Centre for Research in Computational and Applied Mechanics
Department of Mechanical Engineering
University of Cape Town
Rondebosch, Cape Town, South Africa

A CFD Investigation of Cavitation and Associated Deposit Formation in Modern Diesel Fuel Injectors

Author:	Jean-Paul Pelteret
Student Number:	PLTJEA002
Course:	MEC5010Z
Submission Date:	September 2007
Produced for:	Dr C Meyer CERECAM Dept. of Mechanical Engineering University of Cape Town
	Prof A Yates Sasol Laboratories Dept. of Mechanical Engineering University of Cape Town

Abstract

Reducing the pollution of new vehicles has become a priority to vehicle manufacturers, particularly given the fact that emissions requirements that must be achieved by diesel vehicles are becoming more stringent. Modern fuel injectors on common-rail diesel vehicles use very high rail pressures to aid atomisation and increase combustion efficiency. However, associated with the high injections pressures is the issue of nozzle cavitation. Cavitation leads to pockets of diesel vapour forming in the nozzle and it is hypothesised that this causes the formation of deposits in the nozzle. It is also suggested that the collapse of the cavitation vapour space results in extremely high temperatures within the nozzle, resulting in thermal cracking of the fuel and eventually the formation of carbon deposits.

A two-dimensional axisymmetric CFD model with dimensions representative of an injector nozzle was constructed using a fully structured grid. The standard k-ϵ turbulence model with enhanced wall treatment was used for closure of the Navier-Stokes equations. Multiphase fuel flow was modelled in FLUENT® using the mixture model and the full cavitation model developed by Singhal et al. was used to simulate cavitation vapour formation.

It was found that cavitation occurred in the nozzle for the entire spectrum of fuel parameters allowed by the EN 590 specifications. The fuel parameters that most strongly affected cavitation formation were the fuel viscosity and surface tension. It was observed that the decrease in fuel density and viscosity resulted in decreased flow development time.

A simple model for the simulation of the collapse of the cavitation void space was developed. The Rayleigh-Plesset equation was used to determine the bubble radius. Viscous, surface tension, mass and heat-transfer effects were taken into account. A backwards differencing method was used to solve the governing equations.

It was concluded that, for the assumed conditions, there is a strong possibility that thermal cracking could occur. This confirmed the hypothesis that cavitation was the driving mechanism for deposit formation. It was observed that a decrease in fuel viscosity or increase in contaminant gases resulted in elevated collapse temperatures. Additional initial parameters that influenced the maximum collapse temperature are the initial bubble radius and vapour temperature.

Declaration

1. I know that plagiarism is wrong. Plagiarism is to use another's work and to pretend that it is ones own.
2. I have used the Vancouver convention for citation and referencing. Each significant contribution to, and quotation in, this report from the work, or works, of other people has been attributed and has cited and referenced.
3. This dissertation is my own work.
4. I have not allowed and will not allow anyone to copy my work with the intention of passing it off as his or her own.

Signed: Signed by candidate

Name: Jean-Paul Victor Pelteret
Student Number: PLTJEA002
Date: 18 September 2007

Acknowledgements

Prof. Andy Yates, who inspired this project, and without whose assistance this work would never have been possible.

Dr Chris Meyer, whose enthusiasm and expertise in CFD led me to pursue this area of specialisation.

Dr Nirmal Weerasekara, for his invaluable input and insight into the CFD aspect of this project.

Dwain Dunn, for provision of software support when he really shouldn't have had to, and providing assistance where required.

Amy Barty, Vaneshen Naidoo, Darnell Engelbrecht and Harish Appa, for being awesome lab partners, and fun people to be around, and providing assistance when called for.

Brennain Cross, for helping source some pieces of information presented in this dissertation.

Adrian Velaers, for insight made during discussions and providing pictures of fouled injector nozzles.

Table of Contents

List of Figures

List of Tables

Glossary

Atomisation	The process of transforming a body of liquid into a fine spray.
Axisymmetric	Angularly symmetric about an axis.
Cavitation	The process of nucleation in a liquid associated with a sudden decrease in pressure in a fluid.
Cavitation number	A dimensionless number characterising the likelihood and severity of cavitation within a nozzle.
Coefficient of contraction	A dimensionless number quantifying the degree to which the cross-sectional area of a flow has been reduced from the ideal value.
Coefficient of discharge	A dimensionless number quantifying the degree to which the mass discharge from a nozzle has been reduced from the ideal value.
Coefficient of velocity	A dimensionless number quantifying the degree to which the velocity of a flow has been reduced from the ideal value.
Hydraulic flip	A description of the nozzle condition created when convection of gases, generated through the process of cavitation, causes vapour to flow from the inlet to the nozzle exit.
Navier-Stokes equations	A set of partial differential equations describing the motion of fluids.
Non-condensable gas	Contaminant gases that are diffused in a liquid. In diesel, the contaminant gas would mostly consist of air.
Nucleation	The mechanism of cavitation bubble formation and initial growth.
Mini-sac	A type of injector in which the nozzles are not closed by the needle when it is seated. The nozzles are open to the sac volume at the base of the injector.
Rayleigh-Plesset equation	An equation, derived from continuum theory, describing the motion of a spherical bubble undergoing growth or collapse in a Newtonian fluid.
Valve covered orifice	A type of injector that, when the injector needle is fully seated, has the exit nozzles partially or entirely covered by the needle.
vena contracta	The region of a nozzle or jet stream where the flow area is at a minimum.

Nomenclature

Symbols

d	Nozzle diameter
l	Nozzle length
p	Fluid pressure
r	Radius of curvature of nozzle inlet corner
R	Universal gas constant

Greek symbols

α	Phase volume fraction
γ	Adiabatic index $(\frac{c_p}{c_v})$
κ	Cavitation number $\left(\kappa = \frac{p_{\text{inlet}} - p_{\text{vapour}}}{p_{\text{inlet}} - p_{\text{outlet}}}\right)$
κ	Bulk modulus of a liquid

Sub-scripts

1	Upstream characteristic
2	Downstream characteristic
c	Characteristic measured at the *vena contracta*
d	Dispersed phase
e	Nozzle exit characteristic
id	Ideal value
g	Non-condensable gas
l	Liquid phase
k	Secondary phase
m	Mixture
v	Vapour phase
∞	Far-field

Abbreviations and Acronyms

Cc	Coefficient of contraction
Cd	Coefficient of discharge
MFR	Mass flow rate
NCG	Non-condensable gas
ppm	Parts per million
Re	Reynolds number
Re_h	Reynolds number based on hydraulic head
STP	Standard temperature and pressure
RANS	Reynolds Averaged Navier-Stokes
VCO	Valve covered orifice
VFR	Volume flow rate

1. Introduction

At a time where world oil resources are becoming more scarce, an imperative for more fuel-efficient vehicles is being strengthened. This fuel economy requirement must be met while producing lower emissions and without diminishing vehicle performance.

Diesel vehicles offer better fuel economy over their petrol-driven counterparts. However, this is often at the expense of increased ancillary running costs. For a diesel vehicle to be economically viable to the average private motorist, the running cost must be offset by the gain in fuel economy.

To achieve the required combustion efficiency and lower emission output, it is necessary for the fuel to be atomised more effectively upon injection into the combustion chamber. Modern injectors require greatly increased injection pressures, which results in exit velocities in excess of 400 m/s to 500 m/s [9, 10] and improved spray penetration and atomisation.

The increased injection pressure has, however, been linked to increased deposition of material in the injector and premature failure of fuel injectors. Such deposit formations, shown in Figure 1.1, are hypothesised to be caused by increased temperatures in the injector and possible cracking and dissociation of the fuel. It is speculated that the dissociated fuel accumulates in regions of the injector walls and promotes this deposit formation.

Figure 1.1: Section through a fuel injector nozzle with deposition

Nozzle diameters are typically in the order of 0.15 mm and injection durations are measured in microseconds. Direct measurement of characteristics of actual injectors is extremely difficult due to the physical size and time-scales involved in the injection process. The use of Computational Fluid Dynamics (CFD) thus becomes an extremely important aid to the understanding of this process. The Literature Review which follows on page 5, reviews the several studies which have been performed to investigate the flow of fluid in fuel injectors.

1.1 The basics of fuel injectors and cavitation

Each cylinder of a diesel engine has a injector situated between the combustion chamber and the fuel pump. It is arguably the most complex part of a common-rail diesel engine and plays a vital role in the effective combustion of fuel. Each injector is fed off a highly pressurised common fuel rail that may operate at pressures up to 2000 bar.

The injector is controlled by the Electronic Control Unit (ECU) and serves the purpose of providing precisely measured quantities of fuel into the combustion chamber at an exact time for a closely controlled interval. This is achieved by the movement of the injector needle along the axis of the injector to, and away from, the injector nozzle(s). Depending on the design of the injector, there may be more than one nozzle to which flow may be directly or indirectly blocked by the needle. Currently, the most popular method of control of the injector needle is by the use of solenoids and springs, a design shown in Figure 1.2. Third generation injectors are changing to piezo-wafer crystals for more precise control of the needle.

The period of time for which the needle is lifted off its seat determines the volume of fuel which is injected into the combustion chamber. The volume flow rate is closely controlled under all conditions as the volume of fluid that is injected should be consistent and repeatable. The number of holes and their diameter is related to the effectiveness of the injector to atomise the fuel. Effective atomisation is critical in achieving efficient combustion, as the smaller the fuel droplets the greater the surface area, which leads to better combustion. Enhanced atomisation is achieved by expelling fuel out of smaller diameter nozzles at a greater pressure.

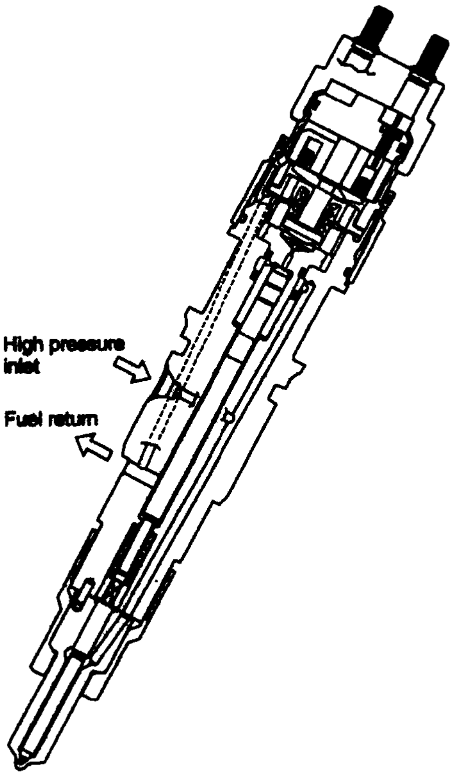

Figure 1.2: Cross-section of a diesel fuel injector [1]

However, raised fuel line pressure increases the tendency for fuel to cavitate inside the injector. Cavitation is a phenomenon associated with a sudden change in direction of a high velocity fluid. The direction change often causes a low pressure region to form in the flow field. If the pressure loss is great enough to drop the pressure to the fluid vapour pressure, the diesel liquid will convert to vapour in order to accommodate the pressure loss. Such a phenomenon occurs near the inlet of the injector nozzle, and possibly on the edges of corners of the injector needle.

There are numerous operational difficulties associated with deposit formation in nozzles. Firstly, the already small flow cross-sectional area can become severely reduced, affecting spray formation and effective fuel dispersion in the engine. This would lead to very poor engine performance with reduction in power and fuel economy and a considerable increase in soot emissions. The deposition may be very severe causing the complete blockage of a nozzle. Ultimately, this would render the injector completely unfit for use and the device would require replacement. Should deposits become dislodged and injected into the engine, these deposits become nucleation sites for soot growth, thereby increasing the pollution output of the engine.

Additionally, cavitation has the ability to erode material and cause substantial damage to its parent apparatus. This damage is attributed to the nature of the collapse of tiny bubbles that form in cavitating flow. High pressures, temperatures and velocities are invariably generated in regions of bubble collapse.

It is largely accepted that there is a strong interconnection between fuel injection rate, spray formation, cavitation and pollution emissions [11]. This makes the understanding of the cavitating flow in injector nozzles imperative to improving on both injector design and fuel blending.

1.2 Role of the fuel industry

It is clear that the flow through a nozzle is influenced by operating conditions such as pressure and fuel temperature; nozzle geometry and fuel properties. Theoretically therefore the variation of these parameters could be used to control the operation of the injector.

It is not clear what effect the alteration of fuel properties has on the severity of cavitation present in the injector nozzle. It is known that cavitation is an aid to effective atomisation; and it is hypothesised that it increases the rate at which deposits build up in the injector. Clearly with the use of higher injection pressures in the next generation injectors, it is crucial that the role which the fuel itself has in the formation of the cavitating regions be understood.

The control of the amount of cavitation present in a nozzle could lead to decreased deposit formation at the nozzle inlet and exit and, injectors with an increased life-span and performance. Currently, the only level of control use is through altering the injection pressure and the inlet radius of each nozzle. By altering specific fuel properties, it may be possible to produce a fuel that greatly enhances overall performance for the next generation of injectors.

1.3 Dissertation objectives

The overall objective of this research was to understand the effect of fuel properties have on the cavitation phenomena that occur in diesel fuel-injectors.

This objective was achieved by observing cavitation effect in two different circumstances, namely during

1. **Vapour formation:** An axisymmetric nozzle of similar dimensions to that found in a specified fuel-injector is to be simulated using a fluid of differing properties. Flow differences are to be noted and quantified where possible.

2. **Vapour collapse:** The collapse of a cavitation void was to be modelled. A first-order estimation for the conditions experienced during collapse had to be made. Since the temperature experienced at the point of collapse was critical, a qualified approximation of this property was vital.

This study was performed using FLUENT® 6.2.16, a commercially available CFD code. Additional package such as Mathworks MATLAB® and Microsoft® Excel were also available for use.

2. Literature Review

The literature review which follows embraces the topics that covers the scope of the topics discussed in this dissertation. Background information for the investigation of the effects of fuel parameters is provided in this chapter. Items of particular interest are the effect of cavitation on fuel injection, cavitation modelling and simulation, as well as experiments and studies performed on the field of interest.

2.1 Effect of cavitation on fuel injection

There are several reasons as to why the understanding of the dynamics involved in the process of fuel injection is so important.

Firstly, the breakup of the jet of fuel exiting a fuel injector has a significant effect on the pollution levels of the engine. This is because most of the pollution is caused by unburned fuel due to poor air/fuel mixture. Further, an increase in surface area to volume ratio will provide an increased burn efficiency. This is due to an increase in heat transfer between the compressed air in the cylinder to the fuel droplet.

The goals of both reduced pollution and increased surface area to volume ratio can be achieved by having a finer spray emanating from the nozzle [12, 13]. This is widely believed to be assisted by the presence of cavitation in the nozzle [10, 14, 15, 16, 17], although some literature discounts this idea [15].

2.2 Deposition in fuel injectors

Deposit formation mechanisms in internal combustion engines are discussed by Lepperhoff et .al. [18]. It was noted that gaseous components of fuel condense and adsorb at the wall due to low wall temperatures. Carbonaceous particles are deposited by adhesive forces between the wall and particles (sticking), attachment by a liquid surface layer (incorporation) and impaction by the motion of particles from a region of higher temperature to one of lower temperature (thermophoresis).

Deposit formation was categorised into two distinct phases. The first, the induction phase, is when a contact medium is built up between the wall and particles. The contact medium consists mostly of hydrocarbons which condense at the wall. In the second phase, carbon particles are able to deposit onto the contact medium. Gaseous components are also able to diffuse into the deposit, causing the density of the deposit to increase. Pyrolysis and polymerisation of the deposit occur and fix the deposit. It was concluded that the only method of avoiding deposit formation is at the induction phase.

In reference to previous work, Williams [19] discussed the severity of deposition around the injector needle. It was concluded that the needle tip, which is exposed to combustion gases and liquid fuel, commonly accumulates light to heavy carbon deposits. The leading edge of the needle, which seats on the injector body, shows very little accumulation of carbon deposit.

Leedham et al. [13] investigated the presence of deposit formation at the tip of injector nozzles using fuel with fuel-additives. Deposition at the fuel-injector tip was observed. It was noted that any deposition in the spray hole is a critical factor, since it leads to less effective fuel atomisation. The point that increased fuel-rail pressure leads to increased fuel injector tip temperatures was noted.

2.3 Experimental studies

Laser Doppler velocimetry (LDV) was used by Sou et al. [2] in order to understand how cavitating flow in nozzles enhances the liquid jet atomisation and velocity distribution of cavitating flow in a two-dimensional transparent nozzle. Tap water with a temperature of 291 K was discharged through a nozzle, with a length, width and depth of 16mm, 4mm and 1mm respectively, into ambient air. The cavitation number used was derived from Bernoulli's equation, and accounted for the average velocity of the flow. The velocity of the flow, and consequently the cavitation number and Reynolds number were altered during the experiments. Additional control over the Reynolds number was maintained by altering the temperature of the water. For some experiments, nucleation sites were introduced by adding 3μm silicone carbide particles to the water.

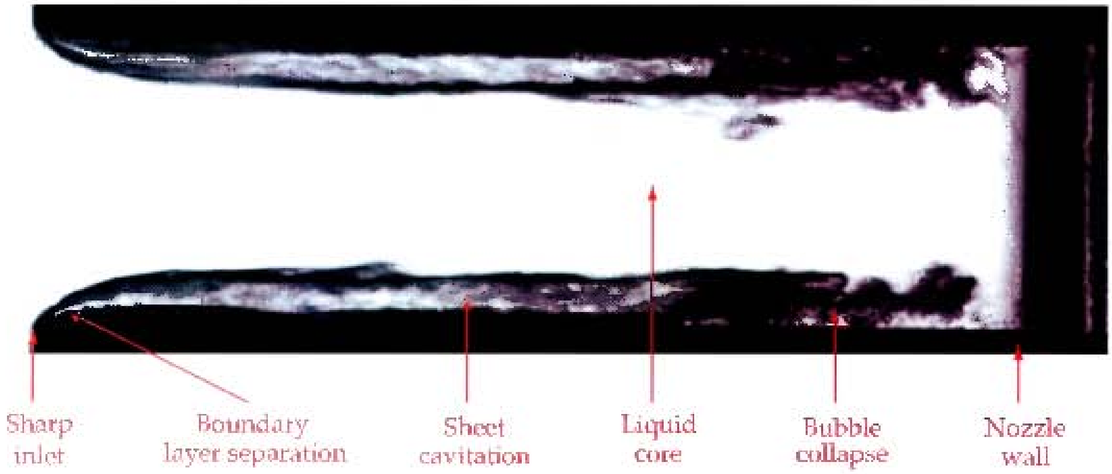

Figure 2.1: Supercavitation in a two-dimensional nozzle, flow moving from left-to-right [2]

The results of the experiments showed that the inception of cavitation occurred near the outer edge of the separated boundary layer. They were able to distinguish between three different cavitation regimes in the nozzles, namely super-cavitation (low cavitation number), developing cavitation and no cavitation (high cavitation number). The supercavitating condition shown in Figure 2.1. It was observed that for intermediate conditions, reattachment of the separated boundary layer occurred in the middle of the nozzle. By altering the cavitation number, keeping Reynolds number approximately constant (by changing the liquid temperature), it was determined that cavitation depended on cavitation number alone. It was determined that a large velocity fluctuation exists downstream of the separated boundary layer, and decreases near the nozzle exit.

Additionally, it was noted that for the supercavitation conditions, lateral flow from the liquid core to the side walls just upstream of the nozzle exit was present, increasing the spray angle and causing enhanced atomisation.

An experimental investigation was conducted by Schmidt et al. [20] to detect cavitation in working diesel fuel injectors. A non-dimensional cavitation number, determined from one-dimensional nozzle theory, and the coefficient of discharge were used to characterise the transient flow. Flow in nozzles with different numbers of holes, as well as differing nozzle throat inlet geometry, was observed. Injection pressure, needle lift and rate of injection was recorded.

For injection pressures of up to 100 bar, it was concluded that behaviour of sharp-edged (both single- and multi-holed) nozzles, corresponded well with that predicted by one-dimensional theory and was similar to that shown in steady-state experiments. A linear relationship between the coefficient of discharge and the square root cavitation number, as predicted by one-dimensional theory, was verified. It was determined that the flow through a rounded multi-holed tip had the characteristics of a non-cavitating nozzle.

Oscillating needle lift was measured in the multi-holed injectors, which resulted in a fluctuation in the rate of injection and the upstream pressure. Although it was predicted that this would have an effect on the coefficient of discharge, no effect was observed. The coefficient of discharge was seen to steadily decrease as the injection time increased.

A paper by MacDonald [21] discusses the use of a fuel injector data acquisition system, known as the AKRIBIS system. The tool is used to record fuel delivery rates and timings. This data is used to characterise delivery rates and timings of fuel injectors, as well as cavitation bubble formation and collapse, and diesel molecular chemistry in terms of the decomposition and disintegration of fuel during bubble collapse.

Typical discharge velocities for the liquid were in the range of 500 m/s to 800 m/s for pressures ranging from 1000 bar to 1800 bar. Is was observed that an increase in injection pressure resulted in an increase in fuel discharge temperature (static temperature) of up to 80°K. This was attributed to the flow dynamics, since the pressure in the fuel line is very high and adds an enormous quantity of kinetic energy to the flow.

The author noted that the collapse of cavitation bubbles results in either very high temperatures or sonoluminescence. The collapse temperatures of non-volatile fuels have been measured as high as 5000°K. It is the authors opinion that the decomposition of vapour's constituent long-chain polymers lowers the collapse temperatures considerably. The technique used to measure the collapse temperature was not outlined. It was also noted that the typical existence period for a cavitation bubble is between 1.0 μs and 2.5 μs.

Benajes et al. [11] analysed the influence of diesel nozzle geometry in the injection rate characteristics. This included the effects of nozzle length and orifice conicity, which is the relationship between the diameter of the nozzle inlet and outlet.

It was found that for a hole with no orifice conicity, where the nozzle inlet and outlet are of the same diameter, the mass flow rate was independent of the pressure drop. This describes a choked flow situation caused by cavitation. Experiments revealed that a conical nozzle did not experience the same effect. It was determined that when no cavitation appeared, there was a good relationship between the discharge coefficient of the nozzle and the flow Reynolds number. However, when cavitation was present, the Reynolds number became meaningless and the flow is best characterised by a non-dimensional cavitation number.

A paper comparing cavitation phenomena in scaled-up diesel fuel nozzles was presented by Ganippa et al. [22] in 2001. Four geometries, including nozzles with an inclined hole and axisymmetric nozzles, were tested at Reynolds numbers between 40 000 and 100 000. Water was chosen as the working fluid. The geometries were made using transparent materials, allowing for photography of the inception and development of the cavitation phenomena. The experiments showed that the distribution of cavitation, as well as the cavitation structure, influence the injector spray pattern and distribution. The cavitation structure was sensitive to the geometry of the sac and hole. As the hole inclination was increased from perpendicular to the centreline of the injector, the cavitation shifted toward the centre of the hole.

It was concluded that inception bubbles grew intensively in the shear layer and developed into cloud-like structures. Cavitation cloud shedding was present in all geometries due to instabilities in the shear layer. It was observed that, under heavy flow conditions, the cavitation cloud can transform into a glossy sheet form (similar to that seen in Figure 2.1). It was also noted that, due to the non-symmetric distribution of cavitation within the hole, the outflow jet atomised on the side where cavitation was present and did not atomise on the side where there was less cavitation.

Payeri et al. [14] performed a study to determine the influence of cavitation on the internal flow of a diesel fuel injector as well as its spray formation. Two orifice injectors were used, one having a cylindrical nozzle, while the other had a conical (tapered) nozzle. Measurements were taken for injection pressures of up to 80 MPa.

It was concluded that a nozzle with a low level of conicity and smaller rounding radii is more prone to cavitation than the highly tapered nozzle with a large inlet radius. It was determined that the critical cavitation number depends on the injection pressure as well as the geometry. This number was observed to increase with injection pressure. Nozzles with high conicity and a large inlet radius have a high discharge coefficient.

In order to study the influence of orifice geometry on flow at the nozzle exit, Payeri et al. [15] performed experimental research on three modern, six-hole, sac-type, direct-injection diesel fuel injectors of varying geometry. The effect of cavitation on the internal flow of the nozzle and spray formation was observed.

It was observed that the discharge coefficient was affected by the pressure difference between the nozzle inlet and outlet, as well as the formation of cavitation in the nozzle. Cavitation occurred when the pressure difference exceeded a critical value for the tested rail pressure. It was noted that a the decreased coefficient of discharge was related to decreased mass flow through the nozzle. The momentum flux for cylindrical nozzles was slightly lower than that of conical nozzles at high injection pressures. Similarly, the effective velocity of the flow exiting the cylindrical nozzle was lower than that of the conical nozzles. Overall, it was concluded that the velocity and mass flow rate was strongly influenced by cavitation, while the momentum flux was not.

The initiation and development of cavitation was visualised by Roth et al. [10] using enlarged acrylic injector models, high-speed digital video cameras and laser Doppler velocimetry. Two injector designs, namely the conical mini-sac and VCO, were analysed.

Increased turbulence through the onset of cavitation was noticed at the entrance to the nozzle, which affected the size of the cavitation bubbles and the homogeneity of the mixture exiting the nozzle. Cavitation was initiated in regions of low pressure at the core of recirculation zones. It was concluded that flow around the sides of the injector hole inlet could be a possible mechanism for cavitation inception. Increased turbulence levels were measured on the lower part of the injection hole when the cavitation number was increased for moderate flow rates. After the onset of cavitation, it was noticed that the recirculation zone was reduced in size, which led to reduced flow restriction and decreased average flow velocity in that region. Increasing the cavitation and flow Reynolds number resulted in increased turbulent kinetic energy.

Desantes et al. [17] presented a paper outlining the effects of cavitation on the flow momentum and outlet velocity. A one-dimensional model based on Bernoulli's equation was used to describe the momentum flux. Experimental results using a VCO injector with a 144 μm nozzle diameter were attained, and compared to the results of Nurick.

It was observed that a reduction in mass flow occurs when cavitation is present. Once this occurs, the mass flow becomes independent of the discharge pressure. The discharge coefficient decreased when the cavitation number increased, a result that aligned with Nurick's one dimensional theory. The momentum flux was observed to increase proportionally with the pressure drop across the nozzle. It was concluded that the decrease in momentum associated with the reduced mass flow was compensated for by smaller wall shear stresses due to the presence of vapour against the nozzle walls. Outlet velocity was seen to increase with the appearance of cavitation.

Collicot et al. [23] conducted experimental research using clear, tilted orifices to study the internal dynamics of the nozzle, as well as cavitation. Flow inside 200 μm nozzles at pressures of up to 210 MPa were visualised.

It was observed that at high pressures, roughness induced cavitation was formed. It was concluded that nozzle surface roughness, cavitation and boundary layer interaction affected spray droplet formation. The authors commented that such effects would be difficult to capture using computational methods.

2.4 Numerical studies and cavitation modelling

In validating the formulation for the full cavitation model, Singhal et al. [24] compared data from the simulation of two-dimensional axisymmetric nozzles to that of Nurick

A 2-D, axisymmetric grid consisting of 2800 cells, incorporating a 20×120 grid in the nozzle, was used to discretise the sharp-edged orifice of the nozzle. A second-order upwind scheme was used to discretise convective fluxes, and turbulence was modelled using the standard k-ϵ model.

The working fluid was chosen to be water at 300°K. Inlet pressures ranging from 1.9 bar to 2500 bar, with corresponding cavitation numbers between 1.0004 and 1.963 were tested. The non-condensable gas fraction was set to 15 ppm for non-deaerated water, which is the saturation concentration of air in water at atmospheric pressure [25]; 1ppm is used for deaerated water, although it is difficult to deaerate to concentrations below 3ppm [25]. The cavitation number used to characterise flow was dependant on the pressure difference between the inlet and outlet, as well as the inlet and vapour pressure. Solutions were considered to have converged when error residuals dropped four orders of magnitude.

Results showed that the predicted results corresponded very well to Nurick's results. The discharge coefficient was constant in non-cavitating flow, while it showed a dependence on the square-root of the cavitation number when flow was cavitating. Additionally, it was found that when the number of cells in the grid were doubled, the predicted mass-flow varied by less than 1%.

A doctoral dissertation presented by Marchese [12] described a Rayleigh-Taylor mixing rate simulation. A piecewise equation of state was used to describe the pressure of the isentropic fluid in terms of its density and quality. The most basic equation of state, namely the polytropic or gamma law, was used to describe gases. The validity of using this equation of state is not discussed. The vapour region is described as a gamma law gas, a stiffened gamma law gas describes the liquid region, and the mixed region was described by a homogeneous equilibrium model.

A two-dimensional axisymmetric model described the nozzle region of a single-orifice injector. A no-slip condition was applied to the walls of the injector. For coarse computational grids, a partial slip condition was used. This ensured that the zero-velocity usually present at the wall would not be imposed beyond the boundary layer. A high pressure condition was imposed at the nozzle inlet. Adaptive mesh refinement was used to ensure that the computational grid was kept sufficiently fine in regions of large property gradients.

Schmidt et al. [9] produced a fully compressible, two dimensional model of a high-speed cavitating nozzle. The compressibility of both phases was taken into account in order to model extremely high injection pressures. The liquid-vapour density ratio was approximately ten-thousand-to-one; a third-order shock-capturing scheme helped account for large density gradients. A computationally inexpensive continuum method was used to track vapour content. The grid was 140 cells long and 40 cells high.

Both the inlet and outlet boundaries have specified pressures. The upstream boundary was specified far enough for the liquid to be near stagnation conditions. The outlet boundary was specified in such a way so that bubbles and acoustic waves could move out of the domain. Flow reversal at the exit was dealt with by specifying incoming fluid as liquid moving in normal to the boundary. The authors submit that this is not an accurate assumption, and limits their model from predicting hydraulic flip.

Initially, the simple axisymmetric model was evaluated. The only grid sensitivity that was noticed was that the transient length of the cavitation film could change. However, they found that mass flow into the domain was not significantly affected.

Results showed that the cavitation region stretched out along the nozzle, as opposed to forming spherical bubbles. For most of the span of the nozzle, the liquid was constricted into a *vena contracta*. The liquid area expanded near the nozzle exit. It was observed that the vapour bubble reached the nozzle exit, which suggests that the bubbles could collapse outside the nozzle. Results of a nozzle that included a rounded inlet edge indicate that these geometries are also prone to cavitation.

Schmidt et al. [26] used an asymmetric, planar model to determine the effects of inlet and outlet pressure on cavitation and separation within a nozzle. The nozzle included a divergent section at the exit. The computational grid was 140 cells long and 40 cells high, totalling 5600 cells. The fluid was modelled as a single phase, with an equation of state accounting for density changes within the fluid. Experimental studies were conducted to confirm results. A geometry representative of a VCO (valve covered orifice) injector was also numerically studied.

It was found that at high pressure differences, cavitation was present at the nozzle inlet. They found experimental evidence that either cavitation or hydraulic flip may occur at the exit. However, the numerical models could not confirm this because no species other than fuel was accounted for. This cavitation effect was time stable.

The VCO injector was modelled as a planar section, with no particular justification. This model was used to assess the effect of needle proximity on the nozzle flow. The model was simplified to one that had a pressure outlet at the exit, a pressure inlet condition upstream of the nozzle inlet, and a wall condition between the seat and the sac. The latter is due to the zero mass flow rate condition between the sac and the nozzle.

Results showed that a large vapour bubble formed along the upper wall of the nozzle. The liquid separated from the upper surface and flowed along the lower surface of the nozzle. The bubble had a highly transient nature. During bubble growth, the exit momentum was concentrated on the lower wall of the nozzle. After bubble collapse, the exit momentum profile varied greatly and nozzle flow is disrupted by a strong pressure wave. It was concluded that the asymmetry and transient oscillations of the flow could cause the spray to break up very rapidly near the nozzle exit.

Iben et al [27] outline the results of CFD simulation of cavitation erosion performed for Robert Bosch GmbH. The package used to perform the numerical work was ANSYS CFX-5. Results were validated by experimental work.

In order to validate the cavitation model, a basic cavitation simulation was performed for a circular throttle flow. Numerical modelling was checked for grid dependency. Results were found to be largely independent of grid size. Model validation was performed in a steady state condition using a RANS SST (shear stress transport) turbulence model. Rayleigh-Plesset equations were incorporated in the simulation.

It was observed that once the pressure difference between the inlet and outlet reached a certain value, the mass flow rate did not increase for an increased pressure difference. This result described a situation involving choked flow and was confirmed by experimental results. It was noted that this phenomenon is purposely designed into fuel injectors to guarantee a certain mass flow rate under nearly all operating conditions. Overall, it was found that cavitation erosion in injection systems can only be predicted using DES (detached Eddy simulation) modelling methods. This was required in order to resolve the complex interaction between large-scale turbulent structures and cavitation.

In 2003, Fluent Inc. [28] performed simulations of a eight-hole injector using FLUENT® 6.1. Due to the geometrical symmetry, only a 45 degree sector was modelled. A total of 231 000 computational cells were used, of which most were hexahedral.

Pressure was specified at the inlet and outlet. The inlet was modelled at least 8 nozzle lengths upstream of the sac. Symmetry planes were specified at either side of the 45 degree cut. The working fluid was set as a mixture of diesel fuel and diesel vapour. All properties for both phases, including the vapour pressure, was specified. A cavitation model was used to track the production of vapour and separation of the two phases. Non-condensable gases were also taken into account. The standard k-ϵ model was used to model turbulence. In order to resolve cavitation accurately, the cavitating regions was contained at least six cells across their width.

It was found that regions of cavitation occurred where the absolute pressure approximated the vapour pressure. This occurred in regions of high recirculation and where the pressure fell below the vapour pressure. Two regions of cavitation were present: One in the nozzle, and one upstream of the nozzle, where the needle and seat are angled. The diesel vapours were carried outside the fuel injector through the outlet, which indicated heavy cavitating conditions.

Fluent Inc. [29] produced another model of an eight nozzle injector in 2005. The full geometry was modelled to assess the effect of an offset needle on conditions inside individual nozzles. A transient simulation, consisting of 800 000 hexahedral computational cells, was performed.

The fluid inlet and outlet were both modelled as pressure boundaries. The inlet was set at least ten nozzle lengths upstream of the sac. The working fluid was set as a mixture of diesel fuel and vapour. A dynamic-mesh model was used to describe the position of the needle as a function of time. The needle was not kept centred on the injectors vertical axis of symmetry, and was set to rest against the wall of the injector at some point in time. A cavitation model was used, and the effects of non-condensable gases were taken into account. The Realisable k-ε model was used to model turbulence. Compressibility effects were not taken into account.

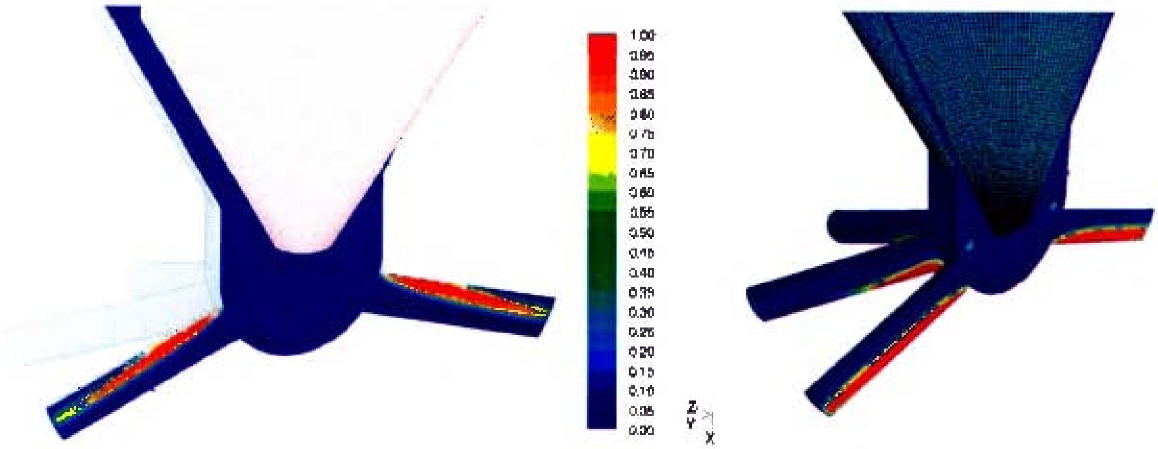

(a) Lifted,offset needle [29]

(b) Near-seated needle [30]

Figure 2.2: Vapour volume fraction on mid-plane of an sac-type eight-hole injector

A result of the simulations is depicted in Figure 2.2(a). Results showed that cavitation occurred at the nozzle throat. It was observed that diesel vapours were carried outside the fuel injector through the nozzle outlet. Even with the asymmetrical needle position, it was observed that the flow pattern in each of the injector nozzles was fairly symmetric. This flow symmetry was observed throughout the injection period.

Figure 2.2(b) shows a similar geometry to that shown in Figure 2.2(a), but with the needle closer to the seated position. No text accompanied Figure 2.2(b), but it is thought that it represents the presence of cavitation in an injector as the needle is about to reseat at the end of an injection. It is interesting to note that the formation of cavitation occurs on the bottom of the nozzle; the opposite position to that of an open needle. This is an important result, since significant rounding of the nozzle inlet edge, used to control and prevent cavitation, occurs only along the upper surface of the orifice.

Three dimensional flow analysis was performed on a VCO injector nozzle by Kubo et al. [31] using the STAR-CD CFD package. The effect of needle eccentricity on fuel-spray pattern was examined, and the simulations were compared to experimental results. The computational geometry consisted of 115 280 cells, which included a region downstream of the nozzle outlet. A needle eccentricity of 10 μm was provided in the direction of one of the holes..

Boundary conditions included a pressure inlet upstream of the nozzles and a pressure outlet downstream of the nozzle exit. A cavitation model was used to predict vapour formation within the nozzles, which was subsequently treated as a gas. The vapour transport equations were solved using the VOF (volume of fluid) model. Needle lift was a linearly described boundary condition occurring over a period of 1.0 ms. An initial lift of 50 μm was imposed for approximately 0.15 ms, after which the needle lift was made to increase linearly over a period of 5.5 ms to its maximum height of 600 μm at 0.7 ms.

A comparison between the coefficient of discharge at a flow time of up to 0.3 ms for models including and excluding a cavitation model, indicated very little difference in results. The average flow rate of simulations including a cavitation model agreed better with experimental results than those that did not use a cavitation model. Flow field visualisation of the numerical results indicate that reverse flow fields within the cavitation region are present. Comparison between numerical results and a five-times scaled-up experimental results visually indicate very similar results for certain needle positions. It was also made clear that cavitation formed at the top of the hole, and proceeded downstream. Long vapour streams of twisted cavitation are present.

A CFD study of erosion and deposition in two-dimensional axisymmetric hydroentangling nozzles was conducted by Anantharamaiah et al. [32] in 2005. FLUENT® was the CFD package used for simulating the flow of water through the tapered nozzle. The mixture model along with a cavitation model were implemented. The cavitation bubble number density was specified. The segregated solver was selected as the solution scheme, the PISO algorithm was used for the time-dependant pressure-velocity coupling. Discretisation schemes for all continuum equations were all second-order upwind, except for the pressure equation which was solved using the PRESTO scheme. The RNG k-ϵ turbulence model was utilised, as it showed the best convergence characteristics for the problem. The solution was considered converged when all residuals has decreased by at least three orders of magnitude.

A two-layer zonal model was used for the near-wall treatment of fluids. The maximum wall y^+ value was kept below 5 for the initial simulations. This value then fluctuated as the pressure was varied above and below the initial condition. The cavitation number for all conditions was close to unity. The grid in the 128 μm capillary region, the location of cavitation initiation, was constructed of a very fine 64×128 structured mesh. The inlet rounding ($\frac{r}{d} = 0.04$) was neglected.

A single phase-flow field incorporating the turbulence model was initially solved for the nozzle. The cavitation model was enabled when convergence was reached for the single-phase simulation. When the cavitating simulations showed no further change in the flow field, the simulation conditions were changed to steady-state and laminar flow. The back-flow at the nozzle outlet was set as that of vapour with a volume fraction of 1, rather than the more realistic treatment as back-flowing air. This assumption was considered valid since the density of vapour is of the same magnitude as that of air.

It was determined that boundary layer separation at the sharp orifice inlet led to the formation of cavitation. This intense cavitation led to the nozzle undergoing hydraulic flip. The water detached from the nozzle wall and caused a constricted jet to form. It was noted that when this condition occurred, the coefficient of discharge dropped from 0.94 to 0.62. Furthermore, it was found that particles released upstream of the inlet were able to impact and deposit at the nozzle inlet.

A comparison of computational prediction of cavitation in diesel fuel injectors and experimental data was performed by Giannadakis et al. [33]. The predictive capability of three different cavitation models was compared to experimental data, and a comprehensive parametric study on model assumptions and settings was performed.

Two Eularian cavitation models both assuming a fixed bubble number density and a linear approximation of the Rayleigh-Plesset equation to simulate bubble growth were tested. One of these models considered the slip velocity between the two fluid phases, while the other did not. The third cavitation model is a Lagrangian model that accounts for the complete Rayleigh-Plesset equation and a variable bubble number density to allow for bubble break-up and coalescence events. Thermal effects were not considered, as it was suggested that they are only significant for injector pressures of over 2000 bar.

A three-dimensional segment of a six-hole fuel injector was modelled using an inlet pressure of 100 bar and an outlet pressure of 1 bar. The injector hole was modelled without inlet curvature. The base computational model used a grid size of 180 000 unstructured cells, while a 1st order discretisation scheme and the standard k-ϵ model were implemented.

It was found that dependant on the variation of simulation conditions, discharge coefficient values of between 0.65 and 0.68 were attained for cavitating flows. It was found that the increasing the cell count up to 500 000 resulted in a Cd variation of only 0.01. It was found that the Cd value difference between the standard k-ϵ turbulence model, the RNG k-ϵ model and two other versions of the k-ϵ model was 0.03. The discretisation scheme accounted for a change of 0.02 in the Cd value. It was found that more dissipative turbulence models and discretisation schemes predicted a lower Cd value. In a high Cd nozzle with a large inlet radius and more tapered hole, discharge coefficients for various simulation setups ranged from 0.77 to 0.83. The difference in the Cd value of 0.06 is attributed to the effects of the grid, discretisation scheme and turbulence model. A test on the result of varying operating pressures was conducted for the nozzles with filleted orifice inlets. It was concluded that the discharge coefficient was a function of the cavitation number and the pressure difference between the inlet and outlet.

The formation of the vapour space, as well as the formation, growth, collapse and reformation of both the individual cavitation bubbles in the nozzle was described. Overall, it was concluded that the Eularian models predict a large void area inside the injector nozzle, while the Lagrangian model predicts a more diffused and gradual vapour distribution. However, all models similarly predicted the velocity increase inside the injection hole and the decrease in discharge coefficient due to the presence of vapour. The collapse of the cavitation region was not captured well by the Eularian models when transitioning between incipient cavitation and fully cavitating flow regimes.

FLUENT® was used by Payri et al. [34] to analyse geometrical effects on the internal flow characteristics of diesel fuel injectors. Cylindrical and conical nozzles with varying grades of hydro-grinding were considered. Computational results were validated by experimental methods.

An extended volume of fluid (VOF) model was used to simulate cavitating flows. A simplified Rayleigh equation accounts for the changing bubble radius. It was noted that the cavitation model implemented in FLUENT® 5.0 did not predict the collapse of cavitation bubbles. Axisymmetric models with a rounded inlet orifice were used to simulate the nozzle. A wall was placed upstream of the nozzle inlet, so flow moved radially into the nozzle. A fully structured grid and partially unstructured grid, of sizes varying from 9000 cells to 200 000 cells, were considered. It was decided that grids of 12 000 cells and 14 000 cells were to be used for the conical and cylindrical models respectively. Laminar flow and turbulent flow were both considered. Results using the Spalart-Allmaras and k-ϵ turbulence models were compared to that considering laminar flow, and it was concluded that the effect of turbulence was negligible. Pressure boundary conditions were set at the inlet and outlet. Typical gas-oil ($C_{16}H_{29}$) properties were used to model the fluid. Time steps of the order of 10^{-9} were used for transient simulations. Convergence requirements were that equation residuals of less than 10^{-3} were reached and that the exit velocity profile had stabilised.

The authors concluded that, even though needle lift was not considered, the transient results were indicative of the diesel injection process. It was determined that a larger inlet rounding resulted in increased mean exit velocities near the wall and an increased discharge coefficient, while the cavitating region was reduced in size. A correlation between the degree of boundary layer separation and the onset of cavitation was observed. CFD calculations predicted that conical nozzles do not have cavitation and are less sensitive to the variation of inlet radius. This is because the pressure experienced in the nozzle is always higher than the vapour pressure. The convergent effect was said to soften pressure gradients and velocity acceleration and was described as a good design tool to eliminate cavitation.

Gavaises et al. [16] investigated flow inside a five-hole diesel fuel injectors using experimental and computational methods. Flow imaging was captured using high-speed photography, while CFD was used to model the injector flow.

Three-dimensional CFD analysis was conducted using a GFS RANS solver and an unstructured grid. The Eularian-Lagrangian cavitation model, which accounted for fundamental processes such as nucleation, bubble growth and collapse and fluid momentum exchanges, was able to simulate geometric induced cavitation, but unable to reproduce the string cavitation observed in the photographs. The SIMPLE algorithm was used to solve the flow-field. Single-phase simulations demonstrated regions in which cavitation was likely to be initiated. Experimentally-derived fixed pressure boundary conditions were applied.

Cavitation was found to be present not only in the nozzles but also inside the volume upstream of the injection holes. Cavitation strings, which are not geometrically induced, were present in regions of large vortex structures in the nozzle tip. Cavitation strings were found to be highly transient and vary considerably with needle lift, but less affected by the cavitation number and Reynolds number once the flow became fully developed. It was observed that the string cavitation significantly influenced the flow pattern inside the nozzle. Geometrically induced cavitation was found to affect the flow rate through the nozzle without the presence of string cavitation. It was concluded that string cavitation was a source of cycle-to-cycle variation of spray patterns in fuel injectors.

Masuda et al. [35] developed a series calculation methodology for computational simulations that predicted flow inside a VCO injector and then performed a spray calculation outside the injector.

The commercial CFD code FIRE version 8 was used to simulate the injector. Due to the symmetry of the injector, only one hole was modelled. Models considering different levels of hydro-grinding were considered by altering the hole inlet radius. Needle movement was modelled. The SIMPLE algorithm was used for pressure-velocity coupling. Internal flow calculation was performed using an Eularian three-fluid and cavitation model. Nozzle geometry was reflected in the internal flow and spray characteristics. The initial vapour void fraction was set at 0.0001 and the bubble number density was specified.

Cavitation was seen to occur at the hole inlet edge throughout the injection period. Asymmetric flow in the nozzle was observed, but credited to the effect of numerical error. The occurrence of asymmetrical nozzle flow was considered possible due to actual asymmetry in the geometry of a real injector. The cavitation region was observed to separate into two regions due to secondary flow in the nozzle cross-section. Twin-vortices of opposing rotational direction, considered to be the secondary flow, were formed in the nozzle. The structure of these vortices changed during periods of low and high needle lift. Needle movement was thus concluded to be a crucial element to the cavitation distribution.

Temperature effects caused due to the compressibility effects of liquid fuel were evaluated by Catania et al. [36]. A computational model employing mass continuity, momentum balance and thermal conservation equations was employed. Physical properties of fluids were modelled using equations of state that accounted for both pressure and temperature variations.

Transient flow through a high-pressure pump-line-nozzle system was evaluated. Cavitation was modelled using a barotropic model. Different thermodynamic evolutions of the vapour and mixture were evaluated.

It was determined that the thermodynamic model applied to the system did not affect the macroscopic formation of cavitation in the system. Pressure distributions were not affected by the variation in vapour void fraction. It was concluded that modelling cavitating flow as isothermal was acceptable due to the negligible temperature variations due to the vaporisation of fluid in the system. Additionally, it was observed that the isothermal models produced the most conservative results with regards to vapour formation.

Blessing et al. [37] used experimental and computational methods to visualise cavitating flow in sac-type common-rail diesel injectors. The influences of spray hole position, inlet rounding and nozzle conicity were determined. Rail pressures of up to 800 bar were tested.

Experimental visualisation was achieved by attaching acrylic glass nozzle tips to real injectors. High speed photography was used to capture the transient cavitation. FIRE v6.3, a finite-volume commercial CFD code, was used to conduct computation simulation. A cavitation model, accounting for bubble growth and collapse, used a linearised Rayleigh-Plesset equation was used to model fluid mass exchange. The bubble number density was specified and needle lift was accounted for.

It was observed that cavitation zones appear in cylindrical nozzles during the injection process. The rounding of inlet edges caused greater flow uniformity and led to a reduction in cavitation intensity. It was concluded that the combination of a rounded inlet edge and a sufficiently conical nozzle can prevent the formation of cavitation in the nozzle.

The difficulties encountered in the numerical simulation of fuel injectors have been described by various authors. These include

- the equation of state for diesel fuel. [12]
- the presence of shock-waves and phase transitions in the flow field. [12]
- the multi-scale nature of the flow field, which includes not only the microscopic nozzle, but also the fluid transfer cavities in the injector and the combustion chamber. Multiple turbulence scales exist, necessitating large computational resources to capture the turbulence effects. [12]
- the tracking of droplets exiting the injector nozzle. [12]
- the large density difference between the vapour and liquid phases. The density of the mixture can change several orders of magnitude over the space of a single computational cell and causes great instability in numerical codes. [26]
- the existence of complex free surfaces at the liquid-vapour interface. [26]
- the treatment and tracking of the second and mixed phases. [26]

2.5 Analytical modelling of bubble collapse

Zwick [38] gives a comprehensive formulation of a continuum approach describing the behaviour of a vapour bubble in liquid. Heat transfer and vapour condensation effects are accounted for during bubble growth and collapse respectively. Heat transfer equations involving convection and diffusion, as well as the temperature distribution inside and outside the bubble, are solved. The bubble dynamics for both bubble expansion and collapse are described using a non-viscous form of the Rayleigh-Plesset equation. Experimental analysis of bubble growth in superheated water was conducted. Comparison of the integral solution to the theory with experimental data found the results to correlate well.

A comparison between two different modelling approaches is given by Lugli el al. [39]. The first model evaluated is a hydrodynamic model, with dynamics described by the Rayleigh-Plesset equations. The authors observed that viscous terms dominate the deceleration of the bubble wall until shock-like rebound occurs. The second model presents a molecular dynamics description of bubble collapse, which applies Newton's laws directly to molecules in the fluids.

It was noted that limitations of hydrodynamic models arise due to the macroscopic considerations involved in their derivation. Standard continuum mechanics is ill-suited to the locally extreme conditions present in a collapsing bubble. Such conditions include accelerations of 10^{11} g and supersonic changes in velocity that occur on a picosecond time-scale. Additionally, models apply assumptions of uniform pressure and temperature within the bubbles. Another limitation is that this model assumes thermodynamic equilibrium, describing conditions where macroscopic fluid variables such as pressure and temperature do not change greatly over molecular length and time-scales.

After the evaluation of the performance of each model's description of the collapse of a 1 nm and 1.5 nm in liquid water of varying temperature, it was concluded that both models provided similar results at the nanometre length scale.

Several methods for solving the Rayleigh-Plesset equation are assessed by Alehossein et al. [40]. Four finite differencing schemes, namely the Euler, central, modified Euler and Runge-Kutta-Fehlberg (RKF) schemes, were evaluated using both constant and variable time-steps. It was found that the RKF method produced the most accurate solution for constant time-steps, while variable time-stepping reduced the computation time significantly. The central differencing method was found to be inefficient and unstable.

The collapse of cavitation bubbles is a rapidly developing area of study. Many papers are available describing the collapse of bubbles in liquids, and models are often extended to investigate near-wall effects [41, 42], free-surface effects [41], microgravity environments [43], asymmetric collapse [41, 42, 44] and the formation and effects of sonoluminescence [45, 46, 47, 48, 49]. The mathematics described in the majority of these models is well outside the scope of this dissertation, and was not focussed on. Instead, the relevant points from the literature have been highlighted in the list below.

- The Rayleigh-Plesset equation is commonly used to describe bubble dynamics for cavitation bubble collapse. The assumptions made in the application of boundary conditions and the solution of the Rayleigh-Plesset equation can have a significant effect on the results attained from the model.
- It is possible to model bubble oscillation in weakly compressible fluids using an extension of the Rayleigh-Plesset equation, known as the Keller equation. [50]
- The external or far-field pressure is either assumed to be constant [43] or of a periodic nature, often approximated as a sinusoidal function [45, 46, 48].
- The gas in the bubble is often considered to undergo polytropic compression [40, 42, 50], and is modelled as an ideal gas [46]. On some occasions, heat transfer effects are neglected and the adiabatic laws

are applied to determine the pressure or temperature of the bubble [41, 45, 49, 51]. In certain circumstances, the van der Waal equation is also considered applicable in the calculation of the bubble pressure [45].

- It is possible to extend the Rayleigh-Plesset equation to include the effects of the compressibility of the surrounding liquid [51].
- The effects of heat-transfer or mass-transfer between the bubble and surrounding environment are sometimes neglected. It is shown that the bubble behaves isothermally when the radial velocity of the bubble wall is small, while there is very little heat loss, representing adiabatic behaviour, only when the radius of the bubble begins to decrease rapidly [44, 47]. Mass transfer is analogous to heat transfer, as when the bubble wall moves slowly vapour is able to diffuse out of the bubble, while vapour is trapped within a rapidly collapsing bubble [44, 47].

2.6 Critique of reviewed literature

The following shortcomings have been noted whilst reviewing the available literature on this subject:

- There is little discussion of the level of inaccuracy of treatment of fluids as inter-penetrating as opposed to two distinct fluids.
- Disadvantages of particular assumptions made during numerical modelling, such as assuming an axisymmetric nozzle or incompressible liquid, was not found.
- The advantages and disadvantages to not using a fine grid around the region of cavitation are not discussed.
- Numerical modelling and simulation of vapour void space and bubble collapse in fuel injector nozzles using commercial CFD packages is not widely discussed. Literature discussing full bubble dynamics that accounted for both growth and collapse of bubbles was found, but there was no reference to the use of the current version of FLUENT® , which employs the "full cavitation model", to model this phenomenon.
- There is no reference in the literature as to what happens to the internal flow-field in the injector or its nozzles after the needle is reseated. A situation such as this would occur once an injection event has ceased.

3. Cavitation and Bubble Dynamics

Cavitation is the process of nucleation in a liquid associated with a sudden decrease in pressure in a fluid. Cavitation involves the rupturing of a fluid, as the pressure exerted on it exceeds the tensile strength of the fluid. This phenomenon results in a fluid phase-change and local regions of vapour forming in an otherwise liquid fluid. [25]

This chapter examines the fundamental ideas used in the formation of the governing equation for bubble dynamics. It also briefly describes the factors affecting the formation, growth and collapse of bubbles as seen in a cavitation environment.

3.1 One-dimensional theory

The cavitation phenomena occurs in a nozzle when fluid flows around a corner. This is most prevalent at the nozzle entrance, where high speed fluid changes direction suddenly as it moves into the nozzle. A low static pressure in the throat of the nozzle is associated with the direction change.

One-dimensional theory is a product of incompressible flow theory, and indicates that flow around a corner of zero radius of curvature will have an infinite negative pressure. This is a physically impossible outcome, and is a consequence of the assumption of constant density made in the formulation of the theory. When the pressure drops below the fluid vapour pressure, the fluid density will change and vapour bubbles may begin to form. The sharper the corner, and higher the velocity at the nozzle entrance, the more likely cavitation is to occur. [20]

Figure 3.1 describes the nature of cavitating flow in a nozzle.

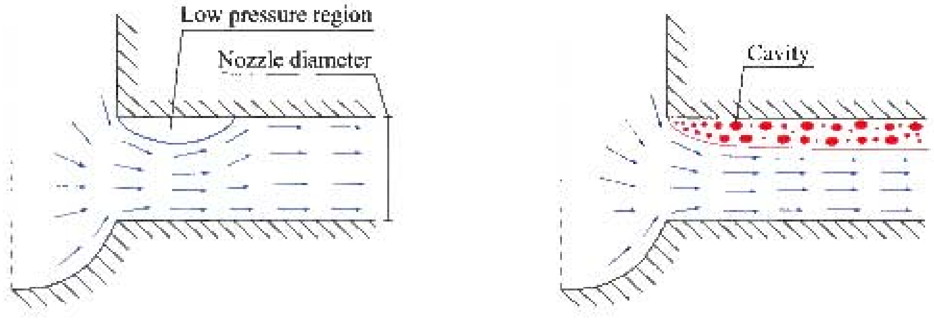

(a) Contraction of flow causes low pressure region

(b) Super-cavitation follows

Figure 3.1: Description of fluid flow in a cavitating nozzle [3]

As fluid flows around a sharp corner, flow separation occurs at the nozzle entrance which results in the presence of a *vena contracta*. The area through which fluid flows near the entrance of the nozzle is effectively decreased. The ratio between the minimum cross-sectional area at the *vena contracta* and the overall cross-sectional area of the nozzle is known as the coefficient of contraction, and is defined as [20]

$$C_c = \frac{A_c}{A} \tag{3.1}$$

where A_c is the reduced flow area of the *vena contracta*, described in Figure 3.2(a)

The coefficient of contraction is largely dependent on the geometry of the nozzle and cavitation parameters. A very rounded nozzle may not contain a separated flow field, and will therefore have a coefficient of contraction of unity. Experimental and theoretical analysis show that the coefficient of contraction of a sharp entranced nozzle should be approximately 0.611. [20]

This value has been measured in a steady-state condition for both cavitating and non-cavitating flows. It has also been observed that, at high injection pressures, the vapour region can elongate and not cause any further disruption to the flow. [20]

The coefficient of discharge, defined as [20, 4]

$$C_d = \frac{\dot{m}}{\dot{m}_{id}} = \frac{\dot{m}}{A\sqrt{2\rho_L(p_1 - p_2)}} \tag{3.2}$$

where $\dot{m}$ is the measured mass flow rate through the nozzle
$\dot{m}_{id}$ is the ideal mass flow rate predicted by Bernoulli's theorem

, describes the efficiency of the nozzle between two measured points. One can therefore measure the losses in the system by comparing the theoretical maximum flow rate with the measured flow rate. [20]

The one-dimensional model makes the assumption that the pressure at the point of contraction is equal to the vapour pressure, P_v. This implies that all losses in the nozzle occur between the *vena contracta* and the

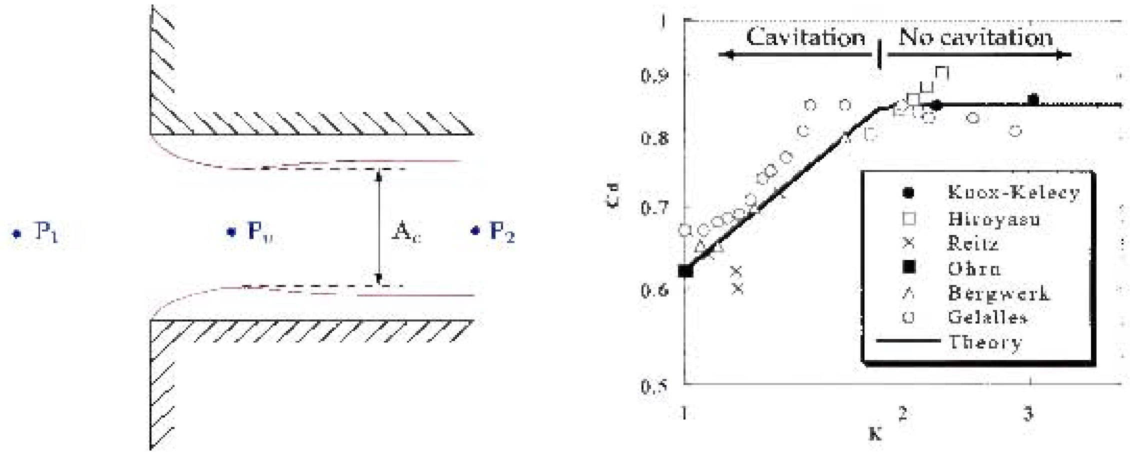

(a) Description (b) Experimental coefficient of discharge vs cavitation number [20]

Figure 3.2: One dimensional nozzle theory

second measured point. With this assumption, the mass flow rate is described only in terms of the vapour and upstream pressure, with the downstream pressure not affecting the flow: [20]

$$\dot{m} = A_c C_c \sqrt{2\rho_L (P_1 - P_v)} \tag{3.3}$$

The points at which the pressure values are referenced in Equation 3.3 are shown in Figure 3.2(a). Equation 3.3 describes a situation similar to that of a choked nozzle. This behaviour has been observed experimentally in cavitating venturi nozzles. [20]

Using the definition of the coefficient of discharge, continuity and Bernoulli's equation, the following description of the coefficient of discharge (Equation 3.4a) and the cavitation number (Equation 3.4b) can be developed: [20]

$$C_d = C_c (K)^{\frac{1}{2}} \tag{3.4a}$$

$$K = \frac{P_1 - P_v}{P_1 - P_2} \tag{3.4b}$$

Nurick [52], after plotting the coefficient of discharge vs cavitation number on log-log axes, observed that the cavitating region lay on a straight line. The y-intercept of the line is the coefficient of contraction and the slope is one-half. When the pressure difference between the inlet and outlet is sufficiently small and K becomes large, cavitation no longer occurs. At these high values of K, the coefficient of discharge becomes largely constant. At high values of K, flow is best characterised by the Reynolds number, as opposed to using the cavitation number. [20]

Various experiments have been conducted by numerous authors over the past sixty years, and results were collated by Schmidt et al. [20] in order to determine the extent to which the coefficient of discharge has a square root dependency on the cavitation number. Figure 3.2(b) shows the results of experimental work plotted against the theoretical result. These results largely conform to Nurick's hypothesis. Sources of error in the experimental results include the inaccuracy of measuring the sac pressure and the inclusion of needle effects. [20]

It is noted that at the beginning and end of injection, the needle will greatly affect the coefficient of discharge described by one-dimensional theory. This is because the low needle lift causes a large pressure loss across its surface. Thus, the measured value of K is only valid during periods of high needle lift. [20]

3.2 Nozzle theory

One-dimensional theory is a useful tool that can be used to analyse ideal nozzles with sharp inlet corners. However, all manufactured nozzles have some curvature on the nozzle inlet, which may render one-dimensional theory inadequate for analysis purposes.

There is, however, no established theory for determining and characterising nozzle flow. Therefore, one is obliged to rely on empirical data described by experiments. These data can be interpreted in the form of several cavitation parameters described in the following section. [4]

Firstly, it is necessary to describe the physical factors that affect nozzle flow. The physical dimensions of the nozzle significantly influence the severity of cavitation, duration of the bubble, and energy release during bubble collapse [21]. These factors include the [4, 21]:

1. nozzle diameter
2. orifice taper
3. nozzle length
4. radius of curvature at the inlet corner
5. upstream pressure
6. downstream pressure
7. viscosity
8. liquid density
9. vapour pressure

Furthermore, dimensionless parameters such as the cavitation number (described by Equation 3.4b) and the Reynolds number based on "hydraulic" head also characterise the flow. The head-based Reynolds number is defined as [4]

$$Re_h = \frac{\rho_l\, d\, v_{id}}{\mu} = \frac{\rho_l\, d}{\mu}\sqrt{\frac{2\,(p_1 - p_2)}{\rho_l}} \tag{3.5}$$

The coefficient of contraction for rounded-inlet nozzles, based on experimental data and described by Nurick, has the same meaning as defined as [4]

$$C_c = \frac{1}{\sqrt{\frac{1}{C_{ct}^2} - \frac{11.4r}{d}}} \tag{3.6}$$

where C_{ct} is the theoretical constant, equal to 0.611, described in Section 3.1. Nurick observed that when $\frac{r}{d} > 0.14$, a *vena contracta* was not formed [11].

It is known that in sharp-edged nozzles, number defining cavitation inception is $K = 1.9$. However, in order to account for the effects of nozzle rounding, an empirical relationship has been developed, and is described by [4]

$$K_{incep} = 1.9\left(1 - \frac{r}{d}\right)^2 - \frac{1000}{Re_h} \tag{3.7}$$

The cavitation number that predicts when hydraulic flip will occur is defined as [4]

$$K_{crit} = 1 + \frac{1}{\left(1 + \frac{l}{4d}\right)\left(1 + \frac{2000}{Re_h}\right)e^{\frac{70r}{d}}} \tag{3.8}$$

It should be noted that if $\frac{r}{d} > 0.05$, then hydraulic flip is considered impossible and $K_{crit} = 1$. The cavitation number as well as the critical and inception cavitation numbers can be used to determine the state that the nozzle will be in [4]:

1. $K > K_{incep}$

   Single-phase nozzle; cavitation does not occur and no vapour appears in the nozzle.

$$C_d = \frac{1}{\frac{1}{C_{du}} + 20\frac{1+2.25\frac{l}{d}}{Rd_h}} \tag{3.9a}$$

$$C_{du} = 0.827 - 0.0085\frac{l}{d} \tag{3.9b}$$

$$u_e = \frac{\dot{m}}{\rho_l A} \tag{3.10}$$

2. $K \leq K_{incep}$

   Cavitating nozzle; vapour forms in near the nozzle inlet

$$C_d = C_c\sqrt{K} \tag{3.11}$$

$$u_e = \frac{2C_c p_1 - p_2 + (1 - 2C_c)\, p_v}{C_c\sqrt{2\rho_l\,(p_1 - p_v)}} \tag{3.12}$$

3. $K \leq K_{crit}$

   Flow may be cavitating or single-phase; hydraulic flip occurs

$$C_d = C_{ct} = 0.611 \tag{3.13}$$

$$u_e = \frac{\dot{m}}{\rho_l C_{ct} A} \tag{3.14}$$

The formulation of the velocity of the fluid jet exiting the nozzle depends on the state of the nozzle. For a single-phase nozzle, it is appropriate to assume a uniform exit velocity. Application of the principal of continuity of mass reveals Equation 3.10. Equation 3.14 is produced in a similar manner to Equation 3.10; however, it accounts for the loss of cross-sectional area of the fluid jet. For the cavitating nozzle, Schmidt and Corrandini showed that the assumption of a uniform exit velocity is not valid. Equation 3.12 was derived to account for the greater velocities experienced through a reduced cross-sectional area during cavitation. [4]

3.3 Mechanisms involved in cavitation

The following section describes, in brief, the cause for, and factors involved in, the cavitation effect. Physical and experimental observations, as well as the mathematics used to describe bubble formation, are discussed. A more detailed summary of relevant information can be found in Appendix A.

3.3.1 Causes of- and factors affecting- phase change

There are two main factors that can initiate a phase change in a fluid. These are a sudden decrease in pressure, which leads to cavitation, or an increase in temperature, which results in boiling. In both cases, phase changes may occur locally and not affect the whole fluid environment as only regions in the fluid may be reach its tensile strength.

Cavitation is the process of rupturing a liquid by a decrease in pressure at a roughly constant liquid temperature. A liquid at constant temperature could be subjected to an absolute pressure lower than its saturation vapour pressure. Fluid rupture occurs when the pressure difference between the absolute- and vapour- pressures is greater than the tensile strength of the fluid at that specific temperature.

Nucleation describes the mechanism involved with the inception of cavitation. Two types of nucleation exist, namely homogeneous and heterogeneous nucleation. Heterogeneous nucleation occurs at a boundary interface between the liquid and a solid wall or contaminant particles suspended within the fluid; it is this mechanism that best describes the process expected in nozzle flows. [25]

Due to the hydrodynamic flow in a system, some regions in the domain will have the optimum geometry to promote bubble growth. As the pressure in the flow regime decreases below the vapour pressure, more areas become capable of generating and releasing bubbles into the flow. In fuel, dissolved gases and microscopic particles that pass through fuel-filters will act as nucleation sites [21]. Microscopic surface geometry has a great effect on nucleation, and surface imperfections can act as nucleation sites. [25]

A further cause of nucleation is the presence of contaminant gases that reside within the liquid. These microscopic bubbles exist in all liquids, as deaeration techniques are not able to remove all gas impurities. The contaminant gas acts as a point of weakness in the fluid, and increases the likelihood of localised fluid rupture. The volume of contaminant gas present in the fluid may cause an increase or decrease in cavitation inception pressure. It is noted that an extremely well purified liquid may have a contaminant gas content of 0.01 ppm. However, decreasing the volume of the NCG below 3ppm in a water tunnel takes a substantial period of time. The mass fraction of air present in water at saturation pressure is approximately 15 ppm. [25]

In a viscous flow system, the minimum pressure experienced in the flow domain will depend on the Reynolds number, which means that the cavitation pressure is also dependent on the Reynolds number. Most flows are both turbulent and unsteady, so both free- and forced- shedding of vortices may occur. The pressure at the centre of a vortex may reach pressures well below the mean pressure of the flow. The implication of this is that cavitation may begin at a transient vortex centre as the pressure there drops below the vapour pressure. [25]

3.4 Bubble growth

Bubble growth can occur due to mass diffusion, thermal, non-equilibrium, convective and surface-roughening effects.

Diffusion of vapour and contaminant gases between the bubble and surrounding liquid changes the mass of the bubble, although the diffusion of contaminant gases only occurs in small quantities over very small time intervals. Change in ambient pressure may also lead to the increase or reduction of bubble mass. Thermal effects only become important over longer time intervals, as the thermal boundary layer is small in inertially controlled bubbles. Convective heat transfer occurs when there is a significant difference in velocity between the bubbles and the surrounding liquid. Surface roughening effects describe heat transfer at the bubble surface due to its instability. [25]

The rate of bubble growth is affected heavily by the thermodynamic properties of the fluid. These properties are functions of temperature, and therefore as the temperature of the working fluid changes, the rate at which cavitation occurs will change. This is because a change in temperature affects not only the physical properties of the fluid, but also the pressure at which cavitation inception occurs. [25]

3.5 Bubble collapse

Cavitation bubble collapse is a substantial and important topic in its own right. The collapse of a vapour-filled bubble in a fluid is often violent and causes much damage to the surrounding material. High velocities, pressures and temperatures are often present in this event. [25]

Collapsing bubbles do not remain spherical. However, spherical analysis is often useful to gauge the maximum possible values of fluid properties such as pressure and temperature that could be attained in such an event. The collapse of a real non-uniformly shaped cavity will create pressures and temperatures of lesser magnitudes than the spherical bubble case because the point of the collapse is dispersed as opposed to being focused at the bubble centre. Factors such as the diffusion of gas from the liquid into the bubble or vice versa, as well as liquid compressibility, reduce the magnitudes of properties experienced during bubble collapse. Compressibility itself has a tendency to reduce the velocity of collapse by a significant margin. [25]

Another factor that complicates collapse is the presence of non-condensable gas or thermal effects. This is because the pressure within the bubble can no longer be treated as constant. While there exists some gas that will decelerate the collapse of a bubble, fluid compressibility does not have a major role in the bubble dynamics. It does however have a significant effect on the formation of shock waves formed when the bubble rebounds after collapse. This is because of the propagation of a pressure pulse directed away from the bubble after it has reached its minimum size. Lastly, it has been noted that surface tension and viscosity do not have a major effect in bubble collapse. [25]

There are three main stages to bubble collapse in a stationary fluid: [25]

1. The initial inward acceleration of the bubble due pressure difference between the bubble and the surrounding fluid.
2. A stage of greatly increasing inwards acceleration, which occurs prior to the period of significant compression within the bubble, due to external pressures and surface tension effects
3. The rebound stage, where the acceleration is very large in the outwards direction

All vapour bubbles that collapse to a size several orders of magnitude less than their maximum size produce a cloud of smaller bubbles upon collapse. This phenomenon occurs over an extremely small time-scale. Furthermore, it is important to note that fluid flow effects cause the bubbles to deform and will significantly alter the effect experienced during bubble collapse. [25]

3.5.1 Thermal effects

It is important to note that the collapsing bubbles can experience thermal effects early in the collapse in a similar manner to that experienced in bubble growth. Even though these effects may be negligible for most of the phase of collapse, they do have a significant effect during the final stage of collapse when the contents of the bubbles become highly compressed due to the inertia of the surrounding fluid. This implies that the bubble can be treated as an isothermal entity for the initial stages of collapse, and adiabatic for the very high velocity period of collapse. Both pressures and temperatures predicted during a spherical bubble collapse are very high. [25]

The non-condensable gas in the bubbles is assumed to behave adiabatically because of the very short time that elapses during collapse. It has been shown that heat transfer between the gas and the liquid is important because of the very small distances and large temperature gradients involved. [25]

4. Computational Modelling

The following chapter outlines the Mathematical and Physics principals that are involved in computational modelling. The fundamental equations defining fluid motion, along with multiphase fluid and turbulence models, are discussed. The method involved in solving the fluids equations is outlined, and the conditions defining the boundaries of model geometry are presented.

FLUENT® employs the finite volume method for domain discretisation and equation solving. It is a numerical algorithm that involves the integration of governing equations over all control volumes in a domain, the conversion of integral equations into a set of algebraic equations using finite-difference approximations and the solution of equations by an iterative method. This method allows all quantities to be conserved on a per-cell basis. The following equation describes the conservation of a quantity ϕ in a cell [53]:

$$\begin{bmatrix} \text{Rate of change of } \phi \text{ in the} \\ \text{control volume with respect to time} \end{bmatrix} = \begin{bmatrix} \text{Net flux of } \phi \text{ due to} \\ \text{convection into the control volume} \end{bmatrix}$$
$$+ \begin{bmatrix} \text{Net flux of } \phi \text{ due to} \\ \text{diffusion into the control volume} \end{bmatrix} + \begin{bmatrix} \text{Net rate of creation of } \phi \\ \text{inside the control volume} \end{bmatrix}$$

4.1 The mixture model

Multiphase flow is, as the name suggests, characterised by the interaction of two or more fluids. In the context of the cavitation problem, it can be described as a bubbly gas-liquid flow where discrete gas bubbles move in a continuous fluid. The mixture model employs a single-fluid approach, where the different phases are consider to be interpenetrating continua. This implies that the bulk flow is modelled considering a single-fluid. For cells that are occupied by more than one fluid, the quantities of each fluid in the cell is expressed using a volume fraction. The total volume fraction of all the phases occupying a particular cell sums to 1. Conservation equations are expressed in terms of the constitutive fluid's volume fractions, and are closed using empirical relations between variable quantities. [4]

The mixture model was is a simplified multiphase model developed to model flow containing at least one fluid. It solves the mixture momentum equations and can account for relative velocities between each phase. The magnitude of the Stokes number calculation is used to determine whether the slip velocity between phases is an important factor. [4]

This section presents the fundamental equations that define the motion of fluid as well as various other fluid properties. Each equation is defined in terms of a Cartesian coordinate system.

4.1.1 The continuity equation

The continuity equation for the fluid mixture is [4]

$$\frac{\partial}{\partial t}\left(\rho_m\right)+\nabla\cdot\left(\rho_m\vec{v}_m\right)=0 \tag{4.1}$$

where $\vec{v}_m$ is the mass-averaged velocity
ρ_m is mixture density

and are defined by the following equations:

$$\vec{v}_m=\frac{\sum\limits_{k=1}^{n}\alpha_k\rho_k\vec{v}_k}{\rho_m} \tag{4.2a}$$

$$\rho_m=\sum_{k=1}^{n}\alpha_k\rho_k \tag{4.2b}$$

where α_k is the volume fraction of phase k.

Equation 4.1 is valid for both compressible and incompressible flows. For an incompressible fluid, the density of the fluid remains constant and the time derivative $\frac{\partial\rho}{\partial t}$ is zero.

4.1.2 The momentum equation

The conservation of momentum equation for the mixture is obtained by summing the individual momentum, or Navier-Stokes, equations for all phases. It is expressed as [4]

$$\frac{\partial}{\partial t}\left(\rho_m\vec{v}_m\right)+\nabla\cdot\left(\rho_m\vec{v}_m\vec{v}_m\right)=-\nabla p+\nabla\cdot\left[\mu_m\left(\nabla\vec{v}_m+\left(\nabla\vec{v}_m\right)^{\mathrm{T}}\right)\right]+\rho_m\vec{g}+\vec{F}+\nabla\cdot\left(\sum_{k=1}^{n}\alpha_k\rho_k\vec{v}_{dr,k}\vec{v}_{dr,k}\right) \tag{4.3}$$

where n is the number of phases
$\vec{F}$ is a body force
μ_m is the viscosity of the mixture
$\vec{v}_{dr,k}$ is the drift velocity for the second phase k

The first two terms on the left hand side of Equation 4.3 describe the local and convective acceleration, while the terms on the right hand side of the equation describe acceleration due to a pressure gradient, viscous effects and external forces.

The mixture viscosity and the second phase drift velocity are defined by [4]:

$$\mu_m=\sum_{k=1}^{n}\alpha_k\mu_k \tag{4.4a}$$

$$\vec{v}_{dr,k}=\vec{v}_k-\vec{v}_m \tag{4.4b}$$

4.1.3 The energy equation

The energy equation takes the following form in the mixture model [4]:

$$\frac{\partial}{\partial t}\sum_{k=1}^{n}(\alpha_k\rho_k E_k)+\nabla\cdot(\alpha_k\vec{v}_k(\rho_k E_k+p))=\nabla\cdot(k_{eff}\nabla T)+S_E \tag{4.5}$$

where E_k is equal to the sensible enthalpy, h_k, for incompressible phases
k_{eff} is the effective conductivity defined by sum of the laminar and turbulent thermal conductivity for each phase, $\sum\alpha_k(k_k+k_t)$
S_E includes volumetric source terms

4.1.4 Cavitation model

A cavitation model is incorporated into the mixture model to account for the mass-transfer effects between a single liquid and its vapour experienced during cavitation. The model used is the "full cavitation model", developed by Singhal et al. [24]. The model accounts for all first-order effects, namely phase change, bubble dynamics (formation and collapse of bubbles), turbulent pressure fluctuations and non-condensable gases. Furthermore, it has been modified to include the effects of multiphase-species transport, slip-velocities between phases, as well as thermal and compressibility effects of the liquid and gas phases. It has been used successfully in modelling cavitation in diesel fuel injectors, and correlates well to Nurick's work. [24]

The formulation of the model employed a homogeneous flow approach to the relationship between the density of fluids and their associated volume fractions. This simplification is considered valid because the velocity slip between liquid and vapour phases is generally small, and the generated vapour consists mainly of small bubbles. [24]

Extension of the original work of Singhal et al. [24] has been completed in order to account for the limitations of the initial work. The cavitation model supplied in FLUENT® 6.2.16 accounts for multiphase flows with multiphase species transport, the effects of slip velocities between liquid and gas phases, and the thermal and compressibility effects of liquid and gas phases. A limitation that remains is that the non-condensable gas mass fraction is considered to be constant throughout the flow field. [4]

Vapour transport
Equation 4.6 is a vapour transport equation that governs the vapour mass fraction, denoted by f [24]:

$$\frac{\partial}{\partial t}(\rho_m f)+\nabla(\rho_m\vec{v}_v f)=\nabla(\gamma\nabla f)+R_e-R_c \tag{4.6}$$

where ρ_m is the density of the mixture, taking into account the effect of non-condensable gases
$\vec{v}_v$ is the velocity vector of the vapour phase
γ is the effective exchange coefficient
R_e is the vapour generation term
R_c is the vapour condensation term

The density of the mixture is calculated as [24]

$$\rho_m=\alpha_v\rho_v+\alpha_g\rho_g+(1-\alpha_v-\alpha_g)\rho_l \tag{4.7}$$

The density of the non-condensable gases, ρ_g, is defined by the ideal gas equation: [24]

$$\rho_g = \frac{WP}{RT} \tag{4.8}$$

Phase change rates

The vapour generation and condensation terms, or phase change rates, are derived from the Rayleigh-Plesset equations, described in Chapter 3. These terms take bubble size into account by limiting the size of the bubble based on the surface area per unit volume.

The rates are defined in Equations 4.9 and 4.10 for an instantaneous, local static pressure p. The two equations described take into account the effects of turbulence-induced pressure fluctuations and non-condensable gases.

When $p < p_v$ [24]

$$R_e = C_e \frac{V_{ch}}{\sigma} \rho_l \rho_v \sqrt{\frac{2\left(p_v - p\right)}{3\rho_l}} \left(1 - f_v - f_g\right) \tag{4.9}$$

, and when $p > p_v$ [24]

$$R_c = C_c \frac{V_{ch}}{\sigma} \rho_l \rho_l \sqrt{\frac{2\left(p - p_v\right)}{3\rho_l}} f_v \tag{4.10}$$

where p_v is the actual vapour phase of the liquid at a given temperature
V_{ch} is a characteristic velocity approximated by the local turbulence intensity, $V_{ch} = \sqrt{k}$
σ is the surface tension coefficient of the liquid
C_e is an empirical constant, equal to 0.02
C_c is an empirical constant, equal to 0.01

The pressure change due to turbulence-induced pressure fluctuations is described in Equation 4.11a [24]:

$$p_v = \frac{1}{2}\left(p_{sat} + p_{turb}\right) \tag{4.11a}$$

$$p_{turb} = 0.39\rho k \tag{4.11b}$$

where p_{sat} is the saturation vapour phase of the liquid
p_{turb} is the turbulence-induced pressure fluctuation
k is the local turbulence kinetic energy

4.2 Turbulence modelling

A turbulence model is introduced in order to provide "closure" to the Navier-Stokes equations. They provide efficient means to resolve the fluctuating components of velocity in order to reduce computational expense. In order to achieve this goal, the exact governing equations can be time-averaged to remove the small fluctuating components, but this introduces additional variables into the equations. Turbulence models provide a means of computing the newly introduced variables. Turbulence models are chosen based on the characteristics of the flow-field. The underlying assumptions and approximations made in the formulation of each model limits their capabilities. [4]

Two methods have been devised in order to alleviate the necessity to resolve small time-scale turbulent fluctuations, namely Reynolds-averaging and filtering. Reynold's averaged Navier-Stokes (RANS) govern the transport of average flow quantities and models the entire range of turbulence scales. This way, they greatly reduce the computational resources required to resolve a flow-field. This method is used in many engineering applications, and is the method adopted for use in this dissertation. [4]

4.2.1 Reynolds-Averaged Navier-Stokes

In Reynolds-averaging, the exact solution of the Navier-Stokes equations are decomposed into the mean and fluctuating components. Equation 4.12 describes the decomposition for velocity and other scalar components, such as pressure and energy [4]:

$$u_i = \bar{u}_i + u_i' \tag{4.12a}$$

$$\phi = \bar{\phi} + \phi' \tag{4.12b}$$

where $\bar{u}_i$ are the mean components of velocity
u_i' are the fluctuating components of velocity
$\bar{\phi}$ are the mean scalar values
ϕ' are the fluctuating scalar values

By substituting this form of the flow variables into the instantaneous continuity and momentum equations and taking a time-average, they can be expressed in Cartesian tensor notation as [4]:

$$\frac{\partial \rho}{\partial t} + \frac{\partial}{\partial x_i}(\rho u_i) = 0 \tag{4.13a}$$

$$\frac{\partial}{\partial t}(\rho u_i) + \frac{\partial}{\partial x_j}(\rho u_i u_j) = -\frac{\partial p}{\partial x_i} + \frac{\partial}{\partial x_j}\left[\mu\left(\frac{\partial u_i}{\partial x_j} + \frac{\partial u_j}{\partial x_i} - \frac{2}{3}\delta_{ij}\frac{\partial u_k}{\partial x_k}\right)\right] + \frac{\partial}{\partial x_j}\left(-\rho\overline{u_i u_j}\right) \tag{4.13b}$$

The equations expressed above are called the Reynolds-averaged Navier-Stokes equations. They are expressed in a similar form to the general Navier-Stokes equations, but now represent the time-averaged values. The terms that appear on the far right of Equation 4.13b, known as the Reynold's stresses, represent the effect of turbulence. It is these Reynold's stresses that need to be modelled in order for the RANS equations to be "closed".

4.2.2 k-ϵ turbulence model

The standard k-ϵ model, proposed by Launder and Spalding in 1974, is the most robust and widely-used turbulence two-equation model. It is robust, computationally economical, and provides reasonable accuracy, allowing it to be used in many applications in industry. [4]

It is a semi-empirical model; the derivation of the model equations relies on phenomenological considerations and empiricism. Two separate transport equations are solved and allows the turbulence length and velocity scales to be independently determined. This turbulence model is only valid in regions where the cell y^+ value is greater than 11.225. [4]

Boussinesq approach

Like many other turbulence models, the k-ϵ turbulence models make use of the Boussinesq hypothesis to relate the Reynold's stresses to the mean velocity gradients [4]:

$$-\rho\overline{u_i u_j} = \mu_t \left(\frac{\partial u_i}{\partial x_j} + \frac{\partial u_j}{\partial x_i}\right) - \frac{2}{3}\left(\rho k + \mu_t \frac{\partial u_i}{\partial x_i}\right)\delta_{ij} \tag{4.14}$$

where μ_t is the turbulent viscosity

The use of this hypothesis greatly reduces the computational expense of computing the turbulent viscosity.

Model transport equations

Two additional transport equations for turbulent kinetic energy, k, and turbulence dissipation rate, ϵ, are solved and turbulent viscosity is solved as a function of these terms. The standard k-ϵ model was developed under the assumption that flow is fully turbulent, and is thus valid only for fully turbulent flow.

The turbulence kinetic energy and turbulence dissipation rate are calculated from the following transport equations [4]:

$$\frac{\partial}{\partial t}(\rho k) + \frac{\partial}{\partial x_i}(\rho k u_i) = \frac{\partial}{\partial x_j}\left[\left(\mu + \frac{\mu_t}{\sigma_k}\right)\frac{\partial k}{\partial x_j}\right] + G_k + G_b - \rho\epsilon - Y_M + S_k \tag{4.15a}$$

$$\frac{\partial}{\partial t}(\rho \epsilon) + \frac{\partial}{\partial x_i}(\rho \epsilon u_i) = \frac{\partial}{\partial x_j}\left[\left(\mu + \frac{\mu_t}{\sigma_\epsilon}\right)\frac{\partial \epsilon}{\partial x_j}\right] + C_{1\epsilon}\frac{\epsilon}{k}(G_k + C_{3\epsilon}G_b) - C_{2\epsilon}\rho\frac{\epsilon^2}{k} + S_\epsilon \tag{4.15b}$$

where G_k is the generation of k due to mean velocity gradients
σ_k is the turbulent Prandl number for k
σ_ϵ is the turbulent Prandl number for ϵ
S_k is a source term
S_ϵ is a source term

The turbulent viscosity is determined by Equation 4.16 below [4]:

$$\mu_t = \rho C_\mu \frac{k^2}{\epsilon} \tag{4.16}$$

Equations 4.15 and 4.16 contain several constants. The standard model constants, derived experimentally, are listed in Table 4.1.

$C_{1\epsilon}$	$C_{2\epsilon}$	C_μ	σ_k	$\sigma\epsilon$
1.44	1.92	0.09	1.0	1.3

Table 4.1: Standard $k - \epsilon$ model constants [4]

4.2.3 Enhanced Wall Treatment

Enhanced Wall Treatment (EWT) is a modelling technique that combines a two-layer turbulence model with enhanced wall functions. It makes allowance for the use of a standard turbulence model with a fine grid that would otherwise invalidate the use of that model. This allows the computational grid to be fine in areas of interest, and coarser where possible. Such instances of the invalidation of a wall-function approach include situations where severe pressure gradients are the cause of boundary layer separation. [4]

$$y^+ = \frac{\rho u_T y}{\mu} \tag{4.17}$$

where y is the distance of the cell centre away from the adjacent wall

The definition of the wall y^+ value is stated in Equation 4.17 above. Where the mesh is fine enough to resolve the laminar sublayer ($y^+ \approx 1$), the model will only employ the two-layer zonal model. When the mesh is sufficiently course ($y^+ \geq 11.225$), the standard turbulence model functions for fully turbulent flow will become solely applicable. In-between these two y^+ values, neither formulation is valid. The EWT supplies a mechanism to apply the necessary near-wall treatment to the flow domain according to the wall y^+ value, even for intermediate meshes. **[4]**

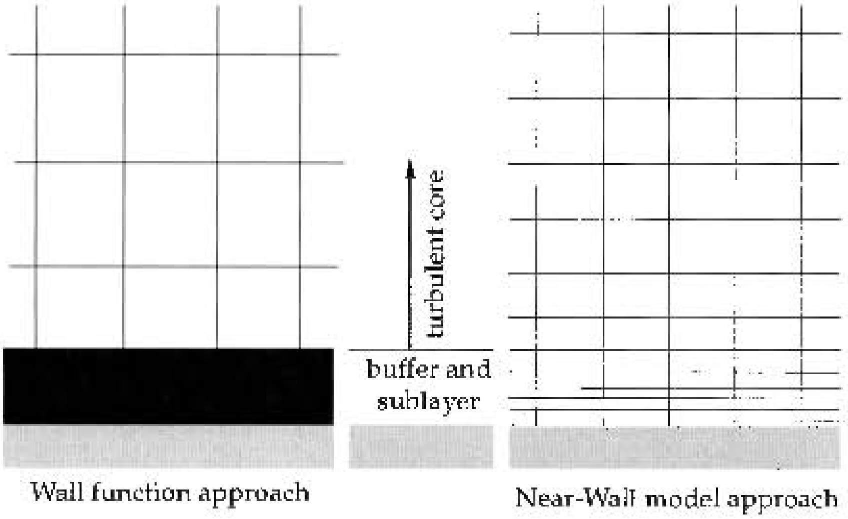

Figure 4.1: Description of near-wall treatment methods [4]

Briefly described, the two-layer zonal model employed for low y^+ values resolves the viscosity-affected near-wall region all the way to the viscous sublayer. It specifies values for ϵ and μ_t in the near-wall cells according to their cell Reynolds number, Re_y. When $Re_y \geq 200$, the flow in the cell is fully turbulent and the k-ϵ model will be employed. In the laminar and transition regions, Wolfstein's one-equation model is used, along with a blending function, to determine the turbulence length scale and viscosity. [4]

Enhanced wall functions blend the laminar law-of-the-wall function with a turbulent law-of-the-wall formulation. This allows the feature to be valid for the entire near-wall region, from the laminar sublayer, through the buffer region and into the fully turbulent outer region. It provides a reasonable representation of the near-wall velocity profile for $3 < y^+ < 10$. It also has the ability to account for pressure gradient effects near the boundary layer. [4]

However, were it important, in order to correctly resolve the laminar sublayer the y^+ value of the cell adjacent to the wall should be approximately 1, with a maximum of 4 or 5. At least 10 cells spanning away from the wall should have a $Re_y < 200$. [4]

4.3 The numerical solver

FLUENT® uses numerical methods to solve the governing integral equations described in Section 4.1 as well as turbulence and other equations. The computational domain is divided up into control volumes using a computational grid. [4]

Integration of the governing equation for each quantity occurs over each control volume. This produces a set of algebraic equations for each variable, which are then linearised. The set of linearised equations are subsequently solved and the values for the dependent variables are yielded. [4]

4.3.1 The segregated solver

The segregated solver employs an algorithm that sequentially solves the governing equations. Since these equations are both non-linear and coupled, several iterations of the solution method must be performed in order for a converged solution to be achieved. [4]

Pressure Interpolation
The standard calculation scheme used in FLUENT® interpolates the pressure values at the cell faces using momentum equation coefficients. Large pressure gradients in the momentum source terms result in a high pressure gradient at each cell face. This makes the scheme unusable, especially for course grids. It is possible to use a second-order scheme to increase accuracy of the cell wall pressure calculations. It does, however, require a good quality mesh to be used. [4]

4.3.2 Discretisation

FLUENT® makes use of a control-volume-based technique in order to convert the governing equations to algebraic equations that can be solved numerically. This method involves integrating the governing equations over each control volume. This in turn results in discrete equations that will conserve each quantity over the control-volume. [4]

Numerical diffusion and discretisation schemes
Numerical diffusion is the result of inaccuracy in the numerical discretisation scheme. Errors in the discretisation of the governing equations over a control-volume occur when the flow through the cell is not aligned with the cell faces. In order to reduce numerical diffusion, higher order discretisation schemes may be used. The use of such schemes depends on the computational grid used, and the flow pattern through the grid. [4]

For highly convective flows, upwind numerical schemes should be used. These use face values derived from cells that are upwind relative to the direction of fluid motion. First-order schemes assume that the cell-centre of any quantity represents the average value throughout the cell. [4]

When flow is not aligned well with the cells, a second-order scheme is preferred over a first-order scheme. A Taylor series expansion about the cell centroid is used to provide a relationship between the properties of the cell and the position within the cell. However, this method sacrifices speed for accuracy. [4]

The QUICK scheme can also be used for rotating flow on a hexahedral grid, as it provides even greater accuracy than the second-order scheme. This scheme employs a weighted average of second-order and central-differencing interpolations for a variable at a cell face. [4]

The discretisation of time is necessary for transient models. This is because each governing equation is integrated over every time step. First-order temporal discretisation is employed; this uses the values calculated at the current and next time-step to determine conditions present at the next time-step.

Under-Relaxation

The magnitude by which a variable is changed between computational iterations must be limited by means of an under-relaxation factor. This change limiting is necessary due to the non-linearity of the governing equations, and ensures computational stability in the solution algorithm. [4]

4.3.3 Pressure-velocity coupling

The segregated solver uses a pressure-velocity coupling algorithm to relate the velocity components to the pressure-field. In general, a pressure-field is guessed, which allows for the resulting velocity-field to be determined. Several iterations of this guess-and-correct procedure are necessary to obtain an accurate quantity-field.

PISO

The PISO algorithm, formulated by Issa (1986), is an extension of the SIMPLE algorithm. It makes use of a pressure predictor step and two velocity correction steps. This has found to be an efficient and fast computational method, albeit computationally expensive. [53]

The PISO algorithm is recommended for transient flow calculations. It is able to maintain a stable calculation for a larger time-step and higher under-relaxation values in comparison to other algorithms. [4]

4.3.4 Solution convergence

A converged solution can be monitored by checking the values of residuals, statistics, property co-efficients and the like. The solution residual is the sum of the residuals for all conserved variables calculated in the flow-field. Convergence is hindered by complex flow conditions, small under-relaxation values and a large number of computational cells. [4]

A decrease in variable residuals three orders of magnitude is a basic expectation of a converged solution. This is not always the case, as factors such as the application of a turbulence model and a poor initial solution guess may hinder the former occurring. The best method of judging convergence is a check whether the solution residuals stay more or less constant over a number of iterations, and whether the solution field looks correct. [4]

4.4 Boundary conditions

The following paragraphs describe the conditions present- and calculation procedure followed at model boundaries.

4.4.1 Pressure inlet

The pressure inlet condition can be used to describe compressible and incompressible fluid properties at a flow inlet. It is most useful for a condition where the inlet pressure is known but the velocity of the fluid is undetermined. The pressure inlet boundary imposes conditions for both total and static pressure. The total temperature, as well as flow direction, fluid mixture fractions and turbulence parameters are also specified. [4]

For incompressible fluids, the total pressure is the sum of the static and dynamic pressures [4]:

$$p_0 = p_s + \frac{1}{2}\rho|\vec{v}|^2 \tag{4.18}$$

For incompressible flows, the total temperature is equal to the static temperature. Furthermore, the density of the fluid at the inlet is either constant or determined as a function of temperature. [4]

4.4.2 Pressure outlet

The pressure outlet boundary condition is used to specify the static pressure at the outlet boundary. Were the fluid to be at supersonic velocities as it crosses the boundary, the pressure is extrapolated from the pressure from the adjacent cells as opposed to using the specified condition. All other flow quantities are extrapolated from interior cells. The total mass flow of the fluid crossing the boundary can be specified in certain circumstances. [4]

Conditions describing flow entering through a pressure outlet boundary can be set. These conditions include the direction, temperature, turbulence parameters as well as the volume fraction of the entering fluid. The specified pressure will be used as the total pressure of fluid that enters the domain through the pressure outlet boundary. [4]

4.4.3 Wall

Wall boundaries are used to specify interfaces between fluids and solids regions. These solid regions can be stationary or undergo a specified radial or translational motion. [4]

A no-slip condition is imposed for viscous flows against wall regions. It is, however, possible to specify a tangential velocity at a wall boundary in order to model slip. Alternativly, a shear stress can be specified at the wall. [4]

Conditions that are specified at a wall include the wall motion, thermal properties, shear conditions and surface roughness. These take into account heat transfer, movement of the wall and the turbulence of flow near the wall. [4]

4.4.4 Axis

The centreline for an axisymmetric model is specified as an axis boundary. It can be described as an axis of revolution, which allows certain three-dimensional geometries that involve 360° symmetry to be modelled as a two-dimensional problem. [4]

No boundary conditions are specified at this boundary. The value of quantities of the cells adjacent to the axis are used to describe conditions along the axis. Property gradients in the angular direction are considered constant. [4]

5. Analytical Modelling

The following chapter presents the model used to approximate the conditions prevailing during the collapse of an idealised cavitation vapour void space.

5.1 Context and purpose of the model

A basic model was developed to provide insight into the collapse of a cavitation vapour void space. It represents an model constructed to determine whether the temperatures involved in the collapse of the vapour space may be high enough to promote pyrolysis and thermal cracking.

Generally, cavitation bubble modelling considers the collapse of individual cavitation bubbles as they flow down the nozzle or are advected into regions of high pressure. The individual cavities that make up the vapour space are treated as spherical bubbles composed of vapour and air and surrounded by vapour what undergoes pressure fluctuations. These bubbles may collapse during or after the injection process, depending on local conditions.

Taking a slightly more macroscopic viewpoint, this model considers the collapse of a portion of the vapour space. This model may not be entirely representative of the collapse of the void space described by an axisymmetric nozzle, since for this case the advected vapour takes the form of an annulus around the liquid flow stream (see Chapter 6 for greater detail). However, this model may reasonably describe the conditions present in the collapse of the void created in a fully three-dimensional nozzle. An example of the conditions described before collapse are present in Figure 2.2, where there is a liquid-vapour interface on four or five of the Cartesian sides of the void. The assumed conditions are depicted in Figure 5.1.

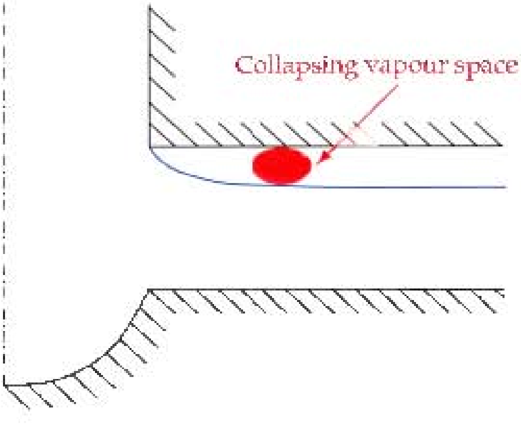

Figure 5.1: Assumed bubble conditions

The vapour space contains a mixture of both contaminant gases and fuel vapour. When injection ceases, the high-velocity flow moving around the nozzle inlet edge will stop and the driver for cavitation is no longer be present. The vapour that remains in the nozzle is subject to the compressive influence of the high static pressure liquid core at the nozzle inlet.

The extreme pressure difference between the vapour, which is at vapour pressure, and the liquid, which is at pressures several orders of magnitude greater than the vapour, causes the vapour space to undergo drastic inward acceleration. Because the chemistry of the liquid and fuel vapour are identical, the vapour can readily diffuse out of the void space when compressed. However, the contaminant gases that remain are unable to diffuse and are compressed to high pressures and temperatures. During the compression stage, it is reasonable to assume that the cavities, composed only of the contaminant gases, may conglomerate into a single mass of gas.

It is the high thermal kinetic energy of the contaminant gases that is of interest. If the temperature of the contaminant gas bubble exceeds 800°K to 1000°K, the impact of the gas with fuel molecules at the liquid-gas interface at the bubble surface is considered to be great enough to break the long-chain hydrocarbons that comprise the fuel. Furthermore, the temperature at the bubble surface may be high enough to promote pyrolysis.

The void space is loosely referred to, both in this chapter and Chapter 7, as a bubble.

5.2 Governing equations

The dimensions of a spherical bubble under the influence of an external pressure is determined by the solution of Rayleigh-Plesset equation [25]:

$$\frac{p_V - p_\infty}{\rho_L} + \frac{p_{Go}}{\rho_L}\left(\frac{R_o}{R}\right)^{3k} = R\frac{d^2R}{dt^2} + \frac{3}{2}\left(\frac{dR}{dt}\right)^2 + \frac{4\mu_L}{\rho_L R}\frac{dR}{dt} + \frac{2S}{\rho_L R} \tag{5.1}$$

where $R(t)$ is the time-dependant radius of the bubble

p_V is the pressure within the bubble, equal to the fluid vapour pressure which is dependant on the temperature of the free-stream

p_∞ is the time-dependant far-field / hydrostatic pressure

ρ_L is the liquid density

p_{Go} is the partial pressure of the contaminant gas

R_o is a reference radius for p_{Go} for the contaminant gas

k is a constant defining the polytropic behaviour of the contaminant gas

μ_L is the liquid dynamic viscosity

S is the bubble surface tension

The Rayleigh-Plesset equation in discussed further in Chapter A.1.

The temperature of the bubble is governed by the First Law of Thermodynamics:

$$\triangle U = \triangle W + \triangle Q \tag{5.2}$$

where	$\triangle U$	is the change in internal energy of the bubble
	$\triangle W$	is the work done on the bubble
	$\triangle Q$	is the energy transferred to the bubble

The terms described in Equation 5.2 are defined as

$$\triangle U = m\, C_V\, \triangle T \tag{5.3a}$$

$$\triangle W = \bar{P} \triangle V \tag{5.3b}$$

$$\triangle Q = -k\, \bar{A}\, \frac{T_B - T_L}{\bar{r}} \triangle t - \triangle m\, L \tag{5.3c}$$

where	m	is the mass of the bubble
	C_V	is the specific heat capacity of air for a closed system
	$\triangle T$	is the change in temperature the bubble
	$\bar{P}$	is the average pressure inside the bubble between time-steps
	$\bar{A}$	is the average area of the bubble between time-steps
	$\bar{r}$	is the average radius of the bubble between time-steps
	$\triangle t$	is the time-step size
	$\triangle m$	is the mass of vapour that has diffused out of the bubble
	L	is the latent heat of condensation

This derivation of the above equation introduces several limitations to the model, namely that [25]

1. liquid compressibility is not taken into account
2. the contents of the bubble are considered homogeneous
3. the temperature and pressure within the bubble are uniform
4. the fluids involved have a Newtonian nature
5. no mass transport of vapour or contaminant gases occurs across the bubble boundary

Brennen [25] indicates that, although the mass conservation condition is applied at the boundary, the resultant description of the kinematic condition is a good approximation of the forces present even when evaporation or condensation is occurring at the liquid-vapour interface.

5.3 Assumptions and simplifications

The following list of assumptions pertains to the analytical bubble collapse model.

1. Liquid
   (a) Liquid and vapour are both identical composition diesel, and can be approximated as the hydrocarbon compound $C_{16}H_{29}$
   (b) Liquid characteristics remain constant with time
2. Gases
   (a) The contaminant gas in the liquid is air
   (b) The air can be treated as ideal gases
   (c) Initial air mass fraction is known
   (d) Specific heat of air remains constant
3. Conditions
   (a) The initial diameter of bubble is considered to be the height of the annular void space taken from CFD models (refer to page 38)
   (b) The bubble has zero initial radial velocity
   (c) Initial pressure inside bubble is the same as the vapour pressure of the liquid at the liquid temperature
   (d) The far-field pressure, equal to the combustion chamber pressure, is constant in time
   (e) During the initial collapse, the vapour leaves bubble (by diffusion) as wall collapses until the bubble contains only air
   (f) During the initial collapse, diffusing vapour condenses at bubble wall interface
   (g) The pressure of bubble remains constant at vapour pressure while diesel vapour diffuses out, thereafter gas compression is governed by the ideal gas law
4. General
   (a) Linear function behaviour for very small time steps
   (b) The bubble remains spherical during collapse

5.4 Physical considerations

The following physical effects have been accounted for in this model:

1. Significant first order thermal effects (pressure work, conduction)
2. Viscous and surface tension effects
3. Temperature dependency of the conduction coefficient of air

4. Diffusion of vapour out of the bubble during initial stages of collapse
5. The latent energy required to condense vapour into liquid at the wall interface

It is appreciated that the predicted temperatures represent possibly the maximum possible due to the assumed physical setting. Upon collapse, energy would be lost due to deformation of bubble surface, resulting in decreased temperatures. Furthermore, the collapse would not be concentrated on one point at the bubble centre, also resulting in a dispersion of energy.

5.5 Solution algorithm

A backwards differencing method was used to determine the evolution of the problem. Figure 5.2 illustrates the algorithm used to solve the equation governing bubble collapse. Accompanying the figure is a detailed discussion of the method, outlined in the paragraphs below.

The differential equation represents an initial value problem, since the initial boundary conditions are known. The following basic steps were implemented to estimate the solution to the Rayleigh-Plesset equation:

1. Initial conditions
    (a) It is necessary to know the following initial conditions: Bubble radius, velocity, acceleration, temperature, pressure and mass. It is possible to refine the guess for acceleration based on the result attained for the second time-step.
2. Bubble dimensions
    (a) A time-step was chosen based on the estimated temperature. This provided excellent stability due to good control of the time-step size when the property gradients during the collapse and rebound phases were great.
    (b) Backwards differencing of acceleration and previous velocity resulted in the current velocity
    (c) The bubble radius was determined from the time-step, and from the current and previous velocities. The initial velocity of the collapsing pure contaminant gas bubble is an extremely important condition in the accurate prediction of the minimum collapse radius and maximum bubble temperature.
    (d) A restrictive condition was applied to the bubble wall velocity and acceleration if the predicted velocity is above the sonic velocity of the surrounding liquid. The current velocity and acceleration are set at the liquid sonic velocity and zero respectively.
3. Bubble properties
    (a) The temperature of the bubble contents was estimated.
    (b) The pressure within the bubble was determined using the ideal gas equation, relating the current pressure to the previous step pressure, temperature and volume and the current temperature and volume.

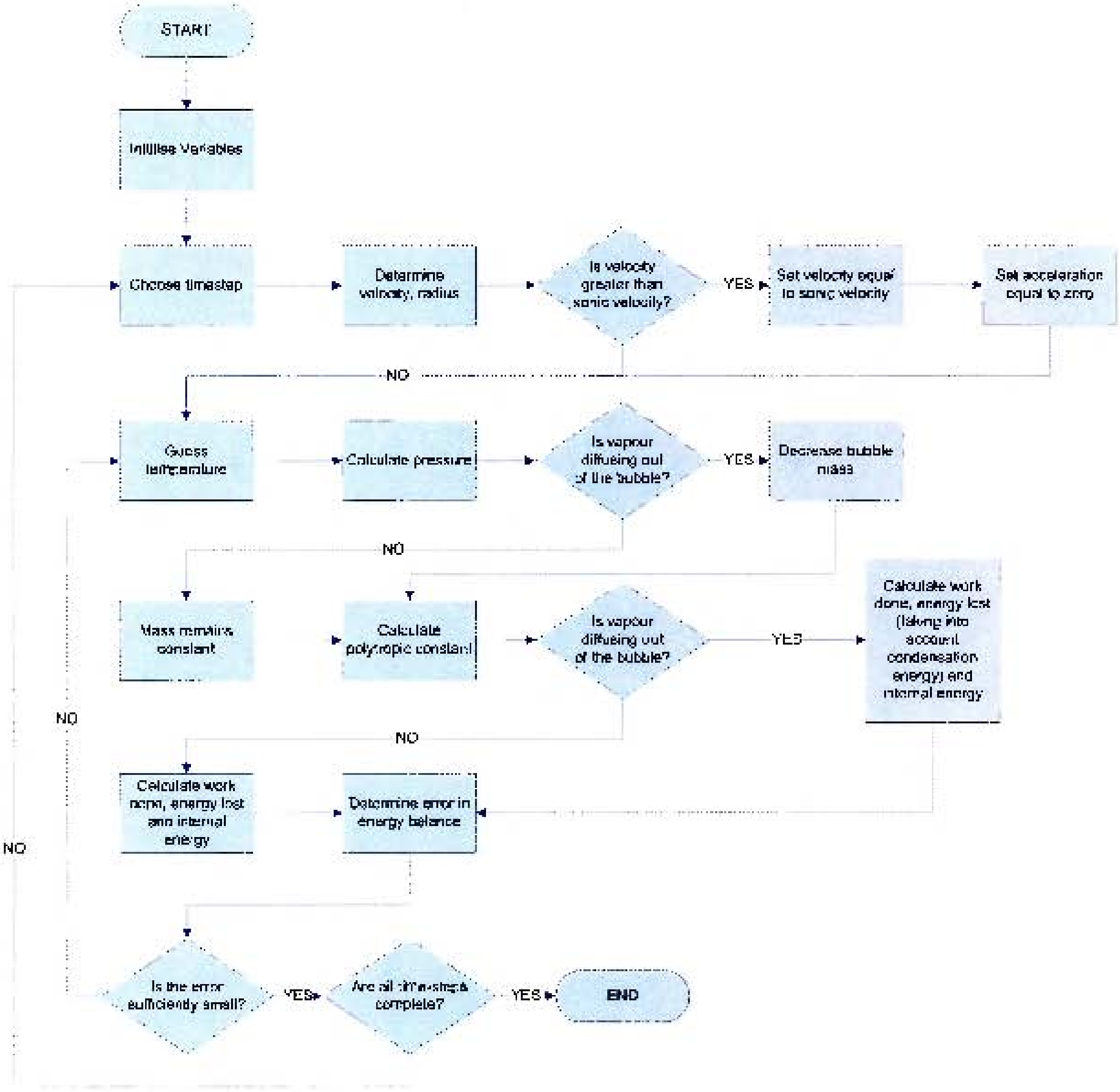

Figure 5.2: Analytical model algorithm

   (c) The mass of the bubble was calculated. If the bubble was in the stage where vapour is still contained within the bubble, then the difference between the current and the previous step mass of the bubble will be related to the change in volume of the bubble and the ideal gas density of the vapour at the current temperature. Otherwise, the mass of the bubble remains constant, since it was assumed that no contaminant gas diffused out of the bubble.

   (d) The contaminant gas polytropic constant, related to the current and previous bubble temperature and volume, was determined.

4. Energy equation

   (a) The approximate work done on the bubble was related to the average pressure exerted on the bubble between time-step and the change in volume between time-steps.

   (b) The loss of energy from the bubble was determined from the conductive heat loss from the bubble centre.

   (c) Should vapour mass be diffusing from the bubble, energy was lost due to condensation of the vapour at the bubble interface. This energy is related to the mass lost from the bubble and the latent heat of condensation of the vapour.

   (d) The change in total internal energy of the system was calculated from the change in temperature of the bubble between the current and previous time-steps, the mass of the bubble and the specific heat at constant volume (closed system) of the contaminant gas.

5. Reduction of solution residual

   (a) The temperature approximated in Step 3a is refined until the error in the energy equation is reduced to a satisfactory level.

6. Factors affecting nozzle cavitation

The main purpose of this thesis is to determine the effect that altering the major physical properties of diesel fuel has on the formation of cavitation in a nozzle. To this end, it was considered useful to concentrate on an axisymmetric nozzle, with a nozzle of similar dimensions to that seen in a real fuel injector (refer to Appendix C for details) and a sharp inlet edge. The pressure difference applied between the nozzle ends would be similar to that experienced in a modern vehicle, and in particular to that used for the injector modelled. The realistic dimensions ensured that the scale of the cavitation phenomena observed would correlate with any experimental data. The sharp inlet edge promotes cavitation in the nozzle.

As described in the paragraphs below, various observations regarding the effect of fuel properties have been made. The effect of variation in fuel density, viscosity, surface tension and non-condensable gas fraction is determined, as well as the effect of rounding the inlet edge of the nozzle. Finally, an approximation of the temperature field that exists in the nozzle is discussed.

In the course of simulations, various other observations and conclusions about fuel injection have been drawn from the results. The conclusions drawn from the observations are described in Chapter 8.

6.1 General flow field

It is conjectured that real injector nozzles would be filled with liquid diesel before and after the needle has seated. This is a fair assumption, since there will be liquid present in the nozzle when the needle seats after an injection.

Upon the application of the pressure differential to the nozzle boundaries, the fluid inside the nozzle accelerates from zero velocity to over 500 m/s in a matter of microseconds. In this period several phenomena, including the formation of turbulent vortices, cavitation inception and vapour transport occur. It is clear that the properties of the flow field vary substantially with time. Since the problem posed is heavily transient, it is felt useful that a description of the flow field is presented.

Figure 6.1 is presented as an aid to the description of the flow-field, and is implicitly referred to in the following paragraphs. The figure presents the normalised mass-flow rate, coefficient of contraction and coefficient of discharge for the nozzle as the time from the application of the pressure difference increases. The mass-flow rate has been normalised for the purposes of presenting a general result. The latter plots are linked to the mass flow rates by Equations 3.2 and 3.4a.

The large pressure difference between the inlet and outlet boundaries (1450 bar) causes the stationary liquid fluid to initially accelerate rapidly. This translates to a rapid increase in mass flow-rate over the first 3.5 μs.

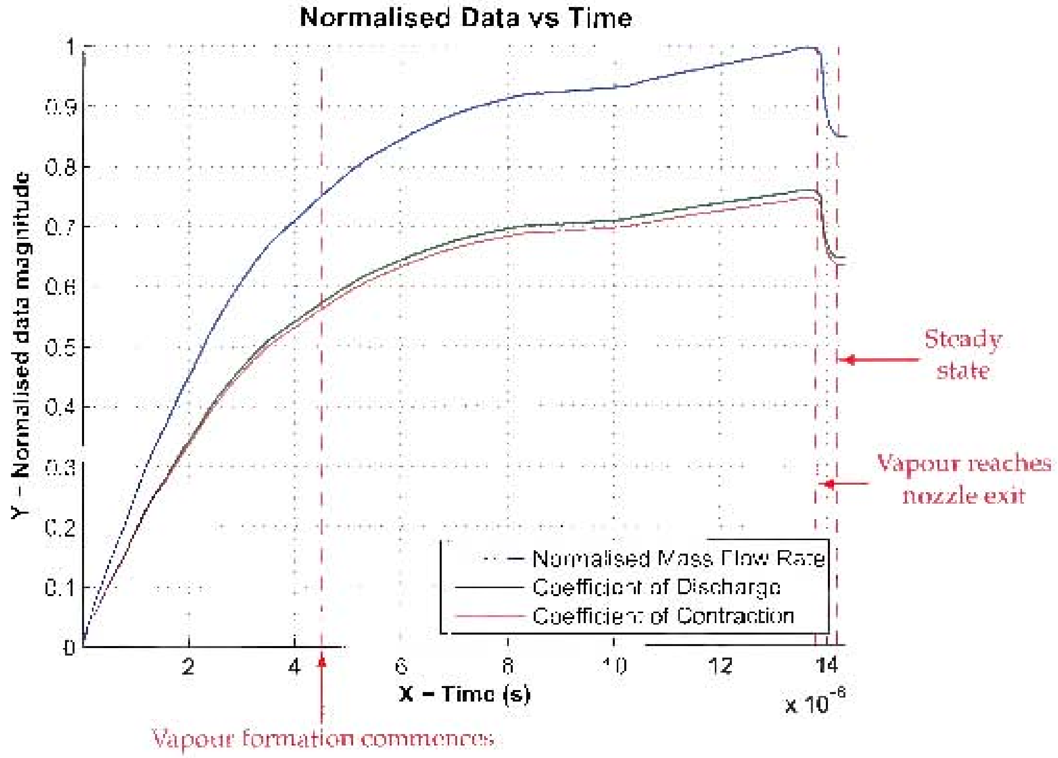

Figure 6.1: Normalised transient mass flow-rate, coefficient of discharge vs time

Due to the assumption of incompressible flow, the pressure field in the domain is fixed almost immediately. This field changes with time due to various phenomena that are described below.

The increase in velocity of the fluid results in the formation of a *vena contracta* at the nozzle entrance. This occurs as the high-velocity fluid moving radially into the nozzle is unable to negotiate the sharp inlet corner. At this point in time, no cavitation is present within the nozzle, since the pressure loss at the entrance is not great enough. The pressure loss across the nozzle entrance increases to a point where the rate of acceleration declines. However, the coefficient of discharge continues to rise as the momentum of the fluid in the nozzle increases.

As the velocity of the fluid moving past the separated region downstream of the nozzle entrance increases, a recirculating vortex forms. At the centre of this recirculating zone is a low-pressure core. The effect of the low-pressure core, superimposed on the pressure loss across the nozzle throat is that the pressure in that area decreases to that of the vapour pressure. This phenomenon is observed after approximately 4.5 μs.

The process of vapour generation, vortex dissipation and the start of vapour advection is shown in Figure 6.2. At this point in time, vapour is generated near the nozzle throat. The point of generation coincides with the location of high turbulent kinetic energy, seen in Figure 6.3. The vapour formed at the core of the vortex is transported upstream to the corner of the inlet, and a distinct vapour bubble is present. This bubble remains stationary in this area with no entrainment into the free-stream, because it remains trapped in the region of recirculation.

As more vapour is generated and the vapour concentration within the recirculating zone increases, it eventually expands beyond the recirculating region. This causes the vortex to dissipate as the cavitation formation

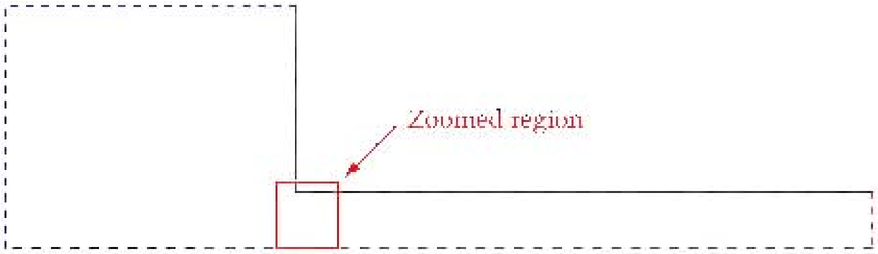

(a) Position of diagrams

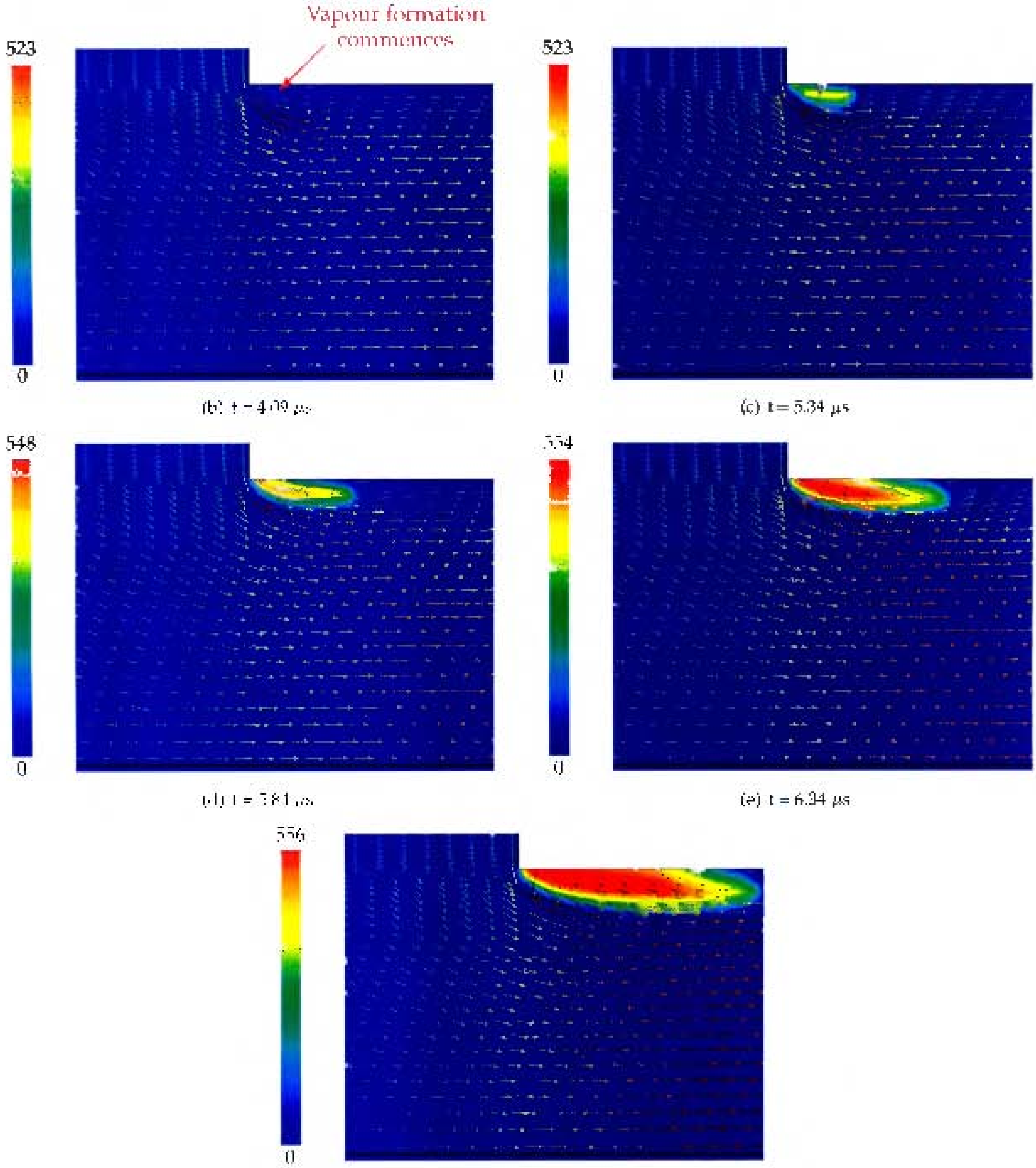

(b) t = 4.09 μs

(c) t = 5.34 μs

(d) t = 5.81 μs

(e) t = 6.34 μs

(f) t = 6.84 μs

Figure 6.2: Vapour phase with velocity vectors [Coloured by velocity magnitude (m/s)]

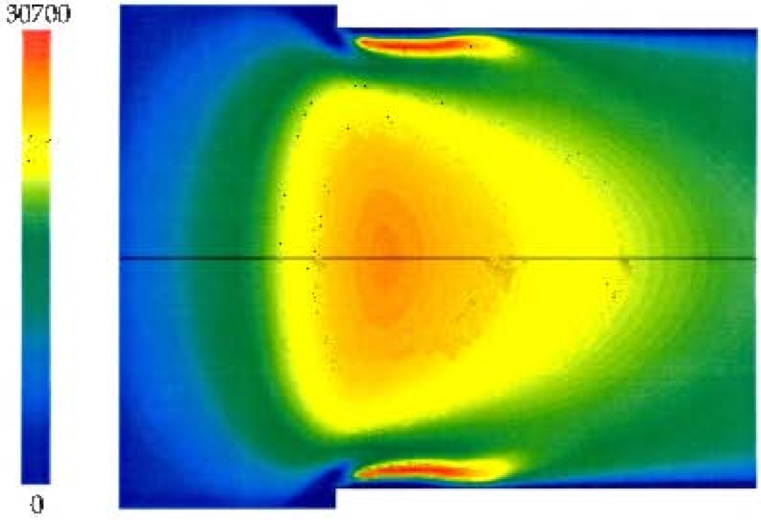

Figure 6.3: Turbulent kinetic energy at t = 6.34 μs [Coloured by turbulent kinetic energy magnitude (m^2/s^2)]

overcomes the effect of the pressure loss. The generation location shifts from the vortex core to the boundary wall. Assuming that the liquid-vapour interface occurs where the volume fraction of vapour is 0.5, the maximum height of the vapour region that is transported against the wall of the nozzle is approximately 15.3% of the nozzle radius. This equates to a coefficient of contraction of 0.717. The advection of the vapour down the length of the nozzle is shown in Figure 6.4.

Initially the rate of vapour formation is low, but as more gas is advected away from the cavitating region, the rate of vapour formation increases. This must occur such that the rate at which vapour is transported away from the nozzle entrance is matched by the vapour generation rate. The mass flow-rate of the vapour down the nozzle increases as the velocity of the liquid continues to increase. As the low-pressure bubble advects downstream, the absolute pressure at the nozzle wall decreases from a high pressure down to vapour pressure.

Vapour mixing into the liquid is noticeable at the downstream edge of the vapour bubble. It is also interesting to note that as the flow-time increases, vapour diffusion occurs increasingly at the liquid-vapour interface parallel the axis of the nozzle. This implies that the quality of the bulk liquid exiting the nozzle decreases with time. However, this could be the effect of numerical diffusion as opposed to a physical diffusion process. The latter may be more likely since the pressure in the liquid is still very high, and the time over which the diffusion process may occur is very small.

When the vapour stream reaches the nozzle exit, the coefficient of discharge reduces dramatically. When this event occurs, "hydraulic flip" is deemed to have occurred. One-dimensional theory predicts that the discharge coefficient drops from 0.761 to 0.637. This is associated with the reduced cross-sectional area through which high density liquid fuel is ejected, and potentially allows for vapour present in the combustion chamber to enter the nozzle. The predicted discharge coefficient value of 0.637 correlates well when compared to the theory and experimental work, previously shown in Figure 3.2(b). However, the measured coefficient of discharge varies slightly from this result: for a coefficient of velocity typically between 0.95 and 0.98 for a sharp edged orifice [54], the coefficient of discharge is worst 0.681. This deviation of 6.9% from the theory predicted value does however seem to lie within the resonable range of experimental scatter shown in Figure 3.2(b). The difference in results is most likely attributed to the interpenetrating fluids assumption of the

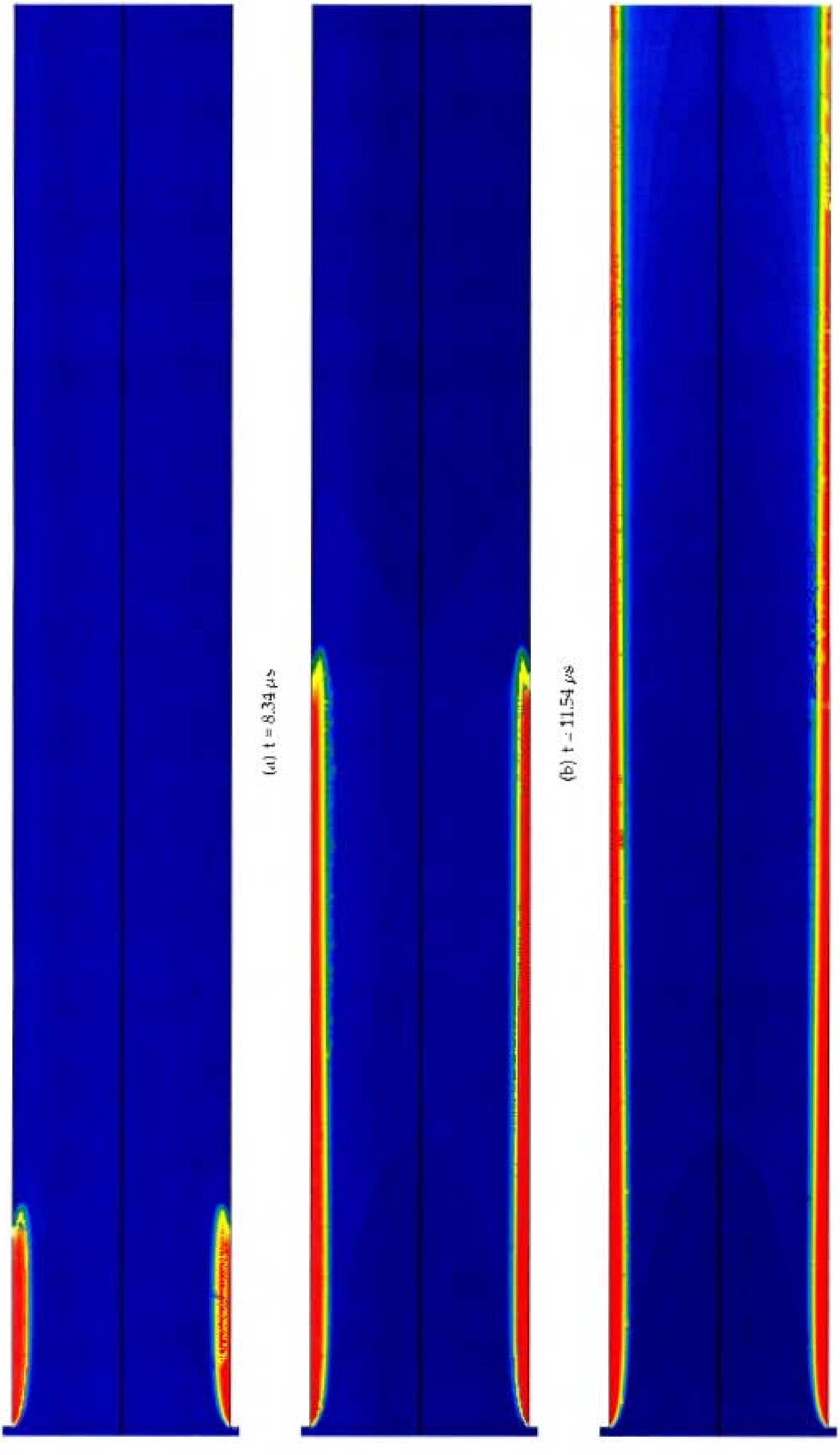

(a) t = 8.34 μs

(b) t = 11.54 μs

(c) t = 14.91 μs

Figure 6.4: Vapour phase [Coloured by volume fraction]

mixture multiphase model, since the liquid-vapour interface is not well defined. However, the selection of turbulence model and discretisation scheme can also affect this result [33].

A plot of the axial velocity of flow exiting the nozzle is shown in Figure 6.5 at various times. The velocity profile of this exhibited in this graph is clearly that of a fully-turbulent nozzle. It is observed from the plot that the boundary layer thickens as the mass flow rate and average exit velocity increases.

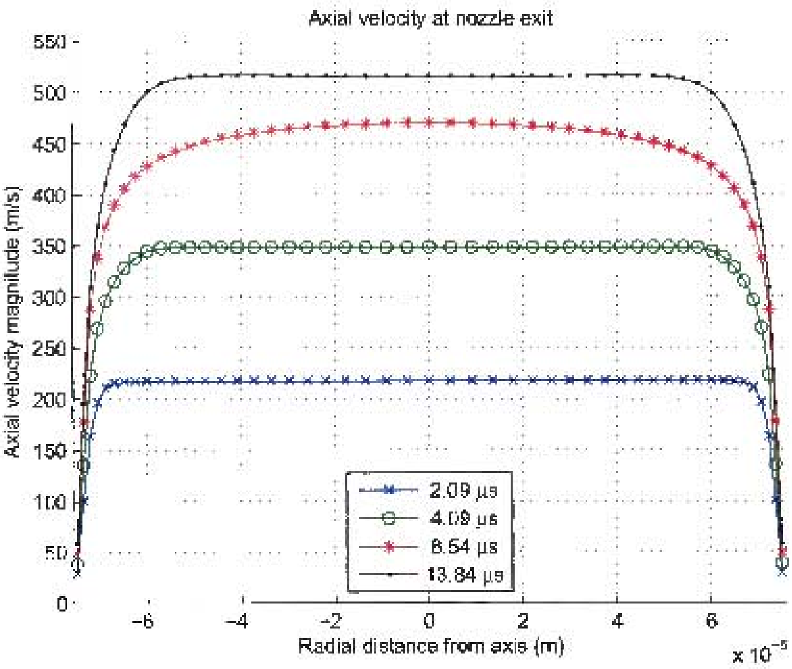

Figure 6.5: Axial velocity along the nozzle

For this axisymmetric case, the vapour essentially forms an annulus through which the liquid is discharged. The effect of this is not seen sooner in Figure 6.1, since the quality of the fuel that is discharged before the vapour reaches the exit is maintained. This implies that high-velocity liquid that was present in the nozzle before the formation of the cavitation bubble discharges through the entire cross-sectional area of the nozzle up to approximately 13.5 μs.

Furthermore, there is a slight perturbation in the exiting flow, where some flow reversal is predicted. This may be a function of the oversimplification of the nozzle geometry, since no outlet chamber is modelled, but is possible due to the occurrence of " hydraulic flip". Once the vapour has been transported to the end of the nozzle, the flow field takes on a steady nature. There are no further changes in the flow field, and a equilibrium between vapour generation and transport is maintained as long as the pressure difference between inlet and outlet remains constant.

In summary, five distinct flow conditions are present in this geometry. These are when

1. flow is initiated and acceleration of the fluid commences
2. fluid separates locally from the nozzle wall and a *vena contracta* forms
3. cavitation inception commences due to the low-pressure core of the separation vortex

4. vapour is generated at the nozzle wall and is subsequently transported towards the nozzle exit
5. the advected vapour reaches the nozzle exit and an equilibrium between vapour generation and transport is achieved.

6.2 Effect of fuel density

The effect of changing the density of the fuel present in- and flowing through- the nozzle is shown in Figure 6.6 and Figure 6.6. Table 6.7 lists the Reynolds head for each simulation, as well as the final mass flow rate and volume flow rate through the nozzle exit for each case. The data extracted from each simulation is compared to that predicted by one-dimensional theory and Nurick's Nozzle theory, described in Section 3.1 and Section 3.2 respectively.

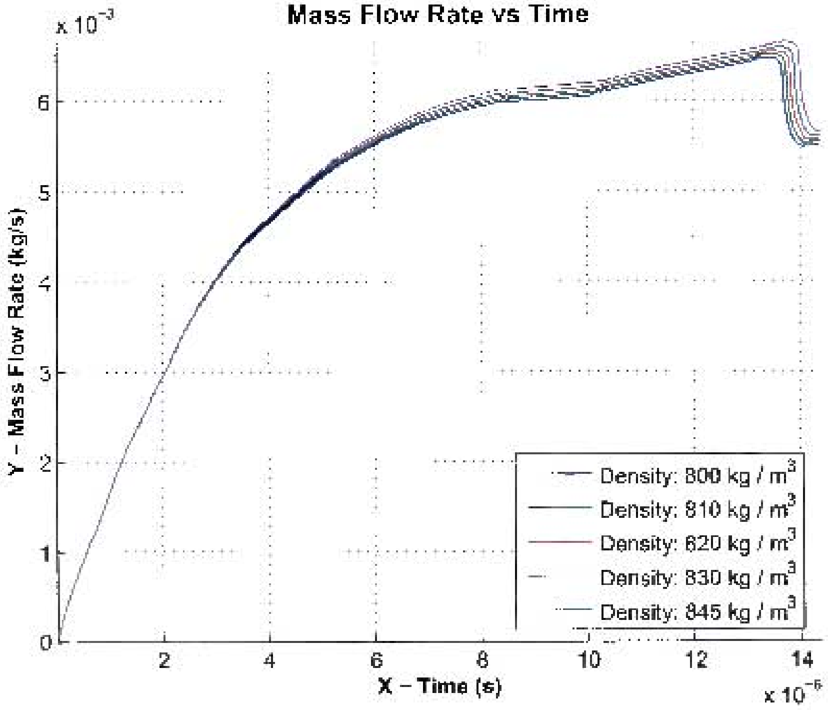

Figure 6.6: Mass flow rate vs. Time for varying density

	Simulation data					One-dimensional theory		Nurick's theory	
Density	Re_h	Final MFR	Final VFR	C_c	v_e	C_c	v_e	C_c	v_e
kg/m^3		kg/s	cm^3/30s		m/s		m/s		m/s
800	21762	5.520e-03	207.00	0.717	513.46	0.638	612.37	0.611	639.04
810	21898	5.554e-03	205.71	0.717	510.81	0.638	608.57	0.611	635.09
820	22032	5.585e-03	204.34	0.717	507.25	0.637	604.85	0.611	630.84
830	22166	5.615e-03	202.97	0.717	504.32	0.637	601.19	0.611	626.61
845	22366	5.665e-03	201.11	0.717	499.91	0.637	595.85	0.611	620.86

Table 6.1: Results - Variation of density

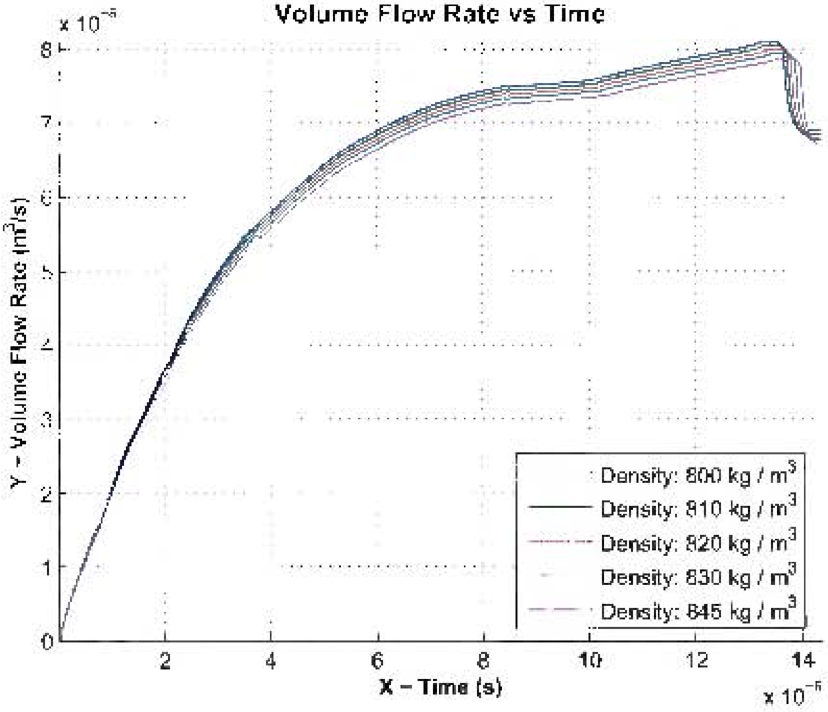

Figure 6.7: Volume flow rate vs. Time for varying density

The results clearly indicate that an increase in fuel density results in an increased mass flow rate, but a reduced volume flow rate for the nozzle. This is due to momentum effects and the mass of the stationary fluid in the nozzle. It is interesting to note that there is such a clear distinction between results even though the difference between the most and least dense fuels tested was only 6%.

It takes longer for the greater mass of fluid to accelerate to a given velocity than the less dense fluid. At any given time between the start of injection and the full development of cavitation, it was observed that the more dense fluid had a lesser exit velocity than the less dense fluid; a confirmation of the effect of momentum on development. However, the increase in density compensated for the reduced exit velocities and resulted in an overall increased mass flow rate at any given time.

It was observed in Figures 6.6, 6.7 that the advection of vapour formed by cavitation mechanisms is more rapid in lower density fluids than in high density fluids. To reiterate, vapour formation occurs after 4.5 μs. It takes a further 9.0 μs for the vapour to reach the exit and the flow to attain a steady state when the fluid has a density of 800 kg/m^3, as opposed to 9.5 μs for the 845 kg/m^3 fluid. The time at which cavitation initiation occurs is roughly the same in both cases. This implies that the vapour accelerates down the nozzle quicker for lower density fuels. This can be explained by the zero drift velocity approximation between the vapour and liquid, and the greater acceleration of lower density fluid through the nozzle.

6.2.1 Discussion of simulation and theoretical results

It is observed that the mass weighted average axial velocity determined in FLUENT® is always less than that predicted by the one-dimensional theory and Nurick's theory. This is because the contraction coefficient seen in the simulations is significantly greater than the theoretical or experimental predictions. A reason for this is occurring may be because of the interpenetrating fluid assumption of the mixture model. No definitive vapour-liquid interface is present, which makes accurate determination of the contraction coefficient directly from simulation results difficult. This lack of a clear interface also allowed the liquid mass to be spread over a greater radius at the exit, resulting in lower average exit velocities than that predicted by one-dimensional theory or Nurick's theory.

Both of these theories assume the liquid to exit as a jet core with a clear distinction between fluid phases. The difference in liquid jet diameters between the simulation and one-dimensional theory are 6.1%, while Nurick's theory predicts a jet that is 8.3% smaller in diameter than the simulation result. Similar differences occur for all simulations discussed in this chapter, and is not necessarity highlighted or elaborated on in later text.

6.3 Effect of fuel viscosity

Figure 6.8 shows the mass flow rate through the nozzle exit for fuels of varying viscosity. A detailed view of the mass flow rate for the last 2 μs of each simulation is also shown. Table 6.2 presents the simulation output data and corresponding predictions.

	Simulation data					One-dimensional theory		Nurick's theory	
Viscosity	**Re$_h$**	**Final MFR**	**Final VFR**	**C$_c$**	**v$_e$**	**C$_c$**	**v$_e$**	**C$_c$**	**v$_e$**
kg/m/s		**kg/s**	**cm^3/30s**		**m/s**		**m/s**		**m/s**
0.001666	44172	5.627e-03	203.37	0.729	493.53	0.638	601.20	0.611	627.85
0.0020	36795	5.633e-03	203.60	0.721	495.84	0.639	601.20	0.611	628.55
0.00225	32707	5.621e-03	203.17	0.721	497.28	0.637	601.24	0.611	627.18
0.0025	29436	5.614e-03	202.93	0.721	499.30	0.637	601.19	0.611	626.49
0.0030	24530	5.616e-03	202.99	0.717	502.43	0.637	601.19	0.611	626.67
0.00332	22166	5.615e-03	202.97	0.717	504.32	0.637	601.19	0.611	626.61
0.0035	21026	5.618e-03	203.06	0.713	505.09	0.637	601.19	0.611	626.88
0.003735	19703	5.619e-03	203.08	0.709	506.35	0.637	601.19	0.611	626.97

Table 6.2: Results - Variation of viscosity

It is clear from the results that altering the viscosity of the liquid fuel results in substantially varying cavitation characteristics. Less viscous fluid, with a higher Reynolds number, tended to cause a less constricted nozzle, represented by the increased contraction coefficient. It was observed that by reducing the viscosity from the base property of 0.00332 kg/m/s, the vapour that formed at the nozzle entrance reached the exit sooner than the that of the more viscous fluid. When the dynamic viscosity was halved, the time that it took for the nozzle to reach the "flipped" state was reduced by roughly 1.5 μs, which represents nearly 10% of the original flow time.

Similarly, increasing the viscosity from the base property reduced the time that it took for the advected vapour to reach the nozzle exit. However, the effect of increasing the viscosity is substantially smaller than reducing it. This could be attributed to the fact that an increase of up to only 12.5% was tested, while viscosities of up to 50% less were also tested.

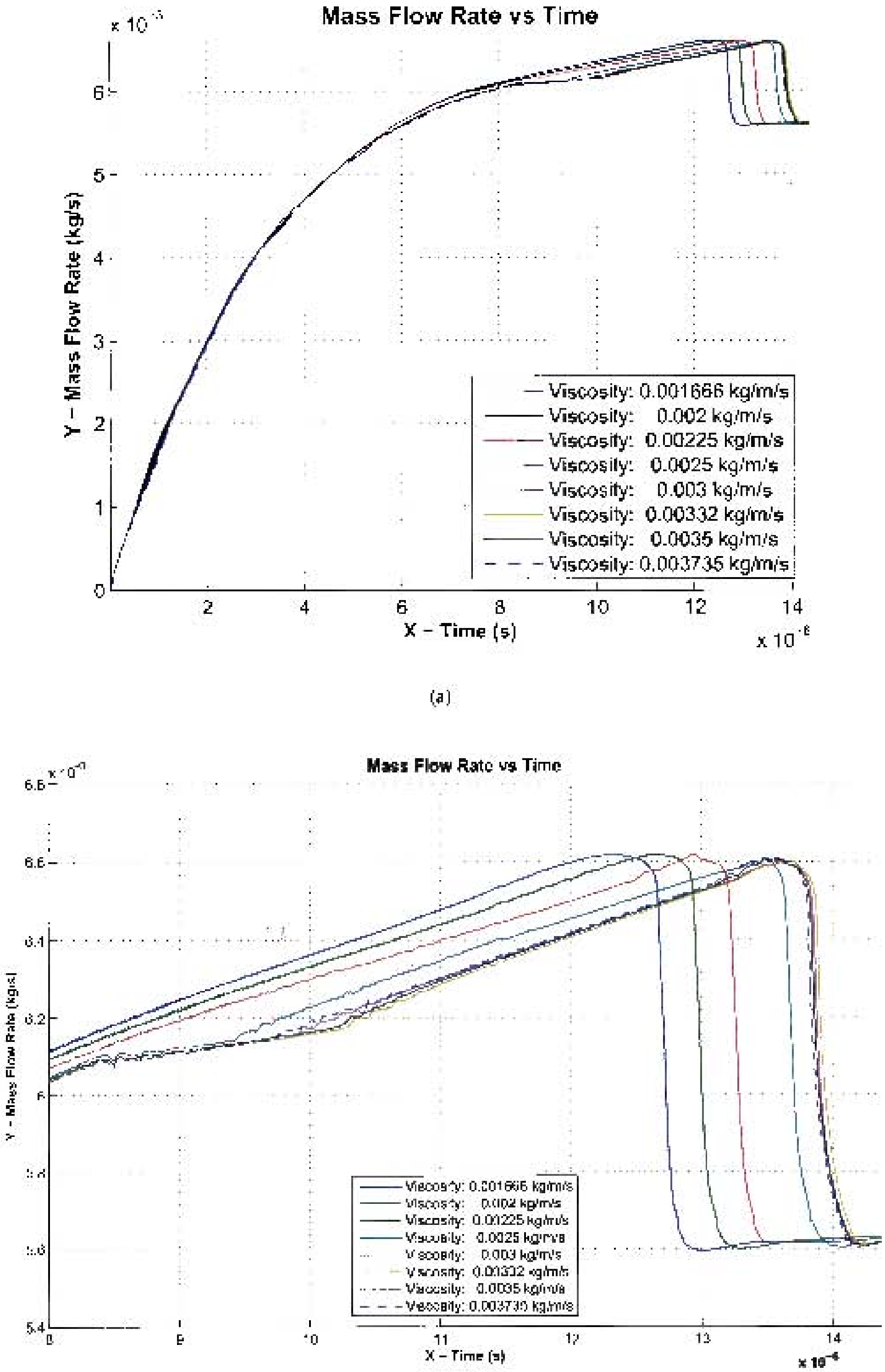

(a)

(b)

Figure 6.8: Mass flow rate vs. Time for varying viscosity

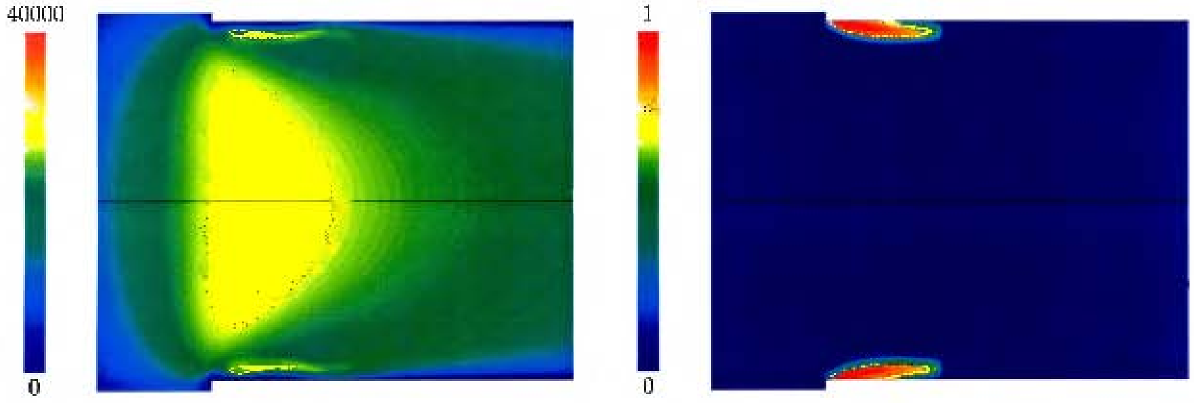

(a) $\mu = 0.001666$ kg/m/s [Contours of turbulent kinetic energy (m^2/s^2)]

(b) $\mu = 0.001666$ kg/m/s [Contours of vapour fraction]

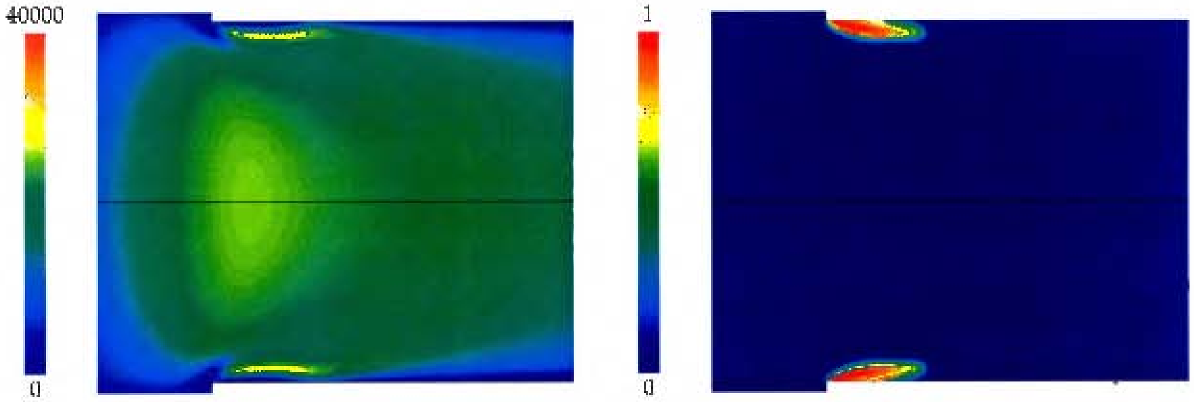

(c) $\mu = 0.00332$ kg/m/s [Contours of turbulent kinetic energy (m^2/s^2)]

(d) $\mu = 0.00332$ kg/m/s [Contours of vapour fraction]

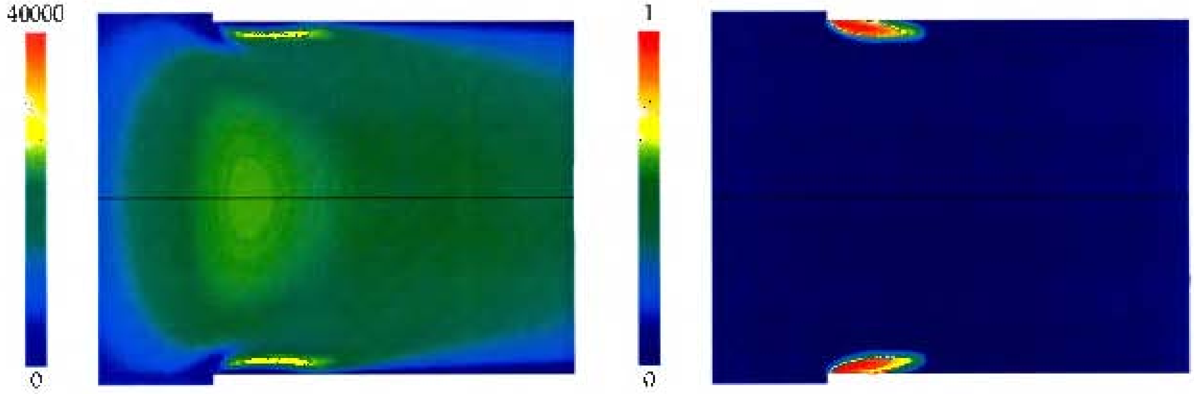

(e) $\mu = 0.003735$ kg/m/s [Contours of turbulent kinetic energy (m^2/s^2)]

(f) $\mu = 0.003735$ kg/m/s [Contours of vapour fraction]

Figure 6.9: Varying viscosity fluids at t = 6.34 μs

Figure 6.9 is useful in explaining the abovementioned phenomenon. As seen in Equation 4.9, the local rate of vapour formation has a square root dependence on the local turbulent kinetic energy. It is observed in the figure that the turbulent kinetic energy in the region of vapour formation is substantially higher for the low viscosity fluid in comparison to the standard fluid. Similarly, when the viscosity of the liquid is increased, the local turbulent kinetic energy decreases. A similar trend relating the Reynolds number to turbulent kinetic energy has been observed experimentally [10]. The maximum values observed in the at 6.34 μs are 38400 m^2/s^2, 30600 m^2/s^2 and 31500 m^2/s^2 for the 0.001666 kg/m/s, 0.00332 kg/m/s, and 0.003735 kg/m/s fluids respectively. At this point in time, it is therefore expected that the lower and higher viscosity fluids are undergoing increased vapour formation in comparison to the fluid of standard specifications. The increased generation of vapour mass explains the decrease in time that it takes for the "flipped" state to be attained.

At this point, it is worthwhile to note that the standard k-ϵ model tends to over-predict the production of turbulent kinetic energy, k, when applied to a flow-field with impingement [55, 56]. However, since the the flow entering the nozzle separates as opposed to striking the nozzle wall, results influenced by turbulent kinetic energy should not be heavily affected by this shortcoming of the turbulence model.

6.4 Effect of vapour surface tension

The result of altering the surface tension of the liquid was determined for a wide range of surface tensions, each within a reasonable range of the average diesel property. Figure 6.10 and Table 6.3 show no significant difference between results.

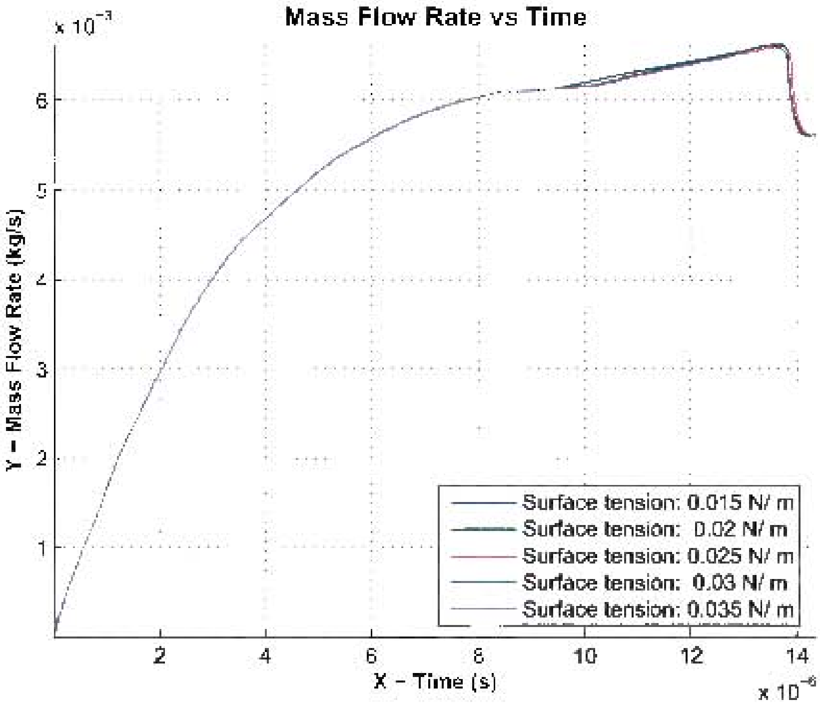

Figure 6.10: Mass flow rate vs. Time for varying surface tension

Figure 6.10 illustrates that the surface tension of the cavities does not affect the rate of advection of vapour

	Simulation data					One-dimensional theory		Nurick's theory	
Surface Tension	Re_h	Final MFR	Final VFR	C_c	v_e	C_c	v_e	C_c	v_e
N/m		kg/s	cm^3/30s		m/s		m/s		m/s
0.015	22166	5.616e-03	202.98	0.721	503.69	0.637	601.19	0.611	626.66
0.020	22166	5.616e-03	203.00	0.717	503.69	0.637	601.19	0.611	626.70
0.025	22166	5.615e-03	202.97	0.717	504.32	0.637	601.19	0.611	626.61
0.030	22166	5.621e-03	203.16	0.717	504.42	0.637	601.19	0.611	627.21
0.035	22166	5.622e-03	203.22	0.713	504.62	0.638	601.20	0.611	627.38

Table 6.3: Results - Variation of surface tension

from the cavitating region. A variation in surface tension has no effect on the mass flow rate through the nozzle, and the time at which the vapour reaches the nozzle exit remains unchanged.

The simulation results in Table 6.3 indicate that a decrease in surface tension results in an increased contraction coefficient. This suggests that under these conditions less vapour developed in the nozzle throat. This result is not repeated in the predictions of one-dimensional theory or Nurick's theory. This result is explained by Equation 4.9, which shows that the rate of vapour formation depends on the surface tension. A large change in surface tension should significantly change the rate of vapour formation, condition depending.

6.5 Effect of non-condensable gas fraction

Figure 6.11 and Table 6.4 outline the results of changing the non-condensable gas fraction of the bulk liquid injected through the nozzle.

	Simulation data					One-dimensional theory		Nurick's theory	
NCG	Re_h	Final MFR	Final VFR	C_c	v_e	C_c	v_e	C_c	v_e
ppm		kg/s	cm^3/30s		m/s		m/s		m/s
5	22166	5.628e-03	203.44	0.717	506.38	0.638	601.20	0.611	628.06
10	22166	5.626e-03	203.36	0.717	505.63	0.638	601.20	0.611	627.80
15	22166	5.615e-03	202.97	0.717	504.32	0.637	601.19	0.611	626.61
30	22166	5.592e-03	202.12	0.717	500.19	0.634	601.17	0.611	624.01

Table 6.4: Results - Variation of non-condensable gas concentration

The results in Table 6.4 indicate no significant difference in cavitation formation in the nozzle. At this concentration of non-condensable gas fraction, the addition of more gas does not severely affect cavitation. It is observed that an increase in the NCG fraction results in a slightly lower mass flow rate, suggesting that the nozzle becomes slightly more constricted. This is not reflected in the measured coefficient of contraction.

It is known that the presence of contaminant gases in solution in the liquid can cause an increase in cavitation inception pressure. However, for a high-pressure nozzle, it is seen that the effects of turbulence on inception pressure are quite substantial. This is clearly a more significant contributor to the increase in inception pressure than the quantity of contaminant gas, particularly in refined diesel fuel which has a very low quantity of air dissolved in it.

It was observed that there was a significant increase in the rate at which the flow-field developed when the NCG mass fraction was reduced from 15ppm. When the liquid contained 5ppm of contaminant gas, the

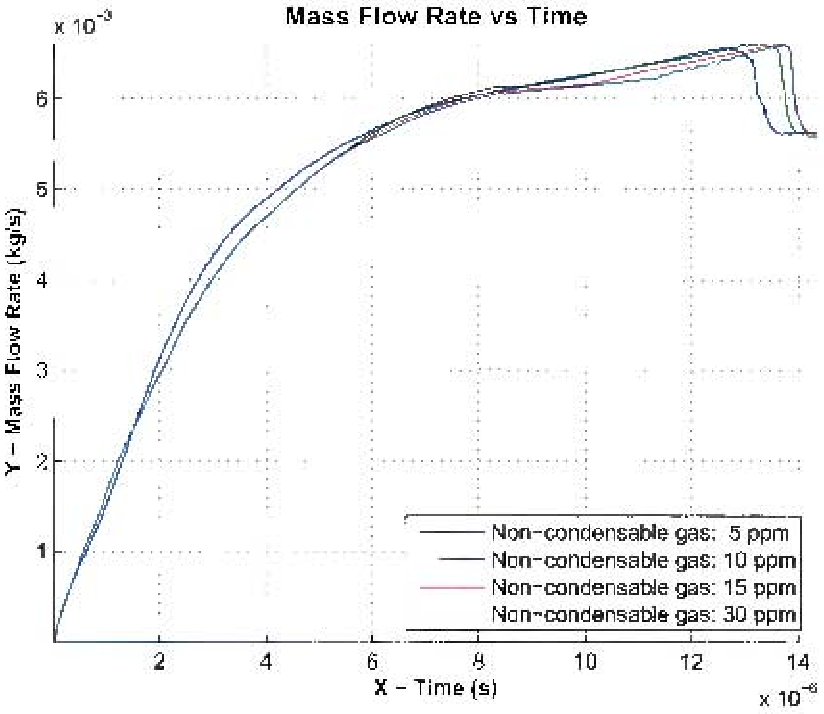

Figure 6.11: Mass flow rate vs. Time for varying non-condensable gas mass fraction

cavitation vapour was advected to the nozzle exit in approximately 0.75 μs less time than when 15ppm NCG was present.

A limitation of the cavitation model used in FLUENT® is that the non-condensable gas fraction is considered constant throughout the domain [4]. The contaminant gas, treated as an ideal gas by FLUENT®, adds an artificial compressibility to the liquid. The pressure in the domain not only drives the flow, but it also compresses the bubbles simulated in each control volume.

The compressibility of the contaminant gases explains the difference in results shown in Figure 6.11. When very little contaminant gas is dissolved in the liquid, the liquid is more incompressible than when a large mass of NCG is present in the fluid. This allows the flow to accelerate more rapidly when a pressure is applied at the nozzle inlet, and results in decreased flow development time.

6.6 Effect of nozzle inlet curvature

The addition of a fillet radius on the inlet corner of the nozzle greatly affects the cavitation that occurs within the nozzle. The pressure loss across the entrance to the nozzle can be substantially reduced if the inlet is sufficiently rounded. It was observed that this can lead to the absence of flow separation and cavitation. When the inlet is not sufficiently rounded to entirely cease the formation of cavitation, it has the effect of delaying the onset of vapour formation until the fluid speed around the inlet is sufficient to promote flow separation.

Not only does the time to inception increase, but the amount of vapour present in the nozzle decreases as the inlet radius increases. The decreased pressure loss allows the vapour to dissolve back into the liquid. This means that the nozzle doesn't attain a state of "hydraulic flip", and there is no constriction or loss in flow area at the nozzle exit. For this reason, a greater mass flow rate is observed through the nozzle when the inlet is rounded. This is depicted in Figure 6.12. Note that the mass flow rate through the nozzles that have an inlet fillet are, for all intensive purposes, identical.

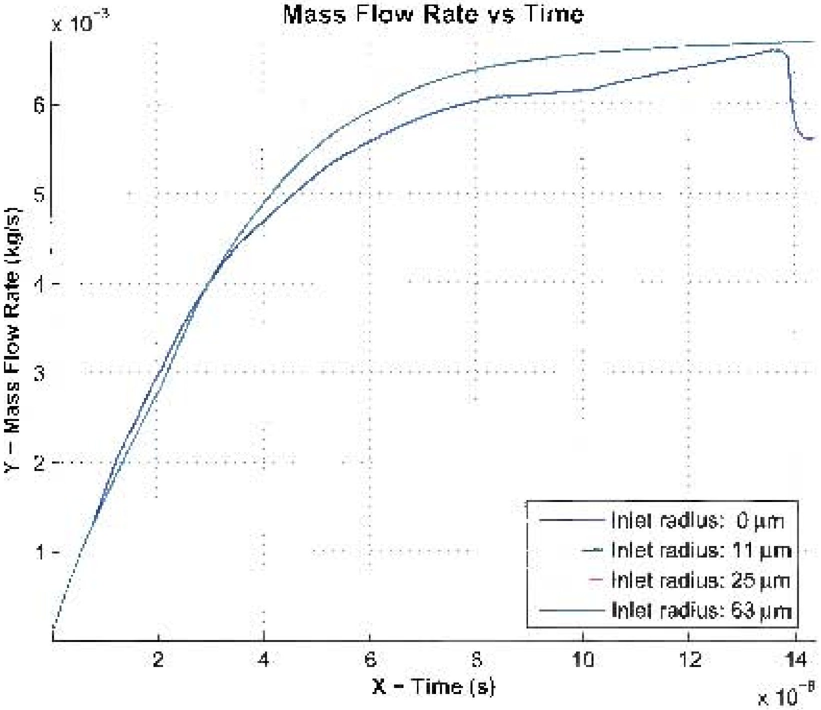

Figure 6.12: Mass flow rate vs. Time for varying inlet radius

The difference in the appearance of the vapour space at the nozzle entrance is shown in Figure 6.13. These results align well with the empirical predictions made by Nurick regarding the state of nozzle. It is clear that the extent to which the vapour constricts the nozzle and advects downstream decreases as the inlet fillet increases in radius. Vapour formation can cease entirely if the edge is sufficiently rounded. The critical radius for a 150 μm diameter nozzle and Re$_h$ of 22166 is predicted, according to Equation 3.8, to be 36.9 μm. Equation 3.6 predicts that no flow separation can occur when the inlet radius is greater than 21 μm. Hydraulic flip cannot occur when the radius is greater than 7.5 μm.

Table 6.5 presents the results of the inclusion of various inlet corner fillets and the predictions made by Nurick's empirical formulae and one-dimensional theory.

It was determined that Nurick's equation describing the coefficient of contraction, namely Equation 3.6, deteriorates in accuracy for this experimental setup. When a $\frac{r}{d}$ of greater than 0.147 is present, a coefficient of contraction of greater than 1 is predicted. This is a physically impossible result, since a C_c of unity represents an unconstricted flow.

For this reason, for the case when a radius of 25 μm was used, a coefficient of contraction of greater than 1 is predicted. In this case, the C_c was considered the same as that for single phase, although cavitation did occur as predicted. This is done because the separation and subsequent throttling effect at nozzle entrance due to the presence of a *vena contracta* was observed to be minimal.

	Simulation data					One-dimensional theory		Nurick's theory	
Inlet radius	**Re_h**	**Final MFR**	**Final VFR**	**C_c**	**v_e**	**C_c**	**v_e**	**C_c**	**v_e**
μm		**kg/s**	**cm^3/30s**		**m/s**		**m/s**		**m/s**
0	22166	5.615e-03	202.97	0.717	504.32	0.637	601.19	0.611	626.61
11	22166	6.706e-03	242.38	0.825	471.26	0.760	601.19	0.737	586.46
25	22166	6.706e-03	242.38	0.939	481.62	0.760	601.19	1.000	457.20
63	22166	6.706e-03	242.38	1.000	490.79	0.760	601.19	1.000	457.20

Table 6.5: Results - Variation of nozzle inlet radius

6.6.1 Discussion of simulation and theoretical results

There is an enormous difference between the simulation results and the contraction coefficients predicted by theoretical mechanisms. Whereas Nurick's empirical theory accounts for the rounding of the orifice inlet, the idealised flow based one-dimensional theory does not.

One-dimensional theory assumes that a *vena contracta* will form, regardless of the geometry of the nozzle. No flow separation was present when the inlet radius was set at 63 μm. It is this fundamental assumption that explains the constant coefficient of contraction seen in Table 6.5. Since little or no separation is present when the inlet radius is increased up to 63 μm, the contraction coefficient value predicted by one-dimensional theory become less accurate.

Nurick's theory uses empirical data to formulate correlations between the degree of inlet rounding and decreased flow separation. For this reason, the results predicted by the theory reflect more realistic predictions for the contraction coefficient than one-dimensional theory. It was however observed that the empirical constants determined for use in Equation 3.6 did not allow for the maximum ratio of inlet fillet radius to diameter used in the injector nozzle, and was therefore a cause of erroneous results.

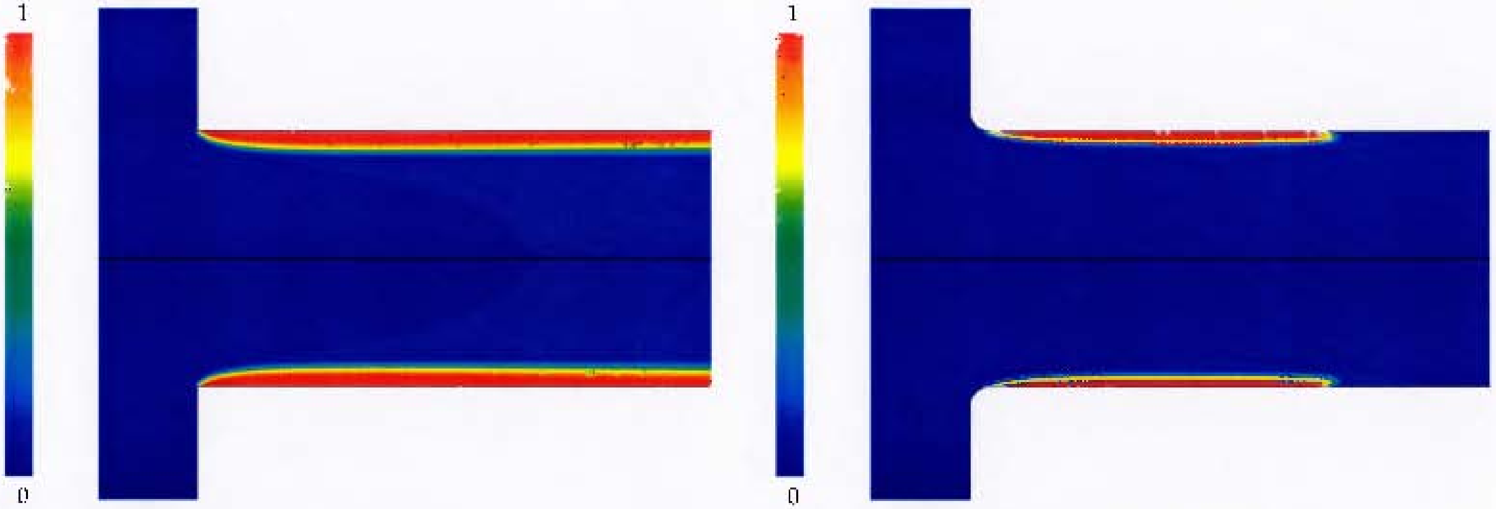

(a) Square inlet, t = 14.365 μs (b) 11 μm radius, t = 14.365 μs

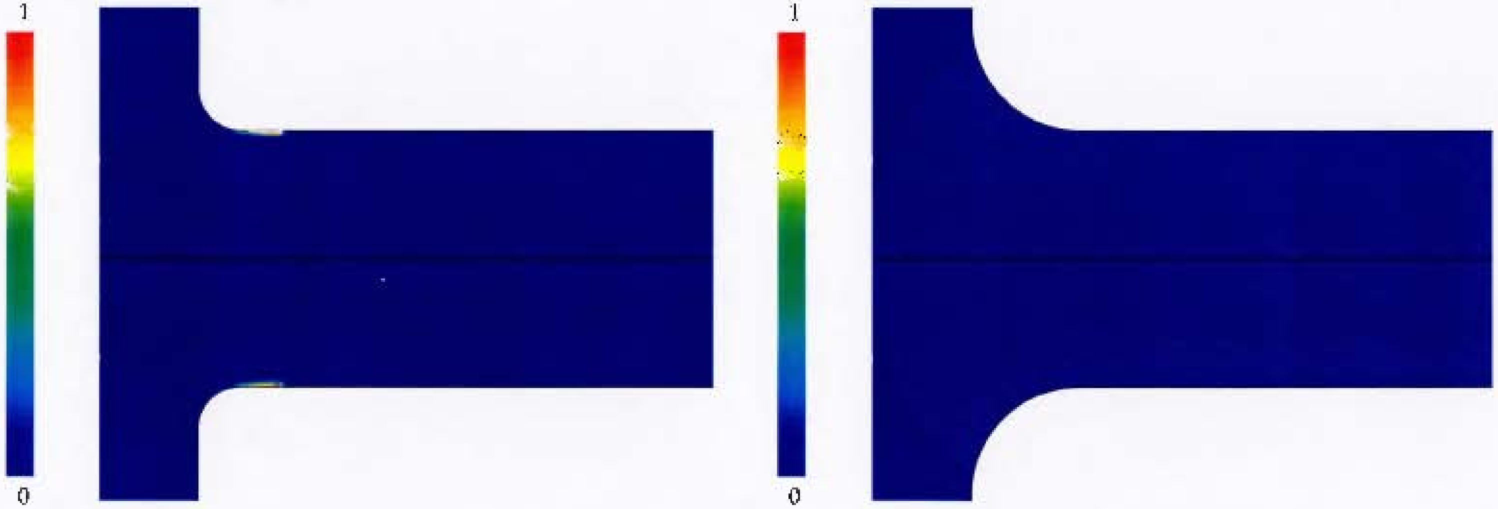

(c) 25 μm radius, t = 14.340 μs (d) 63 μm radius, t = 14.365 μs

Figure 6.13: Vapour phase for varying inlet radius [Coloured by vapour fraction]

6.7 Temperature effects

It is conjectured that thermal cracking is the mechanism for deposit formation in diesel fuel injectors. At temperatures of over 1000°K, chemical decomposition of long-chain hydrocarbons that make up the fuel is possible. It is speculated that this phenomenon only occurs upon the collapse of the vapour cavities. The generation of a thermal profile for the formation of vapour and the vapour cavity before collapse assists in the prediction of the initial temperature of the vapour bubble upon collapse.

Figure 6.14 shows the temperature distribution within the nozzle after 23 μs. Since the vapour was modelled as an ideal gas, the time taken for vapour generation and advection increased. However, since the vapour development and time-scale of the flow development is the same as for when temperature effects were not considered, the result is still considered to be representative and comparable to previous results.

It was observed that a thermal boundary layer exists along the nozzle wall. The temperature of the fluid increases in this region due to the presence of shear stresses in the boundary layer. Most noticeable however is the high-temperature region slightly downstream of the region of vapour formation. Again, the presence of high shear stresses in this gaseous region are the cause of the temperature increase as the vapour is forced to undergo a direction change and advect downstream. The temperature in this region is close to 500°K, a considerable increase of 140°K in comparison to the inlet fluid temperature.

Overall, the average total temperature of the fluid exiting the nozzle was 362.1°K. The static temperature was determined to be 472.9°K, representing an increase of 110.8°K of the inlet fluid. This result correlates fairly well with MacDonald [21], who recorded a temperature increase of 80°K (with an error margin of ±10°K) of fluid pressurised to 1500 bar flowing through a fuel-injector. The discrepancy in results can be attributed to the simplification of the geometry and decrease in distance between the inlet and outlet, the reduction in number of direction changes that the fluid must make, as well as the substantially reduced time-scale over which the simulation is performed. All of these factors could affect the exit velocity of the fluid, and therefore the increase in static temperature due to increased kinetic energy.

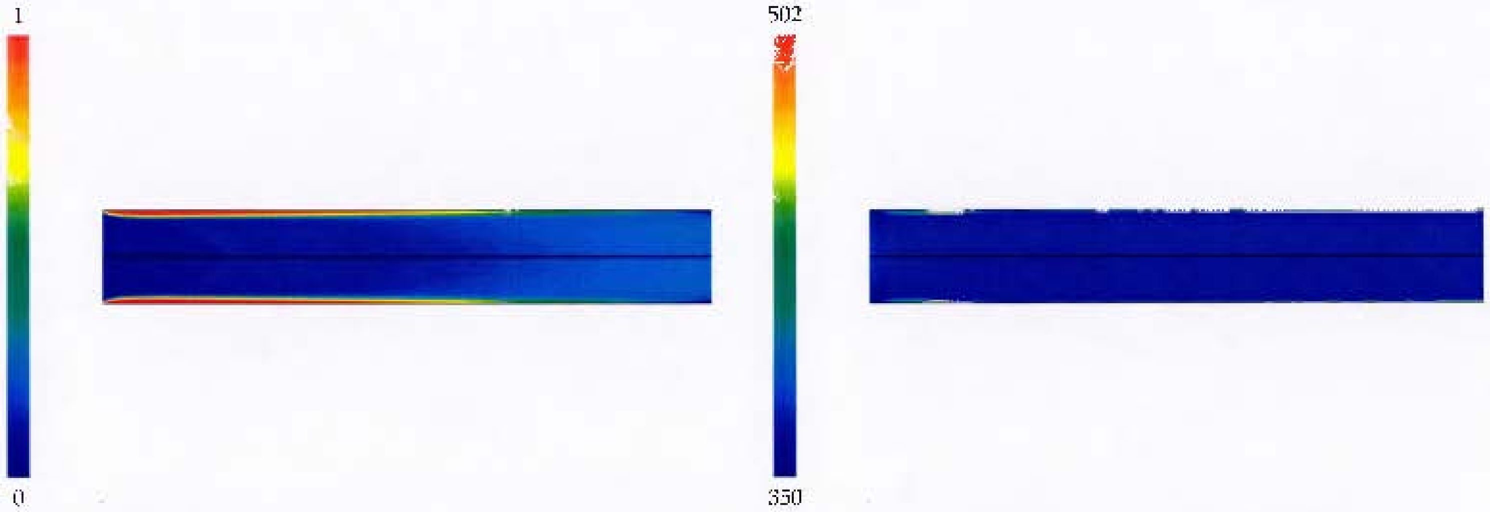

(a) Vapour phase [Coloured by vapour fraction]

(b) Total temperature [Coloured by total temperature (K)]

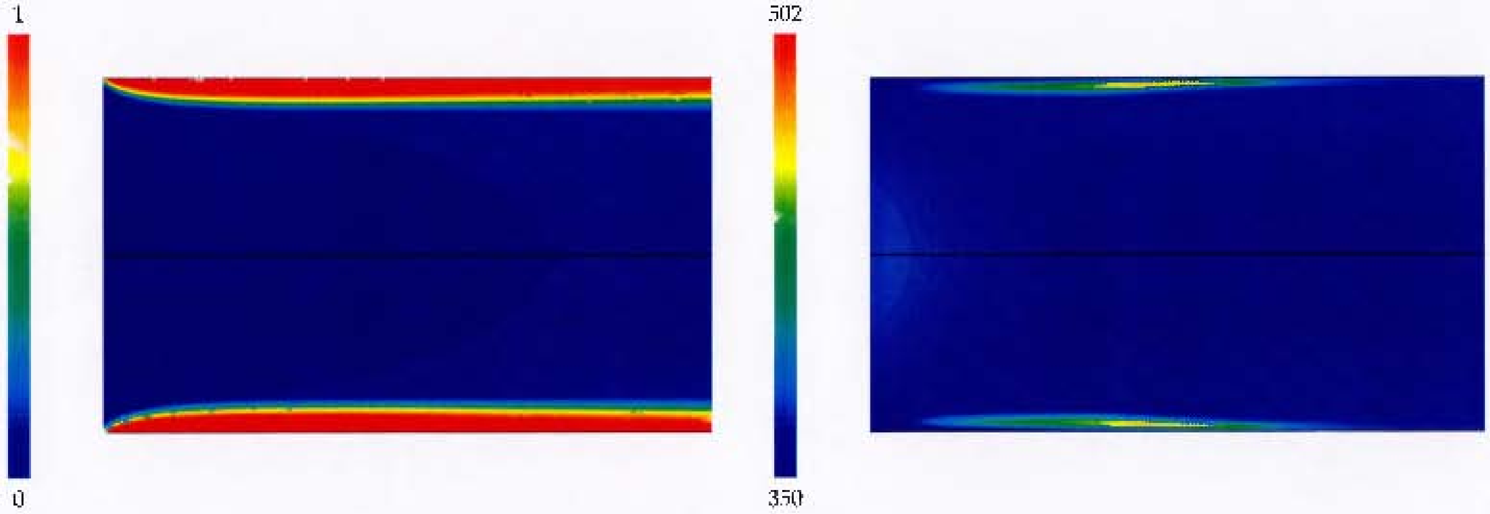

(c) Vapour phase [Coloured by vapour fraction]

(d) Total temperature [Coloured by total temperature (K)]

Figure 6.14: Thermal model after 23 μs

7. Bubble collapse

7.1 Base conditions

A general discussion of the collapse of a vapour space is given in this section. The fluid properties that describe the base conditions for testing are given in Appendix F. The temperature of the surrounding liquid was 360°K.

Figure 7.1 shows the radius of the idealised vapour space with respect to time. The time duration that elapsed between the initiation of compression and when the bubble reached its minimum dimensions was approximately 0.0661 μs. For most of this time, the bubble was reducing in mass because of the diffusion of vapour out of the bubble into the surrounding liquid. The actual compression of the non-condensable gases occurred on much smaller time scale, the duration of which was only 0.2029 ns. The bubble clearly undergoes rapid acceleration towards the end of the diffusion process.

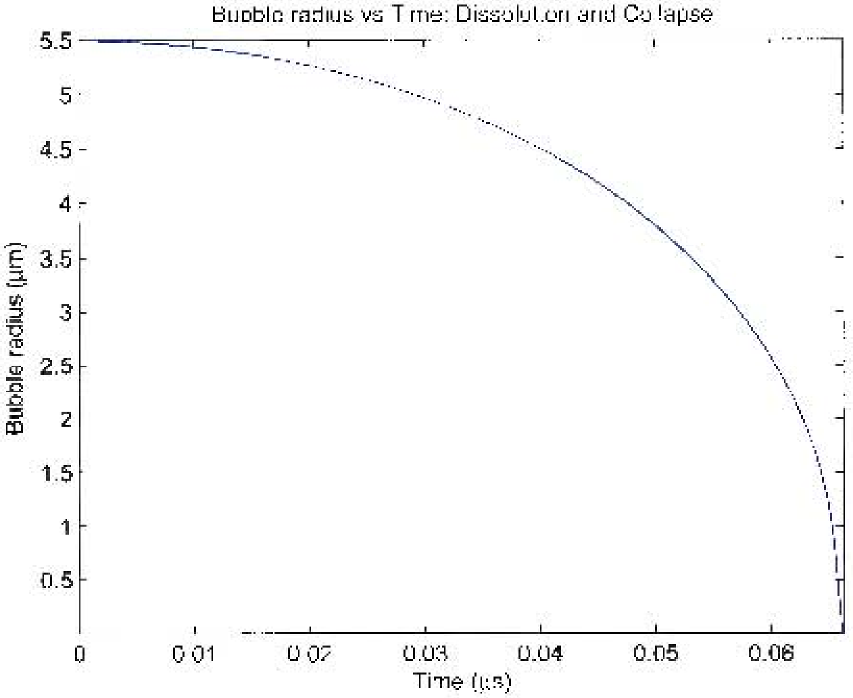

Figure 7.1: Base results: Radius vs Time

The time-scales involved in the collapse of the vapour space are very small. This is mainly due to the large pressure difference between the vapour and its surrounding liquid. Figure 7.2 demonstrates that, even though the liquid pressure is very large, the bubble expands after it collapses to its minimum radius. This is because the compression of the bubble causes the gas in the bubble to be compressed to up to 25000 bar. The rebound process occurs over a substantially larger time interval than the collapse stage. This is because the liquid resists the expansion of the bubble. The bubble eventually attains an equilibrium radius of approximately 14 nm.

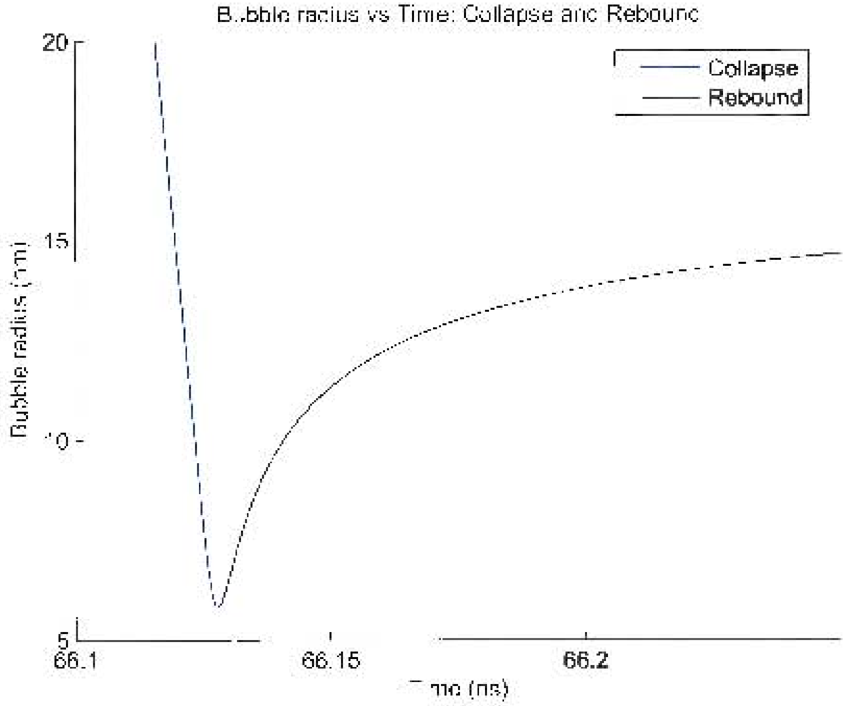

Figure 7.2: Base results: Radius vs Time during collapse and rebound stages

The temperature of the bubble during the collapse and rebound phases is shown in Figure 7.3. The very sharp temperature rise of the bubble indicates that the bubble undergoes very rapid compression. This slow rebound process allows for rapid cooling of the gases, as the conduction distance is small and the temperature difference between the bubble and the surrounding liquid is high. The bubble temperature also decreases due to the expansion of the gases as the bubble radius increases. Overall, it is predicted that the bubble attains a temperature of over 1000°K for over 0.1 ns and exceeds 3000°K for 0.01 ns.

Figure 7.4 describes how the pressure of the bubble increases and decreases in comparison to the temperature of the bubble. It is clear that the temperature rise during the collapse phases is substantially more rapid than the temperature fall during the rebound phase. The line describing the adiabatic compression process from the initial temperature to the maximum temperature attained is also shown on the diagram. Comparing the gradients of the lines representing bubble collapse and the adiabatic curve, it is observed that as the temperature of the bubble increases, the thermodynamic state of the bubble changes from isothermal to adiabatic. This illustrates exactly how rapid the compression process is, that the bubble collapse occurs so quickly that nearly no energy is lost to the surrounding liquid.

The velocity of the collapse is plotted against the temperature of the bubble in Figure 7.5. The process is represented in an anticlockwise motion on the graph, starting with a bubble wall velocity of zero and the temperature equal to 400°K. Initially, the bubble loses energy to the surrounding environment due to con-

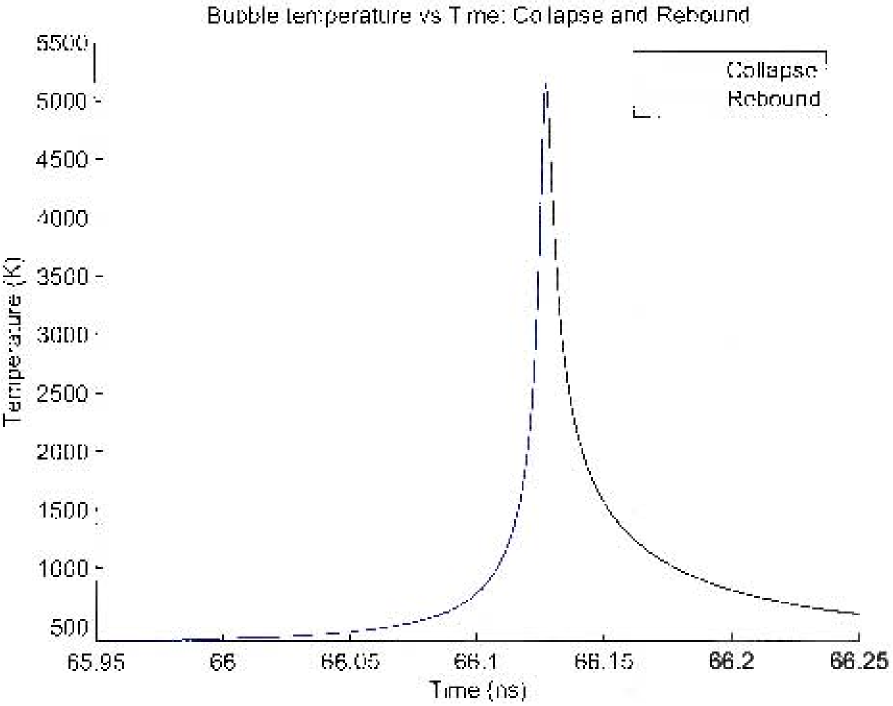

Figure 7.3: Base results: Temperature vs Time

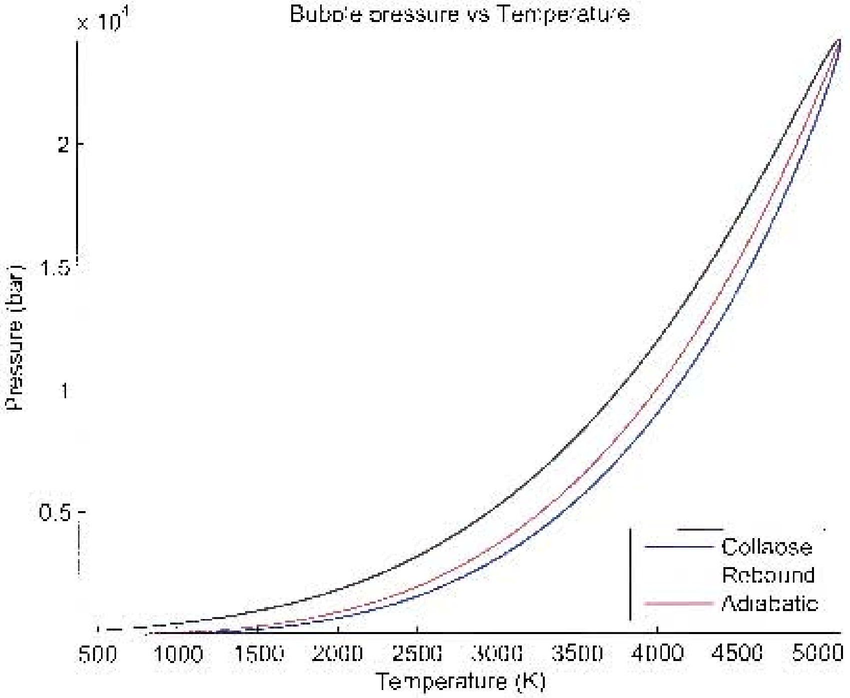

Figure 7.4: Base results: Pressure vs Temperature

duction and the diffusion of vapour into the surrounding liquid. The temperature drops fairly rapidly close to the liquid temperature because the bubble radius is large. The temperature then increases slightly as the velocity of the bubble wall increases and the work done on the bubble increases to a magnitude greater than the total energy lost.

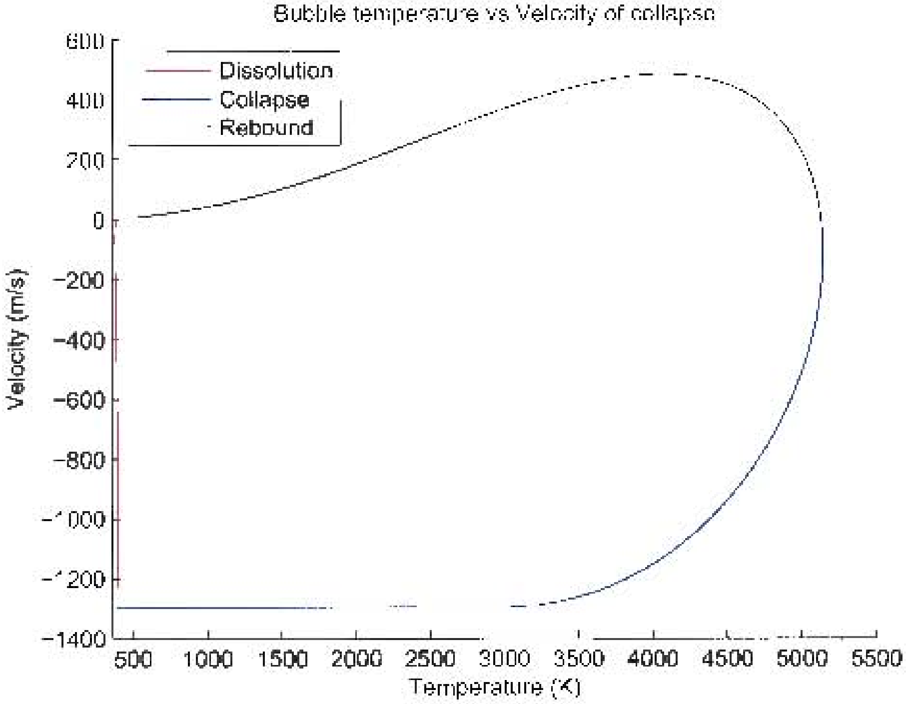

Figure 7.5: Base results: Temperature vs Velocity

The velocity of collapse increases rapidly until the bubble wall attains a velocity equal to that of the sonic velocity of the liquid. No further acceleration can occur, and the conduction of energy away from the bubble becomes dominant until all the vapour is diffused out of the bubble. The momentum of collapse is very high, causing the remaining air in the bubble to undergo rapid compression and the bubble temperature to quickly increases. The compression also increases the pressure in the bubble and the bubble wall undergoes a positive acceleration.

The maximum temperature is attained before the end of the process of collapse has been reached. At this point, conduction becomes dominant even though the bubble is still decreasing in size. This is due to the very small conduction distance and the large conduction coefficient of air at high temperature. The temperature decreases during expansion due to conduction and negative work taking place on the bubble.

7.2 Effect of initial conditions

A study was performed to check the sensitivity of the results attained to the change initial conditions. Tables 7.1 to 7.8 present the results of the study. Arrows indicate temperature directionality and sensitivity to parameter changes: a red arrow indicates a strong link between the parameter and the maximum temperature of collapse, and a blue arrow indicates a weak correlation. The following paragraph elaborates the description of the headings used in the results tables.

Initial temperature describes the temperature of the bubble at the end of the dissolution stage and the start of collapse. *Maximum temperature* is the maximum temperature attained during the entire collapse stage. *Time of collapse* is the total time between the start of the collapse and the time at maximum temperature. The average temporal temperature gradient is stated. This describes the rate of increase of temperature, and is used to better gauge which parameters have the greatest effect on the temperature increase of the bubble.

The initial conditions changed are quite self explanatory, in that each individual condition that may be altered during an experimental procedure is changed while other conditions are kept constant. One possibly obscure condition altered was the surface area coefficient, the results of which are shown in Table 7.8. This parameter represents a simple attempt to account for bubble warping and distortion of the bubble surface, which may lead to an increase in surface area over which greater conduction may occur. An increase in the surface area multiplier from 1 to 2 describes a situation where the effective bubble surface area is double that of a sphere of the given radius.

Bubble Temperature	Initial Temperature	Max Temperature	Time of collapse	dT/dt
K	K	K	ns	K/ns
360	383.9	4437.5	0.2031	19960.6
400	383.7	5148.4	0.2029	23482.0
450	383.5	6056.4	0.2027	27987.5
480	383.4	6602.4	0.2026	30700.2

Table 7.1: Variation of void initial temperature

Pressure	Initial Temperature	Max Temperature	Time of collapse	dT/dt
bar	K	K	ns	K/ns
40	383.6	5134.4	0.2034	23356.1
50	383.7	5148.4	0.2029	23482.0
75	384.0	5183.5	0.2017	23800.1
100	384.2	5219.9	0.2004	24125.4

Table 7.2: Variation of liquid pressure

Density	Initial Temperature	Max Temperature	Time of collapse	dT/dt
kg/m^3	K	K	ns	K/ns
800	384.2	5145.5	0.1992	23903.0
815	383.9	5147.1	0.2011	23690.7
830	383.7	5148.4	0.2029	23482.0
845	383.5	5149.1	0.2047	23277.5

Table 7.3: Variation of liquid density

Viscosity	Initial Temperature	Max Temperature	Time of collapse	dT/dt
kg/m/s	K	K	ns	K/ns
0.001666	383.7	6087.6	0.2030	28092.9
0.00225	383.7	5768.4	0.2030	26528.0
0.003	383.7	5337.4	0.2029	24411.8
0.00332	383.7	5148.4	0.2029	23482.0
0.003735	383.7	4901.3	0.2029	22267.2

Table 7.4: Variation of liquid viscosity

Surface tension	Initial Temperature	Max Temperature	Time of collapse	dT/dt
N/m	K	K	ns	K/ns
0.015	383.7	5145.5	0.2029	23468.5
0.025	383.7	5148.4	0.2029	23482.0
0.035	383.7	5151.1	0.2029	23495.8

Table 7.5: Variation of liquid surface tension

NCG	Initial Temperature	Max Temperature	Time of collapse	dT/dt
ppm	K	K	ns	K/ns
5	376.2	3664.9	0.1407	23375.7
15	383.7	5148.4	0.2029	23482.0
30	405.2	5626.2	0.2558	20412.1

Table 7.6: Variation of non-condensable gas (NCG) mass fraction

Initial radius	Initial Temperature	Max Temperature	Time of collapse	dT/dt
μm	K	K	ns	K/ns
1	365.1	590.8	0.0345	6546.1
2.5	370.8	2104.1	0.0920	18842.1
5.5	383.7	5148.4	0.2029	23482.0
8	395.7	6466.4	0.2951	20568.4

Table 7.7: Variation of initial bubble radius

Surface area multiplier	Initial Temperature	Max Temperature	Time of collapse	dT/dt
	K	K	ns	K/ns
1	383.7	5148.4	0.2029	23482.0
2.5	369.2	5492.0	0.2028	25262.0
5	364.7	5606.9	0.2027	25856.0

Table 7.8: Variation of bubble surface area

It has been observed that the variables that have the most profound effect on the maximum temperature attained for the collapse of a spherical vapour space are the initial bubble temperature, liquid viscosity, the non-condensable gas mass fraction and the initial bubble radius.

The initial temperature difference between bubble and liquid had a great effect on the temperature increase of the bubble. The time of collapse decreased as the initial temperature increased. The maximum temperature of collapse increased accordingly. This factor is, however, difficult to control as it is a function of the flow in the nozzle and not a physical parameter that can be altered.

Reducing the viscosity of the liquid can result in a significant increase in the collapse temperature. The viscosity has a profound effect on the acceleration of the bubble wall: a reduced viscosity liquid will cause less deceleration of the wall and result in a smaller bubble upon collapse. This also influences the rate of temperature increase by a considerable margin. The rate of temperature rise for a bubble immersed in a low viscosity liquid is significantly higher than that collapsing in a viscous fluid. Conversely, increasing the viscosity will result in a reduction the maximum temperature of collapse because the minimum radius of the bubble collapse is increased.

The initial mass of contaminant gases remains the same throughout the collapse process. When the volume of the gases decreases, the pressure experienced by bubble upon collapse decreases. The result is a decrease in temperature. The time of collapse also decreases significantly, because the pressure of the bubble does not resist the influence of the liquid. When the mass (and volume) of non-condensable gases was increased, the maximum temperature and rate of temperature rise increased.

The initial radius of the collapsing bubble has a significant effect on the maximum temperature achieved. Two factors are influencing this result, namely the volume of contaminant gases trapped in the bubble and the momentum of the collapse. Overall, the larger the bubble, the larger the volume of contaminant gases present after the vapour condenses out of the void. Furthermore, since there is more air present at the start of collapse, the momentum of the collapsing gas is greater, resulting in a greater compression of the gases. This culminates in a considerable increase in rate of temperature increase as well as the maximum temperature of collapse. It was observed that, in bubbles that were small enough, very low temperatures of the order of 500°K, that is below that of the thermal cracking margin, were attained.

Variation in liquid pressure, liquid density, surface tension and bubble surface area all showed marginal differences in results. Liquid pressures were altered to simulate the effect of increased combustion cylinder pressure due to turbocharging. The limits of fuel specifications for density and surface tension were tested. An increase in pressure, density, surface tension as well as surface area all showed directional increases in the maximum temperature of collapse.

The result of altering the bubble surface area is quite counter-intuitive. It appears that the temperature history of the bubble has plays a major role in the maximum collapse temperature.

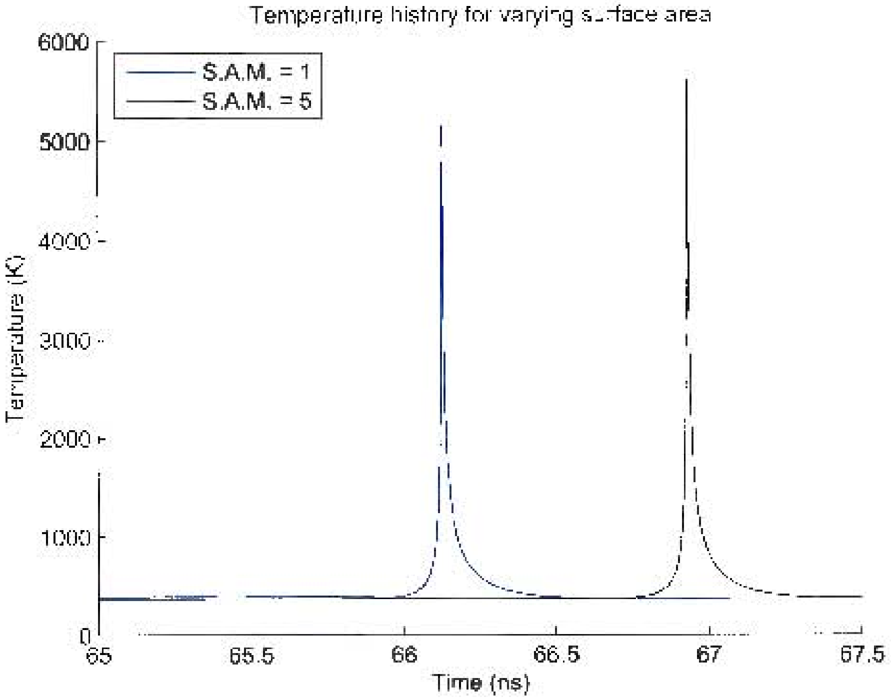

Figure 7.6: Temperature history for various surface area multipliers (S.A.M.)

A bubble with a larger surface area has a lesser temperature upon the initiation of the collapse stage, since it loses more energy by conduction; conversely, the smaller area bubble retains more energy since it is more

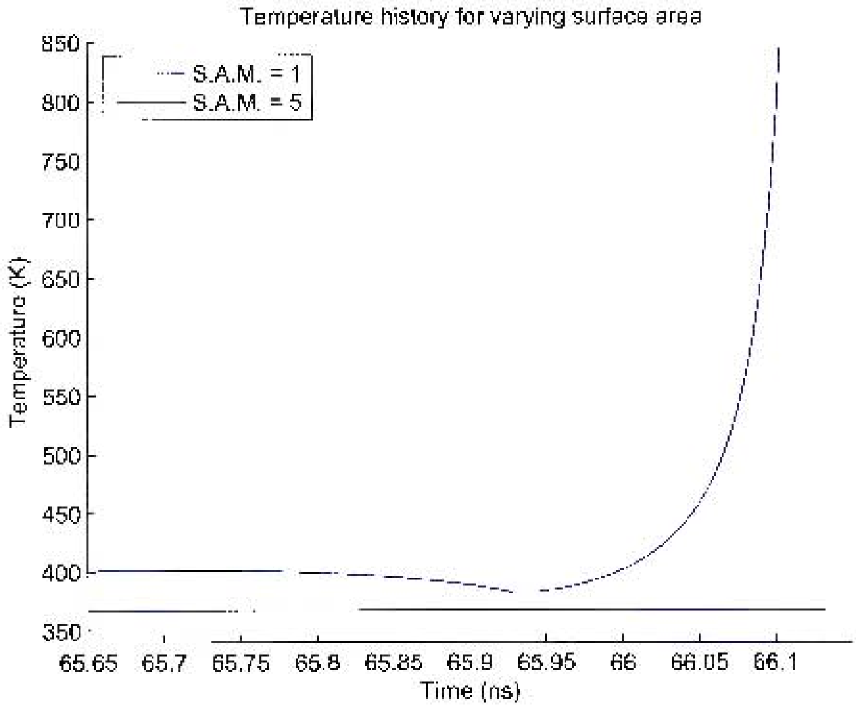

Figure 7.7: Temperature history for various surface area multipliers (S.A.M.) (enlarged)

insulated. Upon the commencement of collapse, the temperature of the bigger bubble increases almost immediately, since it is is near the liquid temperature. The small area bubble still has a relatively large negative conduction temperature gradient and continues to lose heat to the surrounding liquid by conduction. The temperature of the large area bubble soon increases to a temperature greater than that of the small area bubble, and the resulting increase in pressure causes a greater final temperature.

8. Overview of Results

The following are the conclusions can be drawn from the simulations of cavitation of diesel fuel in axisymmetric nozzles and the subsequent collapse of idealised spherical vapour spaces.

8.1 Prediction of cavitation in nozzles

Cavitation was present in all conditions predicted by both one-dimensional theory and Nurick's nozzle theory. Simulations predict discharge coefficients in the region of 0.68. This result correlates fairly well with experimental work and computational simulations.

Although it produced unrealistic results for certain ratios of inlet radius to nozzle diameter, Nurick's theory provided good forecast of the coefficient of contraction and exit velocity for nozzles with filleting on the inlet corner. However, the predicted results for sharp inlet nozzles did not correlate well to the simulation results. This is because the estimated coefficient of contraction for this condition is always set equal to the theoretical minimum of 0.611. One-dimensional theory, based on ideal conditions using Bernoulli's theorem, produced more representative trends than Nurick's theorem. Although the predicted figures did not match those produced in the simulations, the directional trends of the exit velocity of the fluid and the coefficient of contraction were similar. When applied to predict cavitation in nozzles with rounded edges, one-dimensional theory predicted cavitation that, in reality, was not present. This is because the basic assumptions include one describing a choked nozzle.

Overall, it is concluded that Nurick's theory best represents flow in nozzles that have inlet curvature, while one-dimensional theory is best applied to predict sharp-orifice flows.

8.2 Fuel parameters affecting cavitation formation

The physical description of the cavitation area, described by the coefficient of contraction, does not depend greatly on the fluid properties. Cavitation occurs in the nozzle for all range of fuel properties and the overall severity of it remains relativity constant for each property difference. This confirms the observation that cavitation is a pressure-driven phenomenon.

A degree of control over the amount of vapour present in the nozzle is possible by altering the viscosity and the fluid surface tension. By decreasing the magnitude of both these properties, it is predicted that the cross-sectional area of the liquid flowing through the nozzle will increase slightly, and the volume of vapour in the nozzle correspondingly will decrease.

Therefore, for the entire spectrum of fuel properties allowed according to the EN590 specification for diesel fuel, cavitation will occur for this geometry under the given conditions of high pressure, low temperature flow.

8.3 Physical parameters affecting cavitation formation

The pressure difference between the fluid upstream and downstream of the nozzle throat is the driving influence for cavitation in nozzles.

The inlet radius can have a significant effect on the severity of cavitation present in a fuel injector nozzle. Increasing the inlet radius reduces the pressure loss across the nozzle inlet, resulting reduced cavitation. The coefficient of contraction is increased and volume of vapour present in the nozzle is significantly reduced. The "hydraulic flip" can be avoided by introducing a fillet to the entrance of a sharp-orifice nozzle.

8.4 Fuel parameters strongly affecting nozzle flow development

It was observed that the fuel density and viscosity affect the rate at which flow develops in the nozzle and at which vapour flows down the nozzle. The fluid surface tension and non-condensable gas fraction have no effect.

It is possible to make a sharp-edged nozzle reach a "steady-state" condition more rapidly through the use of a low density, low viscosity fuel. The nozzle precipitation and advection of cavitation vapour is accelerated.

8.5 Accuracy of measurement devices

Fuel injectors are approximated as constant volume-flow-rate devices. The simulation results reveal the second-order variations that are present.

When the working fluid is a low density fuel, there is an increase in the volume flow rate and a decrease in the mass flow rate of the liquid at the exit during steady-state conditions. Conversely, when a high density fuel is used, the exiting fluid has a decreased volume flow rate and an increased mass flow rate at steady-state conditions. This phenomenon is attributed to the momentum of the fluid, the greater mass of fluid requiring more time to accelerate to a certain velocity than the less dense and smaller mass of fluid.

The fluid momentum effect has important implications for injection events that occur for very short durations. An example of such a situation is a pilot injection, which typically lasts for durations of 0.2 ms. For this short interval, it is possible that the total mass of a lower density fuel injected may be equal to that of a higher density fuel.

Lowering the fuel viscosity greatly accelerates the advection of vapour down length of the nozzle, resulting in a greater volume of fuel being discharged from the nozzle in the first 14.5 μs of simulated injection.

8.6 Parameters affecting cavitation bubble collapse

According to the idealised collapse model, the fuel parameters that have the greatest influence on the collapse of the vapour space present in the nozzle are the liquid viscosity and the volume of contaminant gas present in the liquid. Decreasing the viscosity of the fuel or increasing the volume of non-condensable gas will result in elevated temperatures when collapse occurs. The former will cause a more rapid rate of temperature increase, while the latter results in a more gradual increase in temperature.

The initial temperature and radius of the bubble also greatly affect the maximum temperature experienced during collapse. An average initial temperature elevated above the temperature of the surrounding liquid can result in greatly increased temperatures of collapse, due to an increase in the rate of collapse. The initial radius of the bubble has a significant effect on the maximum collapse temperature due to its effect on the volume of NCG present in the bubble and the momentum of the collapsing bubble. Increasing the initial radius results in greatly increased collapse temperatures.

8.7 Probability of deposition due to thermal cracking

According to the hypothesis presented in this dissertation, two criteria need to be satisfied for thermal cracking to occur in diesel fuel injectors, namely

1. cavitation must occur, and
2. the collapse of the resultant void space must cause temperatures the bubble to exceed approximately 1000°K.

The literature has suggested that cavitation may occur on the upper or lower surface of the nozzle. The fillet radius at and between these positions varies between 63 μm and approximately 0 μm. It has been shown that varying degrees of cavitation occur between these extremes and it is likely that cavitation does occur during the injection process.

Simulations suggest that a localised temperature of up to 500°K may be present in vapour that forms near the wall of the injector nozzle during the injection process. Dependant on the severity of the cavitation and the position of the gas, this local temperature may drop to between 360°K and 400°K. It is apparent that local temperatures in the nozzle due to flow phenomena such as viscous heating are not high enough to promote thermal cracking.

An idealised collapse model predicts that temperatures in excess of 1000°K are easily attained for durations in excess of 0.1ns for fuel with conservative physical properties. Were the fuel to be of extremely low viscosity or to have a large quantity of contaminant gas dissolved in it, this effect would be greatly exacerbated.

It was observed that the temperature of a collapsing void space can easily exceed that required for thermal cracking to occur. The time scale of the collapse is very small, but since the cracking mechanism is chemically simple (it occurs in one step), the decomposition of long-chain hydrocarbons that make up fuel is quite probable. Additionally, the number of injection events per second is large which may result in the production of many smaller, more reactive polymer chains. These could attach to the walls of the injector and promote further deposition; a similar process is described in the literature [18]. It is this mechanism of continuous deposition that results in the deposits seen in Figure 1.1.

9. Recommendations

Based on the conclusions drawn in the previous chapters and the literature, the author suggests further opportunities for worthwhile research around this topic that were outside the scope of research for this project.

9.1 Obtain experimental data

Experimentally determine the extent of deposition and the influence of fuel properties. The effect of the alteration of critical fuel parameters on injector fouling should be determined. It should be ascertained whether any fuel additives that may effectively reduce nozzle deposition exist.

9.2 Refine computation model

It is seen in the literature that the effect of the grid size, turbulence model and discretisation schemes selected can all have an effect on the predicted discharge coefficient of a three-dimensional injector model. An investigation into their effect on two-dimensional axisymmetric models should be conducted, and the a determination of the best selection of parameters should be made.

The current study considers the vapour pressure of diesel to be constant. This has been described previously in the literature to give representative results, although it is not entirely accurate as a substantial temperature variation can exist within the nozzle. It may be worthwhile exploring the inclusion of the effect of temperature dependency on the fluid vapour pressure.

9.3 Investigate injector needle effects

The literature suggests that the reseating of the injector needle may have an effect on cavitation in the injector nozzle. Ideally, the effect of the needle lifting and reseating in the injector on cavitation formation in the nozzle should be determined. This investigation should include

1. the jetting effect that the needle may produce on the flow as the needle is about to reseat, and
2. the possibility of rupture of fluid that remains in the nozzle and sac due to the momentum of the fluid leaving the nozzle.

9.4 Investigate injector geometry

It has been suggested in the literature that nozzle geometry can have a profound effect on cavitation and bubble collapse. An investigation into the control of cavitation through the use of geometrical parameters should be conducted. The investigation should include determining the effect of

1. nozzle length
2. inlet curvature
3. orifice taper

These investigations should determine whether fuel parameters change the degree to geometric parameters affect cavitation. The investigation regarding orifice taper should seek to quantify the degree of nozzle conicity required to prevent the formation of cavitation phenomena.

9.5 Investigate injection parameter control

An investigation should be performed to determine whether the control of the liquid fuel inlet temperature has any significant effect on cavitation in the injector. It is speculated that the injection pressure has a great effect on cavitation, but whether any increase in cavitation is present for conditions above the tested injection pressures currently is unknown. Conclusions will de drawn from performing both computational simulations and experimental work.

9.6 Produce a more comprehensive model

It would be useful to produce a three-dimensional model approximating the effect of the needle and sac on the cavitation in the nozzle. This model could be used to determine effect of needle seating and non-uniform inlet fillet radius on cavitation in the nozzle during the injection event and immediately after the needle has reseated.

9.7 Experimentally determine the contaminant gas fraction

Whilst conducting this research, it was observed that the volume of non-condensable gases is critical in the accurate determination of maximum temperatures present during collapse of a vapour void space. The magnitude of this volume is unknown for local conditions, and should be experimentally determined.

References

[1] W.Boehner, K. Hummel. Common Rail Injection System for Commercial Diesel Vehicles. *SAE paper 970345*, pages 133–141, 1997.

[2] A. Sou, A. Tomiyama, S. Hosokawa, S. Nigorikawa, T. Maeda. Cavitation in a Two-Dimensional Nozzle and Liquid Jet Atomisation. *JSME International*, 49:1253 – 1259, 2006.

[3] M.Kato, H.Kano, K. Date, T. Oya, K. Niizuma. *Flow Analysis in Nozzle Hole in Consideration of Cavitation*, 1997.

[4] Fluent Inc. *FLUENT 6.2 User's Guide*, 11 January 2005.

[5] Robert Bosch GmbH. Internal Paper A 433 190 873. 2002.

[6] Fluent Inc. Fluent 6.1.22 Internal Material Database, Last checked: 21 February 2007.

[7] J.W. Rose, J.R. Cooper, editor. *Technical Data on Fuels*. Scottish Academic Press, 1977.

[8] J.P. Holman. *Heat Transfer, Ninth Edition*. McGraw-Hill, 2002.

[9] D. P. Schmidt, C. J. Rutland, M. L. Corradini. A Fully Compressible, Two-Dimensional, Model of Small, High Speed, Cavitating Nozzles. *Atomization and Sprays*, 9, 1999.

[10] H. Roth, M. Gavaises, C. Arcoumanis. Cavitation Initiation, Its Development and Link with Flow Turbulence in Diesel Injector Nozzles. *SAE paper 2002-01-0214*, 2002.

[11] J. Benajes, J. V. Pastor, R. Payri, A. H. Plazas. Analysis of the Influence of Diesel Nozzle Geometry in the Injection Rate Characteristic. *Journal of Fluids Engineering*, 126(63):63–71, January 2004.

[12] A. Marchese. *Fluid Mixing: Rayleigh-Taylor Mixing Rate and Diesel Fuel Injection Spray*. PhD thesis, December 2002.

[13] A. Leedham, R. Caprotti, O.Graupner, T. Klaua. Impact of Fuel Additives on Diesel Injector Deposits. *SAE paper 2004-01-2935*, 2004.

[14] F. Payri, V. Bermúdez, R. Payri, F.J. Salvador. The influence of cavitation on the internal flow and the spray characteristics in diesel injection nozzles. *Fuel*, 83:419–431, 2004.

[15] R. Payri, F.J. Salvador, J. Gimeno, L.D. Zapata. Diesel nozzle geometry influence on spray liquid-phase fuel. *Fuel*, 10, 2007.

[16] M. Gavaises, A. Andriotis. Cavitation Inside Multi-hole Injectors for Large Diesel Engines and Its Effect on the Near-nozzle Spray Structure. *SAE paper 2006-01-1114*, 2006.

[17] J. M. Desantes, R. Payri, F. J. Salvador, J. Gimeno. Measurements of Spray Momentum for the Study of Cavitation in Diesel Injection Nozzles. *SAE paper 2003-01-0703*, 2003.

[18] G. Lepperhoff, M. Houben. Mechanisms of Deposit Formation in Internal Combustion Engines and Heat Exchangers. *SAE paper 931032*, 1993.

[19] R. Williams. Development of a Nozzle Fouling Test for Additive Rating in Heavy Duty DI Diesel Engines. *SAE paper 2002-01-2721*, 2002.

[20] D. P. Schmidt, Tzay-Fa Su, Kayhan H. Goney, P. V. Farrell, M. L. Corradini. Detection of Cavitation in Fuel Injector Nozzles. *Transport Phenomena in Combustion*, 1996.

[21] D. MacDonald. The Characterisation of High Pressure Injection. Technical report, INOV8 Technologies plc, 2005.

[22] L. C. Ganippa, G. Bark, S. Andersson, J. Chomiak. Comparison of Cavitation Phenomena in Transparent Scaled-up Single-Hole Diesel Nozzles. In *CAV 2001: Fourth International Symposium on Cavitation*. California Institute of Technology, June 2001.

[23] S. Collicott, H. Li. True-scale True-pressure Internal Flow Visualization for Diesel Injectors. *SAE paper 2006-01-0890*, 2006.

[24] A. Singhal, M. Athavale, H. Li, Y. Jiang. Mathematical Basis and Validation of the Full Cavitation Model. *Journal of Fluids Engineering*, 124:617 – 624, September 2002.

[25] C. E. Brennen. *Cavitation and Bubble Dynamics*. Oxford University Press, 1995.

[26] D. P. Schmidt, C. J. Rutland, M. L. Corradini, P. Roosen, O. Genge. Cavitation in Two-Dimensional Asymmetric Nozzles. *SAE paper 1999-01-0518*, 1999.

[27] U. Iben, M. Voß, W. Bauer. *Simulation of Cavitating Flow in Automotive Injection Systems*. Robert Bosch GmbH, ANSYS Germany GmbH, Winter 2005.

[28] Fluent Inc. *Cavitation in a Diesel Fuel Injector*. Fluent Inc., 2003.

[29] Fluent Inc. *Cavitating Diesel Fuel Injector*. Fluent Inc., 2005.

[30] Yong Yi. Investigating Engine Systems with CFD Tools. `www.erc.wisc.edu/symposiums/2005_Symposium/June%208%20AM/Yi_Fluent.pdf`, Last visited: 07 July 2007. Fluent Inc.

[31] M. Kubo, T. Araki, S. Kimura. Internal flow analysis of nozzles for DI diesel engines using a cavitation model. *JSAE*, 24:255–261, 2003.

[32] N. Anantharamaiah, H. Tafreshi, B. Pourdeyhimi. A study on flow through hydroentangling nozzles and their degradation. *Chemical Engineering Science*, 61:4582–4594, 2005.

[33] E. Giannadakis, D. Papoulias, M. Gavaises, C. Arcoumanis, C. Soteriou, W. Tang. Evaluation of the Predictive Capability of Diesel Nozzle Cavitation Models. *SAE paper 2007-01-0245*, 2007.

[34] R. Payri, X. Margot, F. J. Salvador. A Numerical Study of the Influence of Diesel Nozzle Geometry on the Inner Cavitating Flow. *SAE paper 2002-01-0215*, 2002.

[35] R. Masuda, T. Fuyuto, M. Nagaoka, E. von Berg, R. Tatschl. Validation of Diesel Fuel Spray and Mixture Formation from Nozzle Internal Flow Calculation. *SAE paper 2005-01-2098*, 2005.

[36] A. E. Catania, A. Ferrari, M. Manno, E. Spessa. Thermal Effect Simulation in High-Pressure Injection System Transient Flows. *SAE paper 2004-01-0532*, 2004.

[37] M. Blessing, G. Knig, C. Krger, U. Michels, V. Schwarz. Analysis of Flow and Cavitation Phenomena in Diesel Injection Nozzles and its Effects on Spray and Mixture Formation. *SAE paper 2003-01-1358*, 2003.

[38] S. Zwick. *The Growth and Collapse of Cavitation Bubbles*. PhD thesis, California Institute of Technology, 1955.

[39] F. Lugli, F. Zerbetto. An introduction to bubble dynamics.

[40] H. Alehossein, Z. Qin. Numerical analysis of Rayleigh-Plesset equation for cavitating water jets. *International Journal for Numerical Methods in Engineering*, 2007.

[41] Wang Xia. Numerical simulation of violent bubble motion. *Physics of Fluids*, 16(5):1610–1619, 2004.

[42] S. Popinet, S. Zaleski. Bubble collapse near a solid boundary: A numerical study of the influence of viscosity. *Journal of Fluid Mechanics*, 464:137–163, August 2002.

[43] D. Obreschkow, P. Kobel, N. Dorsaz, A. de Bosset, C. Nicollier, M. Farhat. Cavitation Bubble Dynamics inside Liquid Drops in Microgravity. *Physical Review Letters*, 2006.

[44] A. Szeri, B. Storey, A. Pearson, JJ. Blake. Heat and mass transfer during the violent collapse of nonspherical bubbles. *Physics of Fluids*, 15(9):2576–2586, 2003.

[45] V. Bogoyavlenskiy. Differential criterion of a bubble collapse in viscous liquids. *Physical Review E*, 60(1):504–508, July 1999.

[46] J. Jimenez-Fernandez, A. Crespo. Bubble oscillation and inertial cavitation in viscoelastic fluids. *Ultrasonics*, (43):643–651, 2005.

[47] B. Storey, H. Lin, A. Szeri. Physically Realistic Models of Catastrophic Bubble Collapses. In Roger E.A. Arndt Christopher Earls Brennen, Steven L. Ceccio, editor, *CAV2001 Fourth International Symposium on Cavitation*. California Institute of Technology, 2001.

[48] A. Aganin, M. Il'gamov. Numerical simulation of Gas Dynamics in a Bubble during its Collapse with the Formation of Shock Waves. *Journal of Applied Mechanics and Technical Physics*, 40(2):276–284, 1999.

[49] W. McNamara, Y. Didenko, K. Suslick. Sonoluminescence temperatures during multi-bubble cavitation. *Nature*, 401:772–776, 1999.

[50] T. Lu, R. Samulyak, J. Glimm. Direct Numerical Simulation of Bubbly Flows and Application to Cavitation Mitigation. *Journal of Fluids Engineering*, 129:595–604, May 2007.

[51] E Brujan. Collapse of cavitation bubbles in blood. *Europhysics letters*, 50(2):175–181, 2000.

[52] W. H. Nurick. Orifice Cavitation and Its Effects on Spray Mixing. *Journal of Fluids Engineering*, 98:681–687, December 1976.

[53] H K Versteeg, W Malalasekera. *An introduction to Computational Fluid Dynamics: The finite volume method*. Pearson Education Limited, 1995.

[54] A. Royne, C. J. Dey. Effect of nozzle geometry on pressure drop and heat transfer in submerged jet arrays. *International Journal of Heat and Mass Transfer*, 49:Pages 800–804, February 2006.

[55] S. Murajami. Overview of turbulence models applied in CWE-1997. *Journal of wind engineering and industrial aerodynamics*, (74-76):1–24, 1998.

[56] W. Rodi. Comparison of LES and RANS calculations of the flow around bluff bodies. *Journal of wind engineering and industrial aerodynamics*, (69-71):55–75, 1997.

[57] A. Boehman, M. Alam, J. Song, R. Acharya, J. Szybist, V. Zello. Fuel Formulation Effects on Diesel Fuel Injection, Combustion, Emissions and Emissions Control. In *DOE 2003 Diesel Engine Emissions Reduction Conference*. The Energy Institute, Pennsylvania State University; ConocoPhillips, August 2003.

[58] R. Hutcheson, D. G. Snelgrove. *Gasoline and Diesel Fuel Technology*. The Oxford Princeton Programme, June 2006.

[59] Fluent Inc. Administrator. Cavitation Model. `http://university.fluent.com/forum/viewtopic.php?t=728&view=next&sid=23b4069daa696dbce61dc42bc0d18c1c`, Last visited: 30 October 2006.

[60] Fluent Inc. Tips for successfully modeling cavitating flows in rotating equipment. `http://www.fluent.com/support/solution.htm?id=971`, Last visited: 30 October 2006.

APPENDIX

A. The Cavitation Phenomenon

The following chapter describes, in detail, the causes and factors involved in the cavitation effect. Physical and experimental observations, as well as the mathematics used to describe the cause for, and factors involved in, bubble formation, are discussed. This chapter consists mostly of a summary of the text by C. Brennen [25], and will not be referenced further in this chapter. Summary of other text is, where necessary, distinguished by reference.

Causes of phase change

There are two main factors that can initiate a phase change in a fluid. These are a sudden decrease in pressure or an increase in temperature. In both cases, phase change may occur locally and not affect the whole fluid environment as only regions in the fluid may reach its tensile strength. These phenomena are described below:

1. Cavitation is the process of rupturing a liquid by a decrease in pressure at a roughly constant liquid temperature. A liquid at constant temperature could be subjected to an absolute pressure lower than its saturation vapour pressure. Fluid rupture occurs when the pressure difference between the absolute- and vapour- pressures is greater than the tensile strength of the fluid at that specific temperature.
2. Boiling is the process of rupturing a liquid by an increase in temperature at a roughly constant pressure. A liquid at constant pressure can be subjected to a temperature exceeding its saturation temperature.

Nucleation

Nucleation describes the mechanism involved with the inception of cavitation. Two types of nucleation exist, namely homogeneous and heterogeneous nucleation.

Heterogeneous nucleation describes the case where the point of weakness, and therefore rupture, of a fluid occurs between a solid surface and the liquid. The described solid may be the surface that contains the liquid, or particles that are suspended in the liquid. It is this nucleation mechanism best describes that expected in nozzle flows.

Homogeneous nucleation occurs when thermal motions within the liquid form microscopic voids. These voids act as points of weakness for the fluid, and can rupture and grow into macroscopic bubbles. Heterogeneous nucleation occurs at a boundary interface between the liquid and a solid wall or contaminant particles suspended within the fluid.

In fuel, dissolved gases and microscopic particles that pass through fuel-filters will act as nucleation sites [21]. Microscopic surface geometry has a great effect on nucleation, and surface imperfections can act as nucleation sites. Due to the hydrodynamic flow in a system, some regions in the domain will have the optimum geometry to promote bubble growth. As the pressure in the flow regime decreases below the vapour pressure, more areas become capable of generating and releasing bubbles into the flow.

Residence time effects also play a role in the formation of cavitation bubbles. For the growth of a bubble nucleus to a reasonable size, it is required that the nucleus experiences the low pressure for a reasonable length of time. Should the microscopic bubble be swept into a region of higher pressure, it is conceivable that it may decrease in size and play no further role in cavitation inception.

The effect of contaminant gas

A further cause of nucleation is the presence of contaminant gases that reside within the liquid. These microscopic bubbles exist in all liquids, as deaeration techniques are not able to remove all gas impurities. The contaminant gas acts as a point of weakness in the fluid, and increases the likelihood of localised fluid rupture.

In an ideal flow, the inception of cavitation occurs when the local pressure reaches the vapour pressure of the liquid. However, in a well degassed liquid, it is possible that cavitation may only occur at pressures below the vapour pressure. Conversely, in a liquid containing a large quantity of contaminant gas, the pressure at which a gas bubble grows could be very much higher than the vapour pressure.

The viscous effects on the inception of cavitation

In a viscous flow system, the minimum pressure experienced in the flow domain will depend on the Reynolds number, which means that the cavitation pressure is also dependant on the Reynolds number. Most flows are both turbulent and unsteady, so both free- and forced- shedding of vortices occur.

The pressure at the centre of a vortex may reach values well below the mean pressure of the flow. The implication of this is that cavitation may begin at a transient vortex centre as the pressure there drops below the vapour pressure.

Conclusion

In summary, the reasons for cavitation inception pressure to be different from vapour pressure are as follows:

1. The existence of a tensile strength (pressure difference) can cause a reduction in cavitation inception pressure
2. Residence time effects can cause a reduction in cavitation inception pressure
3. The presence of a contaminant gas can cause an increase in cavitation inception pressure
4. Steady viscous effects due to the dependence of vapour pressure on Reynolds number can cause the cavitation inception pressure to be a function of the Reynolds number

5. Turbulence effects can cause an increase in cavitation inception pressure

During the conduction of experiments, is is important to maintain the following parameters in order to have complete control over the cavitation and vapour development in the system:

1. The cavitation number
2. The Reynolds number
3. The bulk liquid temperature
4. The liquid quality, including the number and nature of the free-stream nuclei, the amount of dissolved gas and the free-stream turbulence
5. The quality of the solid, bounding surfaces, including roughness, and the porosity or pit population

A.1 Rayleigh-Plesset equation for spherical bubbles

The generalised Rayleigh-Plesset equation for bubble dynamics is described as follows:

$$-\rho_L R\ddot{R} = \left(\underbrace{\frac{3}{2}\rho_L \dot{R}^2}_{P_{vel}} + \underbrace{p_\infty}_{P_{ext}} + \underbrace{\frac{2S}{R}}_{P_{sur}}\right) - \left(\underbrace{p_V + p_{Go}\left(\frac{R_o}{R}\right)^{3k}}_{P_{gas}} - \underbrace{4\mu_L\frac{\dot{R}}{R}}_{P_{vis}}\right) \tag{A.1}$$

where P_{vel} indicates pressure terms due to the bubble wall velocity
P_{gas} indicates pressure terms due to the gas inside the bubble
P_{ext} indicates external pressure terms
P_{vis} indicates pressure terms due to viscosity
P_{sur} indicates pressure terms due to surface tension

The above equation is derived from the Navier-Stokes equation in spherical coordinates. It takes the conservation of mass into account by relating the volume rate of production of vapour to the rate of increase in the size of the bubble. A dynamic boundary condition relating the pressure inside the bubble to the bubble surface tension is also considered. Equation A.1 has been described in such a manner as to emphasise pressure terms that accelerate (P_{vel}, P_{ext}, P_{sur}) or decelerate (P_{vis}, P_{gas}) the bubble wall [39].

Several assumptions and simplifications are made in the formation of Equation A.1. Firstly, it is assumed that the far-field temperature is constant. The far-field pressure $p_\infty(t)$ is a known input, as it controls the expansion and collapse of the bubble. Compressibility effects are negated by assuming the density of the liquid ρ_L to be constant. The dynamic viscosity is also assumed uniform and constant. The bubble is considered to be homogeneous in nature, so the temperature and pressure $p_B(t)$ inside the bubble are uniform.

Considerations for the contents of the bubble are also made. The presence of contaminant gas is accounted for in the second term on the left hand side of Equation A.1. It is assumed that no mass transfer of the contaminant gas from the bubble to the surrounding fluid, and that thermal effects can be ignored. This implies that bubble formation is due to pressure and viscous effects, rather than due to temperature effects.

The gas in the bubble is also considered to be polytropic in nature; $k = 1$ describes an isothermal bubble, while $k = \gamma$ describes adiabatic behaviour.

It is interesting to note that the only viscous contribution to the Rayleigh-Plesset equation is due to the boundary condition at the surface of the bubble.

A.2 Bubble growth

Bubble growth can be due to mass diffusion, thermal, non-equilibrium, convective and surface-roughening effects.

Diffusion of gases between the liquid and the bubble are a primary cause of change in mass of the bubble. Diffusion of vapour and contaminant gases may occur, although the diffusion of contaminant gases occurs only in minute quantities, which may be significant over very small time intervals. This diffusion is important, as each microbubble acts as a nucleation site for cavitation inception. Another mass diffusion effect is the change in ambient pressure. This can lead to bubble growth even in a non-saturated liquid.

An "inertially controlled" bubble is one that experiences a change in form in the absence of any significant thermal effects. Thermal effects become significant over longer time intervals, as opposed to the mass diffusion effects which are important at the inception of cavitation. This is because in an inertially controlled bubble, the thermal boundary layer thickness is assumed to be very small. Over long time intervals, the thermal terms in the Rayleigh-Plesset equation exceed those of the inertial, gaseous, viscous and surface tension terms.

The rate of bubble growth is affected heavily by the thermodynamic properties of the fluid. The rate of bubble growth is influenced heavily by the thermodynamic properties of the fluid; therefore, as the temperature of the working fluid changes, one can expect the rate at which cavitation occurs to change. This is because a change in temperature affects not only the physical properties of the fluid, but also the pressure at which cavitation inception occurs.

Non-equilibrium effects exist when the liquid at the bubble interface is not in thermal equilibrium with the vapour contained within the bubble. This effect is significant when there is a large discontinuity at the interface. Such may occur near the end of a bubble collapse.

Convective effects describe the heat transfer due to the relative motion between the bubble and the surrounding liquid. If the pressure difference between the vapour pressure of the fluid and the free-stream is significantly greater than the multiple of the volume fraction of the liquid and the liquid density, then the convective heat transfer effects will delay the onset of thermal growth.

Surface roughening effects describe the heat transfer at the bubble surface due to the formation of an instability at the surface. This occurs when the surface becomes rough and turbulent, which increases the surface area of the bubble and increases heat transfer across the surface interface.

A.3 Bubble collapse

Cavitation bubble collapse is a significant topic of discussion. The collapse of a vapour-filled bubble in a fluid is often violent and causes much damage to the surrounding material. High velocities, pressures and temperatures are often present in this event.

Collapsing bubbles do not remain spherical. However, spherical analysis is often useful to gauge the maximum possible values of fluid properties such as pressure and temperature that could be attained in such an event. The cause of the actual event experiencing lower temperatures and pressures than the spherical bubble case is that the point of the collapse is dispersed as opposed to being focused. Factors such as the diffusion of gas from the liquid into the bubble or vice versa, as well as liquid compressibility, reduce the magnitudes of properties experienced during bubble collapse. Compressibility itself has a tendency greatly to reduce the velocity of collapse.

The difference between idealised calculations and a real condition is described in the following example: According to the ideal spherical bubble calculations, the collapse of a bubble of size 100 times that of its nucleation size and with a nucleation partial pressure of 1 bar would result in a maximum collapse pressure of $1\text{x}10^{10}$ bar and a maximum temperature $4\text{x}10^{4}$ times greater than the ambient temperature. Clearly, this would not occur in a real, physical case.

Another factor that complicates collapse is the presence of non-condensable gas or thermal effects. This is because the pressure within the bubble can no longer be treated as constant. While there exists some gas that will decelerate the collapse of a bubble, fluid compressibility does not have a major role in the bubble dynamics. It does however have a significant effect on the formation of shock waves formed when the bubble rebounds after collapse. This is because of the propagation of a pressure pulse directed away from the bubble after it has reached its minimum size. Lastly, it has also been noted that surface tension and viscosity do not have a major effect in bubble collapse.

A.3.1 Thermal effects

It is important to note that the collapsing bubbles can experience thermal effects early in the collapse in a similar manner to that experienced in bubble growth. Even though these effects may be negligible for most of the phase of collapse, they do have a significant effect during the final stage of collapse, At this point, the contents of the bubbles become highly compressed due to the inertia of the surrounding fluid. Both the pressures and temperatures predicted during a spherical bubble collapse are very high.

The non-condensable gas in the bubbles is assumed to behave adiabatically because of the very short time that elapses during collapse. It has been shown that heat transfer between the gas and the liquid is important because of the very small distances and large temperature gradients involved.

In an experiment, the details of which are unknown, it has been predicted that a bubble centre of a spherical bubbles may reach temperatures as high as 8800°K during the phase of collapse. Other predictions describe temperatures of 6700°K and pressures of 848bar. The interface temperature between the bubble and surrounding fluid has been estimated to be at 3400°K for the latter case.

Other effects of importance include the inter-diffusion of gas and vapour within the bubble, which may cause a build-up of non-condensable gas at the interface. This means that the vapour must diffuse through the non-condensable gas in order to condense on the interface.

A.3.2 Chemical effects

Energy transfer present during cavitation bubble collapse breaks down long-chain hydrocarbon molocules into short-chain hydrocarbons, such as methane, and hydrogen. This assists in reducing combustion time, but also results in decreased combustion temperatures and reduced nitrous oxide production. Hydroxyl radicals, responsible for the decomposition of carbon double-bonds, are also released. [21]

These effects are most readily observed when cavitation is induced inside fuel droplets. This can be achieved by forcing the droplets to exit the nozzle orifice at supersonic speeds. [21]

A.3.3 Bubble shape

There are three main stages to bubble collapse in a stationary fluid:

1. The initial inward acceleration of the bubble due to the difference between the bubble surrounding fluid ($P_\infty > P_V$).
2. A stage of greatly increasing inwards acceleration, which occurs prior to the period of significant compression within the bubble, due to external pressures and surface tension effects
3. The rebound stage, where the acceleration is very large in the outwards direction

All vapour bubbles that collapse to a size several orders of magnitude less than their maximum size produce a cloud of smaller bubbles upon collapse. This phenomenon occurs over an extremely small time-scale. Furthermore, it is important to note that fluid flow effects will cause the bubbles to deform and will significantly alter the effect experienced during bubble collapse.

A.3.4 Cavitation damage

It is widely recognised that cavitation bubble collapse near a solid surface is a major cause of damage to solid materials. During the collapse stage, both highly localised, large amplitude shock waves and micro-jets are generated within the bubble.

When this collapse occurs near a surface, very highly localised and transient stresses are generated within the material. Repetition of this loading causes material fatigue, leading to surface failure. The result of cavitation is the surface material flaking off the wall. Soft materials have a tendency to form a pitted surface when cavitation wear takes place.

APPENDIX: Axisymmetric Nozzle

B. Initial Calculations

B.1 Treatment of fluid phases

Consideration of fluid compressibility is paramount for flow involving high velocities. However, information outlining the sonic velocity for very high-pressure diesel fuel is scarce.

B.1.1 Liquid

The speed of sound for fluid in a liquid phase can be determined by its bulk modulus and density:

$$c_{\text{fluid}} = \sqrt{\frac{K}{\rho}} \tag{B.1}$$

The bulk modulus of diesel liquid increases considerably as the liquid pressure increases. A linear increase in bulk modulus from 1400 MPa to 1750MPa is observed as pressure increases from 0 MPa to 30 MPa [57]. At the outlet, a bulk modulus of approximately 1475 MPa is expected, which equates to a sonic velocity of 1333 m/s for diesel assuming a constant specific gravity of 0.830.

Additionally, diesel fluid at 60°C compressed to 2 MPa and 10 MPa have speed of sound values of approximately 1210 m/s and 1250 m/s respectively [11]. The pressures involved in nozzle flow are expected to be around 1500 bar at the inlet and 50 bar at the outlet, with an average of roughly 750 bar. Using linear interpolation estimates of the sonic velocity at these pressures are 1950 m/s, 1490 m/s and 1575 m/s. These values may be underestimates, since the trend is that at higher pressures the difference between the value of the sonic velocity increased as the pressure increased at a constant rate [11]. They do however correlate well with that determined by Equation B.1.

Using Bernoulli's equation for inviscid, incompressible, irrotational, laminar flow (Equation B.2), an approximation of the expected outlet velocity can be determined. This can serve as a worst case determination for the compressibility effects of the fluid, since the expected sonic velocity is lowest for this pressure.

$$\frac{p}{\rho} + \frac{v^2}{2} + gz = \text{constant} \tag{B.2}$$

Assuming stagnation conditions at the inlet, the outlet velocity was approximated to be 591m/s, which equates to a Mach number at the outlet of roughly 0.396 at 60°C using the interpolated empirical data. Since the Mach number does not look to exceed 0.4 for the fluid, compressibility effects will be neglected for the liquid phase. The region of separation at the nozzle entrance, where the velocity is expected to be greatest, will be at a reasonably high pressure, resulting in a lower Mach number than the outlet.

A first approximation simulation using the incompressible liquid assumption revealed that the maximum exit velocity was closer to 510 m/s, equating to a Mach number of 0.342 at 50 bar. A higher velocity of 550 m/s is experienced by the liquid at the entrance to the *vena contracta*, but the pressure in this region is nearly three times as great as the exit pressure, resulting in a lower Mach number.

B.1.2 Gas

An approximation for the speed of sound in diesel vapour is made by treating the vapour as an ideal gas:

$$c_{\text{gas}} = \sqrt{\frac{\gamma R T}{M}} \tag{B.3}$$

where γ is the adiabatic index
R is the universal gas constant, 8.3145 $\text{J.K}^{-1}.\text{mol}^{-1}$
M is the molar mass of the gas, equal to 221.16 for $C_{16}H_{29}$ fuel

The value of γ for diesel vapour of the specified properties is uncertain, but a value of 1.04117 is used, as seen in the literature [12]. Therefore, the approximate value of the speed of sound in diesel vapour is 114.2 m/s at 60°C. It is quite clear that for an accurate solution, vapour density should be taken into account.

In order for the gas to be modelled correctly, the correct equation of state, taking into account both pressure and temperature effects, needs to be chosen. An ideal gas model will be realistic at high temperatures and low pressures, both of which may be present in this situation.

Literature suggests that a gamma gas law, which links both pressure to the density and temperature of the fluid, may be used as an alternative to an ideal gas law [12]:

$$P = e^{\frac{S_0(\gamma-1)}{R}} \rho^{\gamma} \tag{B.4a}$$

$$S_0 = \frac{log\left(\eta_v\right) R_v}{\gamma - 1} \tag{B.4b}$$

$$R_v = \frac{\eta_v {\rho_v}^{\gamma-1}}{T} \tag{B.4c}$$

$$\eta_v = \frac{p_v}{{\rho_v}^{\gamma}} \tag{B.4d}$$

B.2 Boundary conditions: Turbulence properties

When using a turbulence model, it is necessary to specify the turbulence conditions experienced at the inlet and outlet boundaries. For internal flow, it is convenient to express these conditions in terms of the turbulence intensity and turbulence length scale.

The turbulence intensity is the ratio of the root-mean-square of the velocity fluctuations and the mean flow velocity. The turbulence intensity at the inlet is dependant on the flow conditions upstream of the flow. A low turbulence intensity is used for undisturbed and under-developed flow. The turbulence at the centre of a fully-developed pipe is given by the following empirical formula: [4]

$$I = 0.16(Re_{D_H})^{-\frac{1}{8}} \tag{B.5}$$

The turbulence length scale is a quantity that is related to the large eddies that are present in turbulent flow. In fully developed flow, the size of an eddy is restricted by the size of the pipe, and is approximated by Equation B.6a. Equation B.6b describes the turbulence length scale as a function of the boundary layer thickness for flat-plates. It is particularly useful for wall-bounded flows where the inlet involves a turbulent boundary layer. [4]

$$\ell = 0.07L \tag{B.6a}$$

$$\ell = 0.4\delta_{99} = 0.4\left(5L\sqrt{Re}\right) \tag{B.6b}$$

where δ_{99} is the boundary layer thickness.

B.3 Fluid vapour pressure

In Section 4.1.4, the effect of turbulence on the vapour pressure is discussed. Equation 4.11a describes this effect. In order to gauge the effect of the turbulent pressure rise, the local turbulence kinetic energy, given in Equation B.7, must be determined.

$$k = \frac{3}{2}\left(u_{ave}I\right)^2 \tag{B.7}$$

It was determined that the turbulence kinetic energy at the entrance to the nozzle is approximately 82.4 m^2/s^2. Equation 4.11a was then used to determine the actual vapour pressure of roughly 14300Pa at the nozzle throat for a vaporisation pressure of 1930 Pa. It is therefore observed that, at the working temperature of the fuel, the turbulent effects on the vapour pressure of the system far more significant than the STP vaporisation pressure of the fluid.

B.4 Heat transfer: Brinkman number

Viscous heating describes the creation of thermal energy due to viscous shear in the flow. In order to determine whether the effect of viscous heating is significant in the context of the axisymmetric geometry, it is necessary to determine the Brinkman number [4]:

$$Br = \frac{\mu U_e^2}{k \triangle T} \tag{B.8}$$

where $\triangle T$ is the temperature difference in the system

For an average exit velocity of 350 m/s (based on the mass flow rate of a non-cavitating nozzle) and an expected temperature difference of 80 °C [21] between the entrance and exit of the nozzle, $Br \approx 37.5$. This implies that the viscous dissipation terms are very significant in the transfer of heat in the nozzle.

C. Computational Geometry

This chapter explains how the geometry of the fuel injector was modelled in FLUENT®.

C.1 Fuel injector

Figure C.1 describes the actual geometry of the fuel injector that was used as a base for the simulated model. The specified injector is that used on a BMW 320d E46. This injector has a measured volume flow rate of between 431 cm^3/30s and 449 cm^3/30s at 100 bar. The maximum injector pressure that can be sustained is 1800 bar.

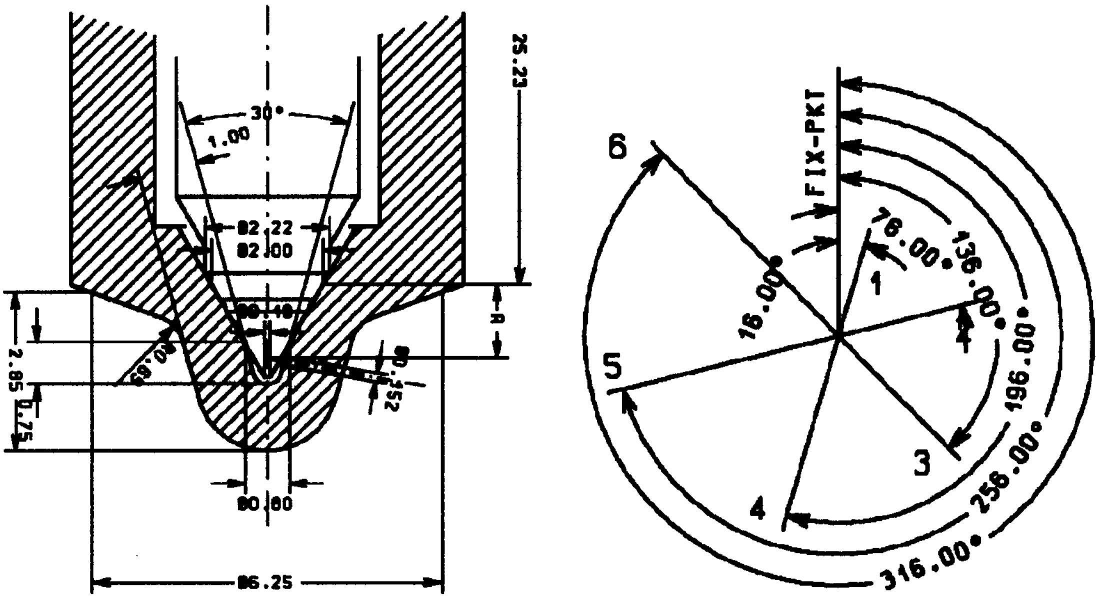

(a) Transverse section

(b) Nozzle orientation

Figure C.1: Diesel fuel injector geometry [5]

C.2 Computational domain

The injector was modelled by two-dimensional, axisymmetric geometry, with the dimensions similar to those when the nozzle it cut transversely through the diameter of a spray hole. The centreline of the nozzle was taken as the axis of symmetry. The nozzle radius and length were set at 7.5 μm and 1 mm respectively. No information regarding nozzle taper was available.

The inlet boundary was set 0.4 mm away from the centreline of the nozzle entrance as to allow stagnation conditions to exist at the boundary. The nozzle inlet corner was created as a sharp edge, in order to promote cavitation in this region. Where stated, a fillet radius on the inlet corner was produced. Figure C.2 shows the boundary conditions subscribed to the general geometry of the problem.

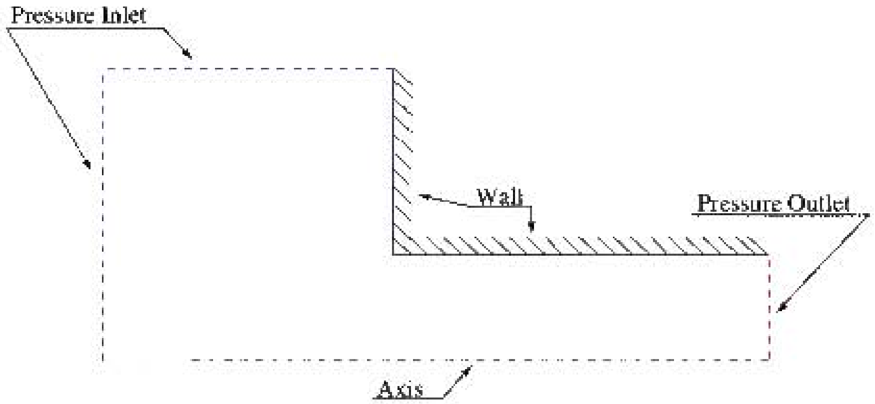

Figure C.2: Boundary conditions

C.2.1 Geometry creation

The entire grid was discretised using quadrilateral elements of rectangular shape. This done so that most of the flow aligned well with the grid, reducing numerical diffusion. A fine mesh was constructed in the inlet region to accurately capture separation, cavitation and turbulent effects near the nozzle entrance. The mesh was made gradually coarser as it extends toward the nozzle exit, and upwind to the inlet.

Due to the presence of separation and recirculating, low-velocity flow at the nozzle entrance, a two-layer model incorporating enhanced wall functions needed to be employed. This method clearly was not employed by Singhal et al. [24], who employed grids consisting of only 2800 cells. However, it was felt that since turbulent vortices and recirculating flow would be present near the nozzle entrance, it would be necessary to accurately capture these effects. The turbulence has a great effect on the cavitation inception pressure, and it was felt that a significant change in the turbulence formation may be possible through the alteration of fuel parameters. Furthermore, an accurate determination of the coefficient of contraction was deemed necessary. This required a fine grid to reduce the inaccuracy in representation of the gaseous and liquid regions of the domain. One disadvantage to this approach is that the effect of surface roughness can not be empirically accounted for.

The requirements for the Enhanced Wall Treatment (EWT) of near wall flow necessitated the grid at the boundary layer needed to be very fine. It was required cells adjacent to the wall had cell centres sufficiently close so that the wall y^+ value was as close to unity as possible. This was not always possible, since as the pressure profile and velocity changes in the nozzle, the y^+ value also changes. Therefore, the grid was constructed such that as the velocity profile in the nozzle changed, the y^+ value was kept near or below 5 for the cells next to the nozzle wall. The grid for the square inlet nozzle is shown in Figure C.3. The grid consisted of a 384 by 32 cell mesh totalling 12352 cells in the nozzle, while 19520 cells were used in the high-pressure region upwind of the nozzle throat. In total, a mesh consisting of 31872 cells was used.

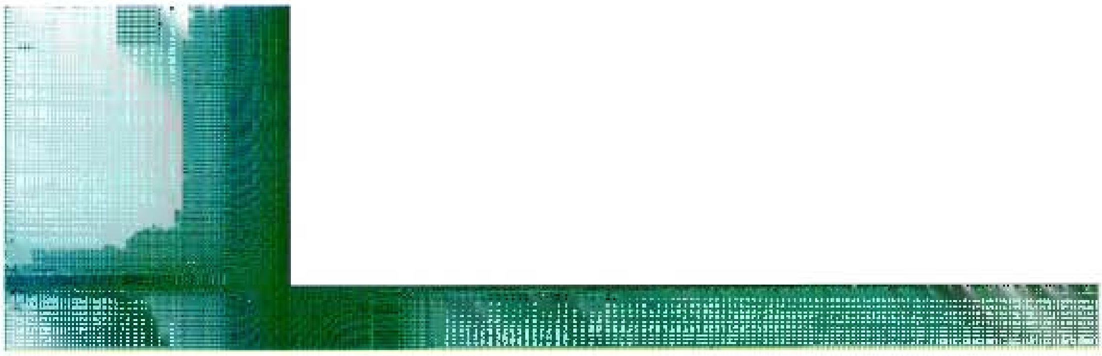

(a) Whole grid

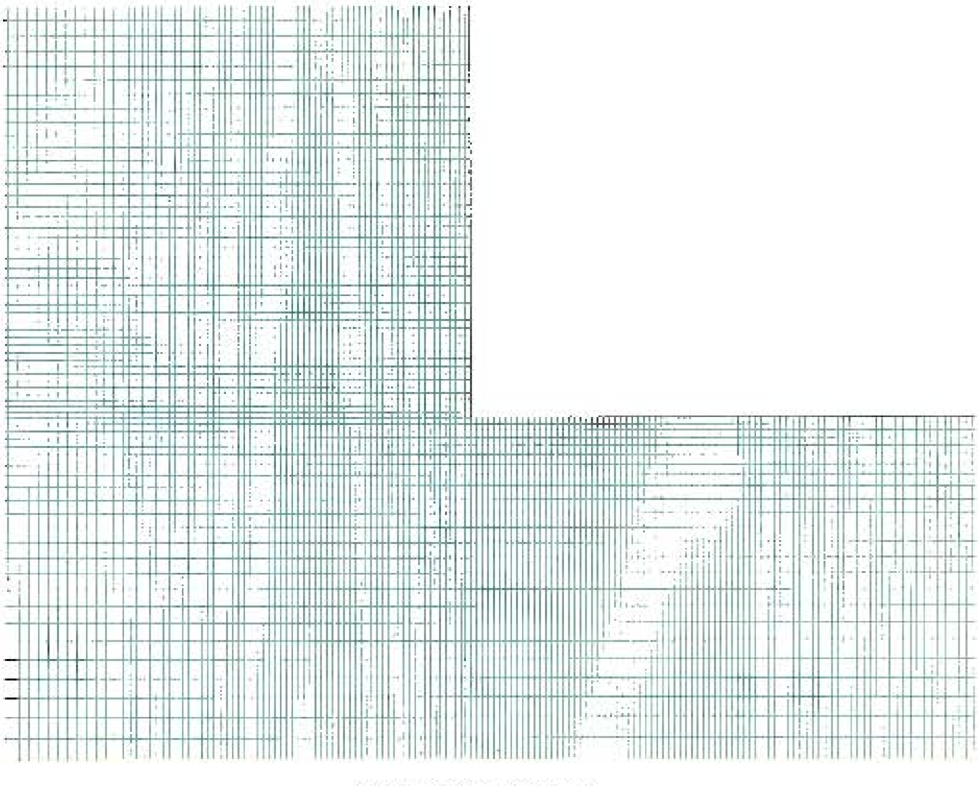

(b) Detail of nozzle throat

Figure C.3: Computational grid for square-inlet simulations

Only the mesh containing a rounded inlet contained distorted elements. The mesh was kept structured, as this allowed for the mesh near the wall in the boundary layer to be tightly controlled. The flow in the region of distorted mesh is uniform and does not undergo large changes in direction or have large property gradients. Numerical inaccuracy in this region was considered to be minimised and necessary to enforce good mesh quality in the boundary layer near the nozzle entrance. In retrospect, a semi-unstructured grid could have been employed to minimise mesh distortion of the grid near the axis. An example of a grid used for a simulation of a nozzle with a rounded inlet is depicted in Figure C.4.

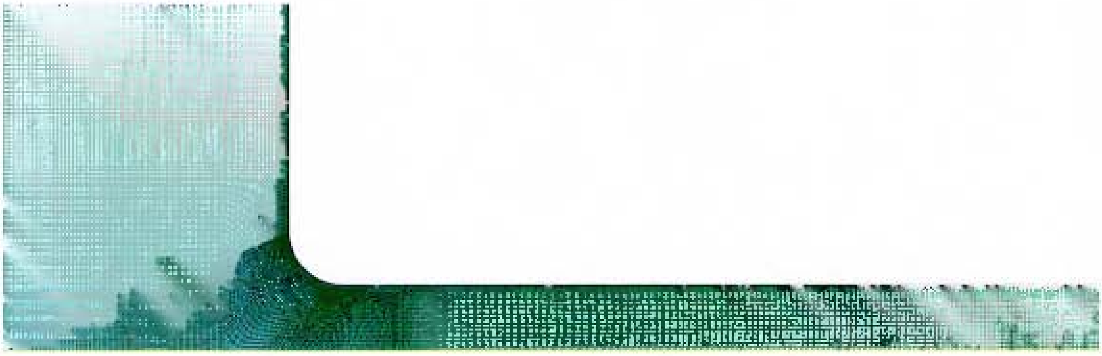

(a) Whole grid

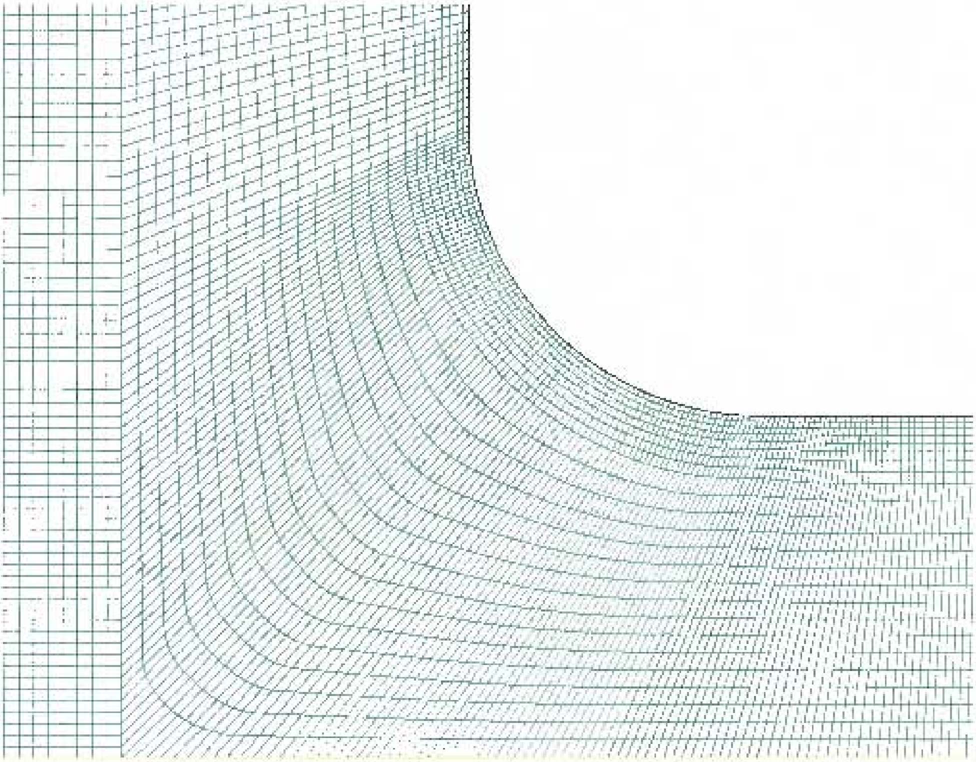

(b) Detail of nozzle throat

Figure C.4: Computational grid for rounded-inlet simulations

D. Computational Settings

D.1 Standard fluid properties and specifications

The following Tables D.1 and D.2 describe the properties of liquid and gaseous diesel fuel (gas-oil) that were used as the working medium in simulations.

Property	Units	Value
Density @ 15°C	$kg.m^{-3}$	830
Viscosity @ 40°C	$kg.m^{-1}.s^{-1}$	0.00332
Specific heat capacity (C_p)	$J.kg^{-1}.K^{-1}$	2050
Droplet surface tension	$N.m^{-1}$	0.025
Vapour pressure @ 360K	Pa	1930

Table D.1: Liquid diesel fuel properties [6, 7]

Property	Units	Value
Density	$kg.m^{-3}$	9.4
Viscosity @ 40°C	$kg.m^{-1}.s^{-1}$	7×10^{-6}
Specific heat capacity (C_p)	$J.kg^{-1}.K^{-1}$	2430

Table D.2: Gaseous diesel fuel properties [6]

It should be noted that the standard values for the liquid fuel density, droplet surface tension and vapour pressure were taken as the average values of data extracted from the FLUENT® Materials Database [6] and literature [7].

In South Africa, diesel does not entirely conform to the EN 590:2004 standard, as alterations have been made to suit local conditions and possibly refinery capabilities. The following relevant criteria exist for this locale in the year 2006 [58]:

Property	Units	Minimum value	Maximum value
Density @ 15°C	$kg.m^{-3}$	800	845
Viscosity @ 40°C	$mm^2.s^{-1}$	2.20	5.30

Table D.3: Relevant South African diesel fuel specifications

The specifications for fuel viscosity translates to limits of 0.001666 $kg.m^{-1}.s^{-1}$ and 0.003735 $kg.m^{-1}.s^{-1}$ for fuel of density 830 $kg.m^{-3}$. These values were taken as guideline limits for alterations that could be made to the fuel properties. The new Euro 5 specifications lie within the limits specified above.

D.1.1 Cavitation model

Certain fluid properties are needed to define the effect of cavitation on the fluid. The following settings were used for the cavitation model used by FLUENT®:

Property	Units	Value
Vapour pressure	Pa	1930
Surface tension	$N.m^{-1}$	0.025
Non-condensable gas	ppm	15

Table D.4: Cavitation model settings

The value used for the non-condensable gas was the standard value provided by FLUENT®, since no data detailing the concentration of contaminant gas in diesel was available. 15ppm is the saturation concentration of air in water at atmospheric pressure. Since the fuel would be sloshing and mixing with air in the fuel tank, it is felt that this value could be attained in a real-world scenario.

D.2 Boundary conditions

The following boundary conditions were applied at the specified locations:

Position	Property	Units	Value / Description
INLET	Type		Pressure inlet
	Gauge total pressure	bar	1500
	Initial gauge pressure	bar	1500
	Backflow turbulence intensity		0.0656
	Backflow turbulence length scale	m	0.0707
	Volume fraction		$7.5\text{x}10^{-4}$
	Bulk fluid temperature	K	360
OUTLET	Type		Pressure outlet
	Gauge Total Pressure	bar	50
	Backflow turbulence intensity		0.055
	Backflow turbulence length scale	m	1.06e-05
	Backflow volume fraction		1
	Backflow temperature	K	440
WALL	Type		Wall
	Wall temperature	K	360
AXIS	Type		Axis

Table D.5: Boundary conditions

The backflow volume fraction was set to unity (i.e. diesel vapour enters the domain under backflow conditions) since the density of the vapour and that of the gases in the combustion chamber would be of the same order of magnitude. Turbulence settings were specified normal to the boundary at which they are set.

D.3 Turbulence model

The standard $k - \epsilon$ turbulence model for fully turbulent flow was used to describe the effect of turbulence in the nozzle. The standard model constants, described in Table 4.1, were retained. The choice of turbulence model was based on the geometry, the fully turbulent conditions present in the nozzle and the literature. The cavitation model has been validated using the standard $k - \epsilon$ turbulence model [24]. Possible inaccuracy of results due to the choice of turbulence model, as suggested by literature [33], have been noted.

An enhanced-wall treatment was applied, since a low-velocity recirculating region appeared where the fluid separates from the nozzle wall just downstream of the nozzle throat. It is necessary in order to capture these low velocities in the boundary layer. Near zero velocities exist in this region for some time, while the flow near the axis retains its high-velocity. Also, the cavitation effect appears only in small regions adjacent to the nozzle wall, and a fine grid was required to capture the effects in the nozzle throat. Since the pressure-gradients between cells in the throat were very large, the option to enhance the capture of "pressure gradient effects" was also activated.

D.4 Initial conditions

Initial conditions were chosen such that the fluid was stationary and at low pressure. This would simulate the conditions that are present before the injector needle has begun to rise. Thus, the initial pressure of the computational domain was set at 50 bar, while the starting velocity of the fluid were set to zero.

D.5 Solver

In order to preserve accuracy, a double-precision solver was used. This preserves accuracy in the resolution of the pressure gradient in the flow regime. [4]

The PISO pressure-velocity coupling scheme was used for the solution of pressure and velocity fields. This is the most stable solver available for use on time-dependant problems, as it ensures a momentum balance after the pressure and velocity fields have been calculated. [4]

D.5.1 Discretisation

Second-order discretisation schemes were used to reduce the amount of numerical diffusion present in the system. It was considered important to use them because flow moves diagonally across some cells. The actual settings are described in Table D.6.

D.5.2 Stability

Stability was a major issue that was encountered when cavitating flow was present in the flow field. This is mainly due to the very high pressure gradients present in the flow field. Certain simulation settings were

Equation	Algorithm
Pressure	Second order
Momentum	Second order upwind
Vapour	QUICK
Turbulence kinetic energy	Second order upwind
Turbulence dissipation rate	Second order upwind
Energy	Second order upwind

Table D.6: Discretisation settings

altered in order to achieve good convergence and stability with the cavitation model. These settings that were used are described below.

AMG multigrid

The following settings in the algebraic multigrid were used, as recommended by the literature for cavitation problems [59, 60]:

1. For the pressure equation, use V-cycle was used.
   The termination criteria was set to 0.001.
   A maximum of 100 pressure calculation cycles were allowed.
2. The number of pre-sweeps was set to 1.
3. The number of post-sweeps was set to 3.

The alteration of these settings were performed to add accuracy to the pressure calculations, and stability to the calculations involved in the entire set of algebraic equations.

Neighbour correction

Where necessary, neighbour correction for the PISO algorithm was implemented. Up to 5 correction iterations were allowed when good stability was not achieved. This algorithm allows the pressure-correction step in the pressure-velocity coupling to be performed a number of times before the solver solves the other variables. In this way stability is enhanced, as the pressure gradients in a cavitating field are large.

D.5.3 Under-relaxation

Modification of the standard under-relaxation values was necessary to stabilise the calculation procedure. Lower under-relaxation values inhibited fast convergence for larger time-steps, but assisted in maintaining solution stability.

Table D.7 outlines the value ranges suggested for use with the cavitation model, and those used in the unsteady, axisymmetric simulations.

Property	Guideline value	Simulation
Pressure	0.2 - 0.7	0.4 - 0.7
Density	0.3 - 1.0	0.5 - 0.85
Momentum	0.05 - 0.4	0.25 - 0.35
Vapourisation mass	0.1 - 1.0	0.35 - 0.45
Vapour	N/A	0.45 - 0.55
Turbulence kinetic energy	N/A	0.4 - 0.6
Turbulence dissipation rate	N/A	0.25 - 0.45
Turbulent viscosity	N/A	1

Table D.7: Simulation under-relaxation values [4]

D.5.4 Time-dependency

Due to the nature of the flow, multiple time-scales were necessary to capture the flow events. Initially, time-steps in the order of 10 ns were required when flow was initialised and the flow-field is near stationary. This fairly rapidly reduced to 0.25 ns as the velocity through the nozzle increased. These minute time-steps were required in order to keep the cell Courant number low and thus maintain the stability and accuracy of the solution at each time-step. In certain instances, it was necessary to reduce the time-step further to 0.1 ns to attain convergence and good stability.

D.6 Approximations and simplifications

A brief overview of some approximations of the geometry and modelling technique used in this dissertation are discussed below.

D.6.1 Geometry

By using the enhanced wall treatment, it is not possible to model the effects of surface roughness, unless those surface imperfections are manually modelled in the geometry. For this reason, surface roughness is not taken into account. This may reduce bubbles nucleation due to surface roughness effect.

Axisymmetric nozzle is not entirely indicative of flow in a fuel injector, since the difference in flow from the sides of the nozzle is not accounted for. The nozzle offset angle with respect to the axis of the injector is ignored. This may inhibit, should it occur in real nozzles, the effect of vapour detaching from the wall of the nozzle. However, since a qualitative study of the effect of fuel parameters is to be determined, this simplification was considered to be justified.

The effect that the injector needle may have on nozzle flow has been neglected. This implies that any effect that the needle may have due to seating and unseating, as well as jetting has been ignored.

D.6.2 Materials

The concentration of the non-condensable gases is assumed to be uniform. This is an approximation associated with the cavitation model. The velocity difference between the two phases was considered so small as to be negligible.

For most simulations, the effect of temperature on the flow field is neglected. Flow is considered isothermal and both the liquid and gas are considered the be of constant density. This has been shown to lead to accurate and representative solutions for sharp-edged orifice geometries [24].

For simulations where temperature effects were to be considered, the liquid was still modelled as incompressible, but an incompressible ideal-gas model was used to describe the diesel gas. An ideal gas assumption is valid at high temperatures and low pressures, the latter of which describes the pressure of the vapour well. The vapour pressure was considered to be constant with respect to temperature.

E. Initial Decisions

The following chapter outlines initial decisions that were made in order to successfully simulate flow through an axisymmetric nozzle. The purpose of the chapter is to briefly describe the process undertaken to determine the optimum level of grid refinement and model requirements to use. The outcomes of these initial investigations were considered in the development of further models.

It should be noted that all of the settings described in Appendices B and D were used to perform the described simulations. For the most part, the accuracy of simulations was determined according to the visual description of the vapour phase and coefficient of discharge profiles and results. Velocity and pressure distributions were checked as a matter of course.

Due to the predicted significance of the turbulent effects on cavitation described in Section B.3, it was felt necessary that a grid that with sufficient resolution to capture these turbulent effects was imperative. Since it was known that stagnation and recirculation would occur in the orifice throat, it was considered necessary to produce a grid that used enhanced wall functions that could account for the stagnant flow near the wall.

E.1 Grid dependency

A check was done to determine the effect of grid size on the accuracy of the simulations. Several grids were checked, each differing fairly substantially in resolution. Steady-state single-phase models were run until the continuity residual was at $1\text{x}10^{-5}$ and all other residuals were at $1\text{x}10^{-3}$. The cavitation model was then implemented until the continuity residual reached $1\text{x}10^{-5}$.

Table E.1 describes the meshes used to determine the effect of grid dependency. The quality of the mesh was excellent as a regular grid was used.

Grid description	Low resolution	Medium resolution	High resolution
Number of cells	24116	43190	92640
Number of cells in nozzle	8768	15870	37940
Worst wall y^+ value inside nozzle	5	4.95	2.1
Worst wall y^+ value outside nozzle	8	7.1	2.73
Quality of result	Fair	Good	Good

Table E.1: Description of grid dependency mesh

By this comparison, it was decided that a grid similar to the medium resolution grid would be suitable for calculation purposes. Refinements were initially made to the existing medium to reduce the wall y^+ values below 5 as suggested for use with an Enhanced Wall function turbulence model. The benefits of using as coarse a mesh as possible include a reduction in time taken to run simulations, as well as a reduced Courant number for unsteady simulations.

Unsteady simulations were then run and wall y^+ were checked at different time intervals. It was observed that the y^+ values predicted were often lower than that predicted by steady simulations, especially in the initial stages of flow. The mesh was again modified both inside and outside the nozzle until the number of cells outside the nozzle was minimised and the y^+ value was near to and below 10. This leaves the y^+ value at the maximum value that can be used with Enhanced Wall functions, and allows a minimised computational and time expense. The wall y^+ value was highly transient, as the development of flow changed both the velocity and phase of the fluid adjacent to the wall.

The final grid to be used for unsteady simulations was created with the consideration of the time that each transient simulation would take to run. The grid had the following properties:

Number of cells	19120
Number of cells in nozzle	7680
Worst wall y^+ value inside nozzle	6.3
Worst wall y^+ value outside nozzle	8.2

Table E.2: Description of final axisymmetric grid

The high wall y^+ values were present at the nozzle entrance and in regions where high velocity liquid was adjacent to the wall. The value was lower in regions where the near-wall cells in the nozzle contained either vapour or had low velocity liquid. In excess of 80% of cells adjacent to the wall had y^+ values of less than 5 when transient simulations reached a steady-state.

It should be noted that the pressure inlet was set 5 nozzle radii upwind of the centre of the axis of the nozzle inlet. This was done because, through an iterative process, it was determined that the static pressure and velocity at this point are sufficiently close to 1500 bar and 0 m/s respectively. It was also determined that the proximity of the high pressure inlet to the nozzle is sufficiently large so that the pressure inlet does not affect the pressure distribution at the nozzle entrance.

E.2 Stability and convergence criteria

Convergence criterion in unsteady simulations changed as the flow in the nozzle developed. When single-phase flow was present, convergence of all properties was rapid and easily attained. For this reason, initial time-steps were large and high under-relaxation values were set. Residuals were set at or below 1×10^{-3} for all properties.

The appearance of vapour due to cavitation caused stability issues. As a result of this, time-steps had to be significantly reduced to each iteration and under-relaxation factors had to be decreased. It was found that, even with a fine grid, convergence of the continuity equation to a residual of less than 1×10^{-3} was difficult. All other residuals converged to values less than 1×10^{-4} when the time-step was decreased.

Transient simulations were only considered to fully converged when the residual magnitudes described in the above paragraphs were attained and the flow conditions had stabilised. The mass-flow through the nozzle outlet had to reach a steady value, and the velocity profile at the exit needed to stabilise before transient simulations were ended.

APPENDIX: Bubble Collapse

F. Bubble collapse: Fluid properties

F.1 Base conditions

Property	Units	Value
Density	$kg.m^{-3}$	830
Far-field pressure	bar	50
Temperature	K	360
Viscosity	$kg.m^{-1}.s^{-1}$	0.00332
Surface Tension	$N.m^{-1}$	0.025

Table F.1: Liquid properties

Property	Units	Value
Molar mass	$kg.mol^{-1}$	221

Table F.2: Vapour properties

Property	Units	Value
Mass fraction	ppm	15
Specific heat capacity (C_v)	$J.kg^{-1}.K^{-1}$	717.5
Molar mass	$kg.mol^{-1}$	29

Table F.3: Air properties

Property	Units	Value
Temperature	K	400
Pressure	Pa	1860.6
Radius	μm	5.50
Velocity	$m.s^{-1}$	0
Acceleration	$m.s^{-2}$	-6.25×10^{8}
Polytropic value		1

Table F.4: Initial bubble properties

F.2 Temperature dependant fluid properties

The specific latent heat of evaporation of diesel is given by [7]:

$$L = \frac{251.3 - (0.377 * (T - 273))}{\rho} \tag{F.1}$$

Table F.5 provides the values for the temperature dependant conductivity of air. Conductivity is not greatly dependant on pressure.

Temperature	Conductivity
K	W/m.K
100	0.009246
150	0.013735
200	0.01809
250	0.02227
300	0.02624
350	0.03003
400	0.03365
450	0.03707
500	0.04038
550	0.0436
600	0.04659
650	0.04953
700	0.0523
750	0.05509
800	0.05779
850	0.06028
900	0.06279
950	0.06525
1000	0.06752
1100	0.0732
1200	0.0782
1300	0.0837
1400	0.0891
1500	0.0946
1600	0.1
1700	0.105
1800	0.111
1900	0.117
2000	0.124
2100	0.131
2200	0.139
2300	0.149
2400	0.161
2500	0.175

Table F.5: Temperature dependant conductivity of air [8]